

REMEDICATION OF DNAPLs IN SATURATED POROUS MEDIA:  
COSOLVENT FLUSHING AND SHERWOOD CORRELATION

by

Derya Aydın Sarıkurt

B.S. in Environmental Engineering, İstanbul University, 2006

M.S. in Environmental Sciences, Boğaziçi University, 2010

Submitted to the Institute of Environmental Sciences in partial fulfillment of

the requirements for the degree of

Doctor of Philosophy

in

Environmental Sciences

Boğaziçi University

2018

To my “*Little Mr. Sunshine*”

## ACKNOWLEDGEMENTS

I would like to express my deepest gratitude to my supervisor Prof. Dr. Nadim Copty for giving me the opportunity to do this PhD. This study would not have been possible without his consistent guidance, encouragement, support and generous help. I also would like to express my gratitude to the members of my thesis committee, Prof. Dr. Cevza Melek Kazezyılmaz Alhan, Assoc. Prof. Dr. Nihat Hakan Akyol, Prof. Dr. Ferhan Çeçen, and Assoc. Prof. Dr. Başak Güven for taking time to evaluate my study.

I would like to thank Prof. Dr. George Karatzas and Dr. Zoi Dokou for their contributions and ideas on this work. I also would like to thank Assist. Prof. Dr. Ulas Tezel for his help when operating GC-MS.

I am grateful to Kübra Karaman, Korcan Yakşı, Filiz Ayılmaz and Çağrı Gökdemir for their technical help in the laboratory.

I would like to thank Ece Özön, Fatih Sert, Evrim Kalkan, Tunç Öztunç, Öncü Maracı, Emrah Çoraman and all of my other friends for their emotional support. I would also like to express my sincere gratitude to all the members of Boğaziçi University Institute of Environmental Sciences.

Finally, I would like to thank my family; my mother, my father, and my sister. The most special thanks go to Türev Sarıkurt for supporting me for all those years in good and bad times. His help was countless for this thesis. Last but not least, I am most grateful to my little son Güneş Sarıkurt who is included to this thesis process at the end and brings joy to my life.

This dissertation was supported by a Research Fund of Boğaziçi University grant (7682) and a TÜBİTAK grant (113Y281) to Nadim Copty.

## ABSTRACT

### **REMEDICATION OF DNAPLs IN SATURATED POROUS MEDIA: COSOLVENT FLUSHING AND SHERWOOD CORRELATION**

The contamination of the subsurface by the accidental release of organic contaminants in the form of non-aqueous phase liquids (NAPLs) is a widespread and challenging environmental problem. However, there is lack of cost effective technologies for the remediation of groundwater systems contaminated with NAPLs. A key process influencing the effectiveness of NAPL remediation is the interphase mass transfer which is the transfer of components across the interface separating the aqueous and NAPL phases. This study evaluates the use of cosolvent flushing for the removal of NAPLs from saturated porous media. Intermediate-scale laboratory experiments were conducted to investigate the impact of cosolvent content, flow velocity, and pumping pattern on cosolvent enhanced NAPL dissolution. Results demonstrated the importance of the flushing solution content and the flow characteristics on NAPL removal. The experimental results were also modeled using multiphase flow simulator. The model results highlighted the significance of the interphase mass transfer in NAPL remediation and the need to model this process as a non-equilibrium kinetic process. To further elucidate the factors influencing the interphase mass transfer mechanism, a series of controlled dissolution experiments from pooled NAPL were also conducted. The interpretation of the experiments was performed using a 2D pore network model in addition to a simplified 1D analytical solution. Results showed that the analytical solution which ignores lateral transport, under-estimates the interphase mass transfer coefficient. Based on the estimated mass transfer coefficients, improved non-lumped Sherwood correlations were developed. These correlations can be used in future modeling studies involved pooled NAPL configurations.

## ÖZET

### **DNAPL'LERİN DOYMUŞ GÖZENEKLİ ORTAMDAN GİDERİMİ: YARDIMCI SOLVENTLE YIKAMA VE SHERWOOD KORELASYONU**

Yeraltı sularının suyla karışmayan organik kirleticiler (NAPLs) ile kirlenmesi yaygın ve çözümü zor olan bir çevresel problemdir. Ancak, NAPL'ler ile kirlenmiş yeraltı suyu sistemlerinin iyileştirilmesinde maliyeti düşük teknolojiler bulunmamaktadır. NAPL arıtımının verimini etkileyen ana proseslerden biri fazlar arası kütle transferidir. Fazlar arası kütle transferi, bileşenlerin, su fazı ile organik fazı birbirinden ayıran arayüz boyunca iletimi olarak tanımlanabilir. Bu çalışma, NAPL'lerin doymuş gözenekli ortamdan giderimi için yardımcı solvent ile yıkama prosesinin kullanımını değerlendirmektedir. Yıkama çözeltisi içindeki yardımcı solvent miktarının, akış hızının ve pompalama düzeninin NAPL çözünürlüğüne etkisini incelemek için orta ölçekli laboratuvar deneyleri yapılmıştır. Sonuçlar yıkama çözeltisi içeriğinin ve akış özelliklerinin NAPL giderimindeki önemini göstermiştir. Deneysel sonuçlar ayrıca çok fazlı akış modeli kullanılarak modellenmiştir. Model sonuçları, fazlar arası kütle transferinin NAPL giderimi uygulamalarındaki önemini ve bu prosesin dengede olmayan kinetik bir proses olarak modellenmesi gerektiğini vurgulamıştır. Fazlar arası kütle transfer mekanizmasını etkileyen faktörleri daha ayrıntılı incelemek için birikinti halinde NAPL kullanılarak kontrollü çözünme deneyleri yapılmıştır. Deneylerin yorumlanması iki boyutlu gözenek ağı modeli ve basitleştirilmiş tek boyutlu analitik çözüm kullanılarak gerçekleştirilmiştir. Sonuçlar, yatay taşınımın ihmal edildiği analitik çözümün iki boyutlu gözenek ağı modeline kıyasla fazlar arası kütle transfer katsayısını daha düşük tahmin ettiğini göstermiştir. Elde edilen kütle transfer katsayılarına bağlı olarak yeni Sherwood korelasyonları geliştirilmiştir. Bu korelasyonlar, birikinti halindeki NAPL konfigürasyonlarını içeren gelecekteki modelleme çalışmalarında kullanılabilir.

## TABLE OF CONTENTS

ACKNOWLEDGEMENTS.....	iv
ABSTRACT.....	v
ÖZET.....	vi
TABLE OF CONTENTS.....	vii
LIST OF FIGURES.....	x
LIST OF TABLES.....	xvi
LIST OF SYMBOLS/ABBREVIATIONS.....	xvii
1. INTRODUCTION.....	1
2. BACKGROUND AND LITERATURE REVIEW.....	4
2.1. Non-aqueous Phase Liquids (NAPLs) as Subsurface Contaminants.....	4
2.2. Characteristic Properties of NAPL.....	6
2.2.1. Solubility.....	6
2.2.2. Interfacial Tension.....	7
2.2.3. Density.....	7
2.2.4. Viscosity.....	7
2.2.5. Wettability.....	8
2.3. Remediation Methods for NAPL Contamination.....	8
2.3.1. Soil Vapor Extraction.....	9
2.3.2. Air Sparging.....	9
2.3.3. In-situ Chemical Treatment.....	9
2.3.4. Reductive Dechlorination by Nanoparticles.....	10
2.3.5. In-situ Chemical Agent Flushing.....	10
2.4. Interphase Mass Transfer.....	13
3. PURPOSE.....	19
4. MATERIALS AND METHODS.....	21
4.1. Batch Experiments.....	21
4.1.1. Interfacial Tension Measurements.....	21
4.1.2. Solubility Measurements.....	22
4.1.3. Miscibility Measurements.....	22
4.1.4. TCE Analysis.....	23
4.2. Intermediate-Scale Flushing Experiments.....	24
4.2.1. Cosolvent Flushing Experiments.....	25

4.2.2. Tracer Tests.....	26
4.3. Modelling.....	27
4.3.1. Model Description.....	27
4.3.1.1. Capillary Pressure.....	28
4.3.1.2. Relative Permeability.....	28
4.3.1.3. NAPL Partitioning.....	29
4.3.1.4. Ternary Phase Diagram.....	29
4.3.2. Model Description.....	30
4.4. Flow Cell Experiments.....	32
4.4.1. Dissolution Experiments.....	32
4.4.2. Tracer Tests.....	34
4.5. Estimation of the mass transfer coefficient and development of Sherwood correlation.....	34
5. ENHANCED DNAPL SOLUBILIZATION IN SATURATED POROUS MEDIA AND NUMERICAL MODELLING.....	39
5.1. Calibration Curve of TCE.....	39
5.2. Batch Experiments.....	40
5.2.1. Interfacial Tension Measurements.....	40
5.2.2. Solubility Measurements.....	41
5.2.3. Miscibility Measurements.....	42
5.3. Intermediate-Scale Flushing Experiments.....	43
5.3.1. Tracer Tests.....	43
5.3.2. Cosolvent Flushing Experiments.....	45
5.4. Modelling.....	50
5.4.1. Calibration of the Model.....	50
5.4.2. Modelling Results.....	51
6. INTERPHASE MASS TRANSFER FROM POOLED DNAPL AND DETERMINATION OF THE SHERWOOD CORRELATION.....	57
6.1. Calibration Curve of DCB.....	57
6.2. Flow Cell Experiments.....	58
6.2.1. Tracer Tests.....	58
6.2.2. Dissolution Experiments.....	59
6.3. Estimation of the Mass Transfer Coefficient.....	62
6.4. Development of Sherwood Correlation.....	83
7. CONCLUSION AND RECOMMENDATIONS.....	86

REFERENCES..... 91

APPENDIX A: PORE NETWORK FORTRAN CODE FOR FLOW CELL  
FILLED WITH GLASS BEADS..... 104

APPENDIX B: PORE NETWORK FORTRAN CODE FOR FLOW CELL  
FILLED WITH SAND..... 109

## LIST OF FIGURES

Figure 2.1. The spread of LNAPLs (a) and DNAPLs (b) in subsurface.....	5
Figure 2.2. Variation of surface tension, solubility and interfacial tension with surfactant concentration (Lowe et al., 1999).....	11
Figure 2.3. Schematic of interphase mass transfer.....	14
Figure 4.1. Interfacial tension meter (KSV 703 Digital Tensiometer).....	22
Figure 4.2. TCE peak obtained from GC-MS analysis.....	23
Figure 4.3. Front view of the intermediate-scale flushing tank.....	24
Figure 4.4. Model discretization and TCE injection point and source zone.....	31
Figure 4.5. Sketch of the flow cell.....	32
Figure 4.6. Flow cell compacted with two different porous media, a) sand, b) glass beads.....	33
Figure 4.7. Pore network model used to simulate NAPL dissolution.....	36
Figure 5.1. TCE calibration curve for GC-MS.....	39
Figure 5.2. TCE calibration curve for UV-vis Spectrophotometer.....	40
Figure 5.3. Interfacial tension between TCE and the aqueous phase as a function of ethanol content (% by volume) in the aqueous phase.....	41
Figure 5.4. Solubility of TCE in ethanol-water system as a function of volume fraction of ethanol in the aqueous phase.....	42
Figure 5.5. Ternary phase diagrams for TCE-ethanol-water (mass %).....	43

Figure 5.6. Tracer test experimental data and best fit solutions.....	44
Figure 5.7. The photos of the dyed tracer test.....	45
Figure 5.8. Cumulative TCE mass in the effluent.....	46
Figure 5.9. Effect of different flow conditions on TCE mass recovery (mg and %)......	48
Figure 5.10. Modeling results for DNAPL injection zone size of 5x5 cm.....	52
Figure 5.11. Modeling results for DNAPL injection zone size of 3x3 cm.....	54
Figure 5.12. Recovered TCE mass calculated from experiments and with model.....	55
Figure 5.13. Modified Sherwood number versus Reynolds number for all experiments.....	56
Figure 6.1. DCB calibration curve for UV-vis Spectrophotometer.....	57
Figure 6.2. Tracer test experimental data and best fit solutions.....	59
Figure 6.3. Effluent aqueous phase concentrations as a function of velocity for the glass beads and sand experiments.....	61
Figure 6.4. Contour plot of the normalized aqueous DCB concentration computed with the pore network model for $Pe=8.7$ (glass beads).....	64
Figure 6.5. Contour plot of the normalized aqueous DCB concentration computed with the pore network model for $Pe=13.2$ (glass beads).....	64
Figure 6.6. Contour plot of the normalized aqueous DCB concentration computed with the pore network model for $Pe=36.1$ (glass beads).....	65
Figure 6.7. Contour plot of the normalized aqueous DCB concentration computed with the pore network model for $Pe=79.1$ (glass beads).....	65

Figure 6.8. Contour plot of the normalized aqueous DCB concentration computed with the pore network model for $Pe=163.4$ (glass beads).....	66
Figure 6.9. Contour plot of the normalized aqueous DCB concentration computed with the pore network model for $Pe=334.2$ (glass beads).....	66
Figure 6.10. Contour plot of the normalized aqueous DCB concentration computed with the pore network model for $Pe=515.9$ (glass beads).....	67
Figure 6.11. Contour plot of the normalized aqueous DCB concentration computed with the pore network model for $Pe=980.4$ (glass beads).....	67
Figure 6.12. Contour plot of the normalized aqueous DCB concentration computed with the 1D analytical solution for $Pe=8.7$ (glass beads),.....	68
Figure 6.13. Contour plot of the normalized aqueous DCB concentration computed with the 1D analytical solution for $Pe=13.2$ (glass beads).....	68
Figure 6.14. Contour plot of the normalized aqueous DCB concentration computed with the 1D analytical solution for $Pe=36.1$ (glass beads).....	69
Figure 6.15. Contour plot of the normalized aqueous DCB concentration computed with 1D analytical solution for $Pe=79.1$ (glass beads).....	69
Figure 6.16. Contour plot of the normalized aqueous DCB concentration computed with the 1D analytical solution for $Pe=163.4$ (glass beads).....	70
Figure 6.17. Contour plot of the normalized aqueous DCB concentration computed with the 1D analytical solution $Pe=334.2$ (glass beads).....	70
Figure 6.18. Contour plot of the normalized aqueous DCB concentration computed with the 1D analytical solution for $Pe=515.9$ (glass beads).....	71
Figure 6.19. Contour plot of the normalized aqueous DCB concentration computed with the 1D analytical solution $Pe=980.4$ (glass beads).....	71

Figure 6.20. Contour plot of the normalized aqueous DCB concentration computed with the pore network model for $Pe=1.3$ (sand).....	72
Figure 6.21. Contour plot of the normalized aqueous DCB concentration computed with the pore network model for $Pe=1.6$ (sand).....	72
Figure 6.22. Contour plot of the normalized aqueous DCB concentration computed with the pore network model for $Pe=2.3$ (sand).....	73
Figure 6.23. Contour plot of the normalized aqueous DCB concentration computed with the pore network model for $Pe=8.1$ (sand).....	73
Figure 6.24. Contour plot of the normalized aqueous DCB concentration computed with the pore network model for $Pe=15.4$ (sand).....	74
Figure 6.25. Contour plot of the normalized aqueous DCB concentration computed with the pore network model for $Pe=30.2$ (sand).....	74
Figure 6.26. Contour plot of the normalized aqueous DCB concentration computed with the pore network model for $Pe=59.8$ (sand).....	75
Figure 6.27. Contour plot of the normalized aqueous DCB concentration computed with the pore network model for $Pe=99.5$ (sand).....	75
Figure 6.28. Contour plot of the normalized aqueous DCB concentration computed with the pore network model for $Pe=185.2$ (sand).....	76
Figure 6.29. Contour plot of the normalized aqueous DCB concentration computed with the pore network model for $Pe=216.0$ (sand).....	76
Figure 6.30. Contour plot of the normalized aqueous DCB concentration computed with the 1D analytical solution for $Pe=1.3$ (sand).....	77
Figure 6.31. Contour plot of the normalized aqueous DCB concentration computed with the 1D analytical solution for $Pe=1.6$ (sand).....	77

- Figure 6.32. Contour plot of the normalized aqueous DCB concentration computed with the 1D analytical solution for  $Pe=2.3$  (sand)..... 78
- Figure 6.33. Contour plot of the normalized aqueous DCB concentration computed with the 1D analytical solution for  $Pe=8.1$  (sand)..... 78
- Figure 6.34. Contour plot of the normalized aqueous DCB concentration computed with the 1D analytical solution for  $Pe=15.4$  (sand)..... 79
- Figure 6.35. Contour plot of the normalized aqueous DCB concentration computed with the 1D analytical solution for  $Pe=30.2$  (sand).....79
- Figure 6.36. Contour plot of the normalized aqueous DCB concentration computed with the 1D analytical solution for  $Pe=59.8$  (sand).....80
- Figure 6.37. Contour plot of the normalized aqueous DCB concentration computed with the 1D analytical solution for  $Pe=99.5$  (sand).....80
- Figure 6.38. Contour plot of the normalized aqueous DCB concentration computed with the 1D analytical solution for  $Pe=185.2$  (sand).....81
- Figure 6.39. Contour plot of the normalized aqueous DCB concentration computed with the 1D analytical solution for  $Pe=216.0$  (sand)..... 81
- Figure 6.40. Comparison of the mass transfer coefficients determined with the analytical solution and the 2D pore network model for, a) glass beads, and b) sand..... 82
- Figure 6.41.  $Sh$  calculations for glass beads ( $d_m= 0.001$  m) and sand ( $d_m= 0.0002$  m) and their best-fit correlations. For comparison the data from Zilliox et al. (1973) [glass beads with  $d_m= 0.002$  m], Hoffmann (1969) [glass beads with  $d_m= 0.0005$  m], and the Pfannkuch (1984)  $Sh$  correlation are also shown. A logarithmic scale is used for the vertical axis..... 84
- Figure 6.42.  $Sh$  calculations for glass beads ( $d_m= 0.001$  m) and sand ( $d_m= 0.0002$  m) and  $Sh$  calculations for glass beads ( $d_m= 0.001$  m) and sand ( $d_m= 0.0002$  m)

and their best-fit correlations. For comparison the data from Zilliox et al. (1973) [glass beads with  $d_m = 0.002$  m], Hoffmann (1969) [glass beads with  $d_m = 0.0005$  m], and the Pfannkuch (1984) Sh correlation are also shown.

A non-logarithmic scale is used for the vertical axis..... 85

## LIST OF TABLES

Table 2.1. Lumped Sherwood correlations from literature.....	17
Table 4.1. List of tank flushing experiments.....	25
Table 4.2. Input parameters of pore network model for the two different porous media.....	38
Table 5.1. List of key parameters used in the model simulations.....	51
Table 5.2. Comparative measures (RMSE and NRMSE) and mass transfer coefficients for different DNAPL injection zone sizes of 5x5 cm and 3x3 cm.....	51
Table 6.1. Dispersion coefficient and dispersivity values determined from tracer tests.....	59
Table 6.2. Velocity and effluent concentration data from sand dissolution experiments.....	60
Table 6.3. Velocity and effluent concentration data from sand dissolution experiments.....	60
Table 6.4. Mass transfer coefficients determined with the 1D analytical equation and 2D pore network model for glass beads.....	62
Table 6.5. Mass transfer coefficients determined with the 1D analytical equation and 2D pore network model for sand.....	63

## LIST OF SYMBOLS/ABBREVIATIONS

Symbol	Explanation	Unit
$A$	Cross sectional area of the tank	$L^2$
$a$	Interfacial area per unit volume of porous media	$L^2/L^3$
$A_e$	Empirical parameter that depends on $C_{3max}$	-
$B$	Empirical parameter that depends on the binodal curve	-
$C$	Aqueous phase concentration	$M/L^3$
$C_{eff}$	Steady-state effluent concentration	$M/L^3$
$C_i$	Aqueous-phase concentration in chamber $I$	$M/L^3$
$C_m$	Concentration associated with $Q_m$	$M/L^3$
$C_s$	Effective NAPL solubility	$M/L^3$
$C_0$	Influent concentration	$M/L^3$
$C_l$	Concentration of each component in each phase	$M/L^3$
$C_{3max}$	Maximum height of the binodal curve of the TPD	-
$C_n^w$	Water concentration in the NAPL phase	v/v
$C_w^n$	NAPL concentration in the aqueous phase	v/v
$C_p^c$	Cosolvent concentration in the cosolvent poor phase	v/v
$\Delta C_{im}$	Difference in concentration between chamber $i$ and adjacent chambers $m$	$M/L^3$
$D$	Dispersion coefficient	$L^2/T$
$D_m$	Molecular diffusion coefficient	$L^2/T$
$D_m$	Mean grain diameter of the porous medium	L
$g$	Gravity	$L/T^2$
$i$	Chamber index	-
$J$	Interphase mass transfer rate	$L/T^2$
$k$	Intrinsic permeability of the porous	$L^2$

	medium	
$k_f$	Explicit interphase mass transfer coefficient	L/T
$K_L$	Lumped interphase mass transfer coefficient	1/T
$k_{Li&Fu}$	Exponent of the IFT expression	-
$k_{rw}$	Relative permeability to the aqueous phase	-
$L$	Length of the flow cell (=0.1 m)	L
$l_1$	Aqueous phase	-
$l_2$	NAPL phase	-
$l_3$	Microemulsion	-
$M$	Number of adjacent chambers	-
$n$	Porosity of the porous media	-
$N_{Ca}$	Capillary number	-
$N_T$	Tapping number for horizontal flow	-
$P_{bl}$	Bubbling pressure for phase 1	M/L-T <sup>2</sup>
$P_{cll'}$	Capillary pressure between phase 1 and 1'	M/L-T <sup>2</sup>
$Q$	Flow rate	L <sup>3</sup> /T
$q$	Darcy velocity	L/T
$Q_m$	Flow rate into/out of chamber $i$ to adjacent chambers	L <sup>3</sup> /T
$q_w$	Darcy velocity of the aqueous phase	L/T
$Re$	Reynolds number	-
$S_c$	Schmidt number	-
$S_h$	Explicit Sherwood number	-
$S_h'$	Lumped Sherwood number	-
$S_n$	Initial NAPL saturation	-
$S_{nl'}$	Standardized saturation	-
$t$	Time	T
$v$	Velocity	L/T
$V_s$	Volume of chamber $i$	L <sup>3</sup>
$x$	Length in the direction of flow	L
$x_d$	Travel distance into the region of residual organic phase	L

$\alpha$	Dispersivity	L
$\theta$	Bond number	-
$\theta_n$	Saturation of the organic phase	-
$\lambda$	Pore size distribution coefficient	-
$\mu$	Aqueous phase kinematic viscosity	$L^2/T$
$\mu_w$	Aqueous phase dynamic viscosity	$M/L-T$
$\rho_w$	Aqueous phase density	$M/L^3$
$\Delta\rho$	Density difference between water and organic liquid phase	$M/L^3$
$\sigma$	Interfacial tension when a cosolvent is present	$M/T^2$
$\sigma_{ow}$	Interfacial tension between the organic liquid and water	$M/T^2$
$\sigma_0$	Interfacial tension in the absence of a cosolvent	$M/T^2$

### Abbreviation

### Explanation

BTEX	Benzene-toluene-ethylbenzene-xylene
CMC	Critical micelle concentration
DCB	1,2-dichlorobenzene
DNAPL	Dense non-aqueous phase liquid
GC-MS	Gas chromatography-mass spectroscopy
HPCD	Hydroxypropyl- $\beta$ -cyclodextrin
IFT	Interfacial tension
LNAPL	Light non-aqueous phase liquid
NAPL	Non-aqueous phase liquid
nZVI	Zero valent iron nanoparticles
PCE	Perchloroethylene
PRB	Permeable reactive barriers
TCA	1,1,1-trichloroethane
TCE	Trichloroethylene
TPD	Ternary phase diagram
ZVI	Zero valent iron

## 1. INTRODUCTION

The contamination of the subsurface by the accidental release of organic contaminants is a widespread and challenging environmental problem that poses a serious threat to groundwater reserves worldwide. During the last two decades, more than 311,000 contaminated sites have been cleaned up in the USA alone, and many more remain to be remediated (U.S.EPA, 2004). The most serious contaminants of groundwater resources are petroleum hydrocarbons (e.g., oil, gasoline, diesel) and chlorinated solvents (e.g., perchloroethylene (PCE), trichloroethylene (TCE), and 1,1,1-trichloroethane (TCA)). These contaminants have a high toxicity and they are associated with a high exposure risk due to their widespread use in industrial applications (Stroo et al. 2003). For instance, TCE can persist for decades in the subsurface after its release (Guilbeaut et al., 2005) and pose risk for human health if the groundwater contaminated by TCE used as drinking water (McKnight et al., 2010). Since many of these organic contaminants have non-polar structures, low aqueous solubilities, and high interfacial tension they often persist in the environment as a separate phase termed non-aqueous phase liquids (NAPLs).

NAPLs are typically classified as either light non-aqueous phase liquids (LNAPLs) which have lower density than water, or dense non-aqueous liquids (DNAPLs) which have higher density than water. LNAPLs migrate downwards through the vadose zone accumulating mostly at or above the water table within the capillary fringe. On the other hand, DNAPLs tend to migrate vertically under the influence of gravity to greater depths below the water table because of the density effect.

When a NAPL mass enters the subsurface, it migrates through the subsurface and gets entrapped within individual pores in the form of discontinuous blobs, or may accumulate in the form of pools if some barrier is encountered. As water infiltrate through the soil and groundwater flow get in contact with NAPL, the entrapped and pooled NAPLs start to slowly dissolve into the aqueous phase forming a mobile contaminant plume. Due to the low solubility, relatively high toxicity and relatively low degradation of many hydrocarbons, the presence of NAPLs in the subsurface can cause the contamination of groundwater resources for decades and perhaps centuries (Pankow and Cherry, 1996).

In order to completely remove or reduce the source zone NAPL contamination in subsurface, various remediation technologies have been proposed. The removal of many NAPLs by conventional remediation methods such as pump & treat has been found to be ineffective under

natural conditions encountered in the field because the entrapment of NAPLs in the porous media and their relatively low dissolution and degradation rates (Grubb and Sitar, 1994; Saba et al. 2001; Childs et al., 2006). The need for alternative methods for NAPL remediation has led to the development of new technologies starting from the late 1980's. These innovative strategies for source zone NAPL treatment include in-situ chemical agent flushing, in-situ chemical treatment, air sparging, reductive dechlorination with reactive nanoparticles and soil vapor extraction (Tick et al., 2003; Soga et al. 2004; Childs et al., 2006; Oostrom et al. 2006; Brusseau et al., 2011).

In-situ cosolvent flushing, the investigated technique in this dissertation, is among the more promising technologies for NAPL source zone remediation (Oostrom et al., 2006). This remediation process involves the injection of cosolvents into the contaminant source zone to enhance the solubility of the NAPL and possibly instigate its mobility as a separate phase by reducing the interfacial tension. Solubilized contaminants are carried downgradient and collected through recovery wells. In recent years, many researchers have evaluated the in-situ flushing technology for improved removal of NAPLs trapped in the subsurface (Hirasaki et al., 2000; Sabatini et al., 2000; Giese and Powers, 2002; Hofstee et al., 2003; Imhoff et al., 1994; Abriola et al., 2005; Childs et al., 2006; Agaoglu et al., 2012). Depending on the flushing agent used, the removal behavior of the contaminant may vary significantly. Therefore, it is very important to select the proper flushing agent before remediation process. The widely considered cosolvents are low molecular weight alcohols such as ethanol, 1- propanol, 2-propanol which are highly soluble and water miscible resulting in enhanced solubilization and mobilization of chlorinated solvents entrapped in the subsurface (Oostrom et al. 2006; Stroo and Ward 2010).

A key process that controls the fate of NAPLs in the subsurface and the effectiveness of any in-situ remediation technique is the interphase mass transfer which is the transfer of components across the interface separating the NAPL phase and the aqueous phase. In recent years, significant research has been conducted to elucidate the factors that influence interphase mass transfer rate in porous media (e.g., see recent review by Agaoglu et al., 2015). The NAPL dissolution, groundwater flow field and the spatial distribution of the multiphase system are major factors that affect the interphase mass transfer process. The interphase mass transfer rate can decrease in residual NAPL zones due to variation in flow velocity (Imhoff and Miller 1996). For pool NAPL configurations, clean water bypassing of the NAPL contaminated zone leads to dilution and consequently reduced effluent concentrations (Brusseau et al. 2002).

Much of the research efforts on interphase mass transfer consisted of laboratory experiments that provide definition of interphase mass transfer by empirical expressions. However, these expressions were mostly specific to the conditions of the idealized experiments and an inclusive interphase mass transfer definition is lacking. One of the major limitations has been the inability to define the distribution of the interfacial areas of the multiphase system.

The vast majority of published interphase mass transfer correlations considered the mass transfer (dissolution) from the NAPL phase into the pure water phase in the absence of any cosolvent. The focus of this dissertation will be on the evaluation of cosolvent flushing for the remediation of NAPL zones in saturated porous media. It will include both laboratory-scale experiments and numerical modeling. Because of the significance of the interphase mass transfer that controls the fate of NAPLs in the subsurface, additional controlled dissolution experiments were conducted and used to develop improved Sherwood correlations.

The rest of this dissertation is organized as follows:

- Chapter 2 includes some theoretical background information relating to NAPLs in porous media and literature review addressing groundwater contamination, enhanced NAPL solubilization, in-situ NAPL remediation, cosolvent flushing, multiphase modelling, and interphase mass transfer.
- Chapter 3 presents the purpose of this study.
- Chapter 4 describes the applied experimental procedures and numerical codes developed.
- Chapter 5 includes the results and discussion of the batch tests, intermediate-scale flushing experiments, and multiphase model used to simulate the cosolvent flushing experiments.
- Chapter 6 presents the results and discussion of NAPL dissolution experiments in flow cell, the numerical model developed to simulate dissolution experiments, leading to improved Sherwood correlations.
- Conclusion and recommendations for future work are discussed in Chapter 7.

## 2. BACKGROUND AND LITERATURE REVIEW

### 2.1. Non-aqueous Phase Liquids (NAPLs) as Subsurface Contaminants

In many parts of the industrialized world, groundwater resources are threatened by the organic contaminants in the subsurface. Hydrocarbons such as petroleum products and chlorinated compounds like PCE and TCE in the form of non-aqueous phase liquids (NAPLs) are among the most serious groundwater contaminants. These organic contaminants are mostly released into the subsurface from leaky underground storage tanks and surface spills. Once released into the subsurface, these compounds may exist as a separate liquid phase due to their low solubility, may sorb to the soil or form dissolved plumes as a result of slow dissolution process into the flowing groundwater.

As noted earlier, NAPLs are commonly classified as light non-aqueous phase liquids (LNAPLs) and dense non-aqueous phase liquids (DNAPLs). Their density relative to that of water has major influence on their fate and transport. LNAPLs, such as petroleum hydrocarbons, have lower densities than water. Hence, once LNAPLs are released into the subsurface, they migrate through the unsaturated soil to the water table. At the water table, LNAPLs tend to spread laterally causing a depression on the water table due to their weight (Illangasekare et al., 1995; Hu et al., 2010). The migration pathway of LNAPLs when released to the subsurface is presented in Figure 2.1a.

Compared to LNAPLs, DNAPLs, which include many chlorinated compounds, compose a more serious threat to the subsurface environment (Huling and Weaver, 1991). The most common DNAPLs are PCE, TCE, 1,2-dichlorobenzene (DCB), carbon tetrachloride, chloroform, dichloromethane, and polychlorinated biphenyls. These contaminants are used in many industrial applications such as chemical manufacturing, degreasing operations, commercial dry cleaning operations (Cohen and Mercer, 1993). When DNAPLs are released to the subsurface in sufficiently large volumes, migration will occur under gravitational forces down to and below the water table of an unconfined aquifer. When they reach some low permeability layer, they start spreading horizontally and continue travelling, in some cases, substantial horizontal distances away from the original source zone. Once DNAPLs migrating below the water table come to rest, they are generally found to exist in the form of residual NAPL and/or NAPL pools (Luciano et al., 2010). Figure 2.1b shows the schematic of a DNAPL release and migration.

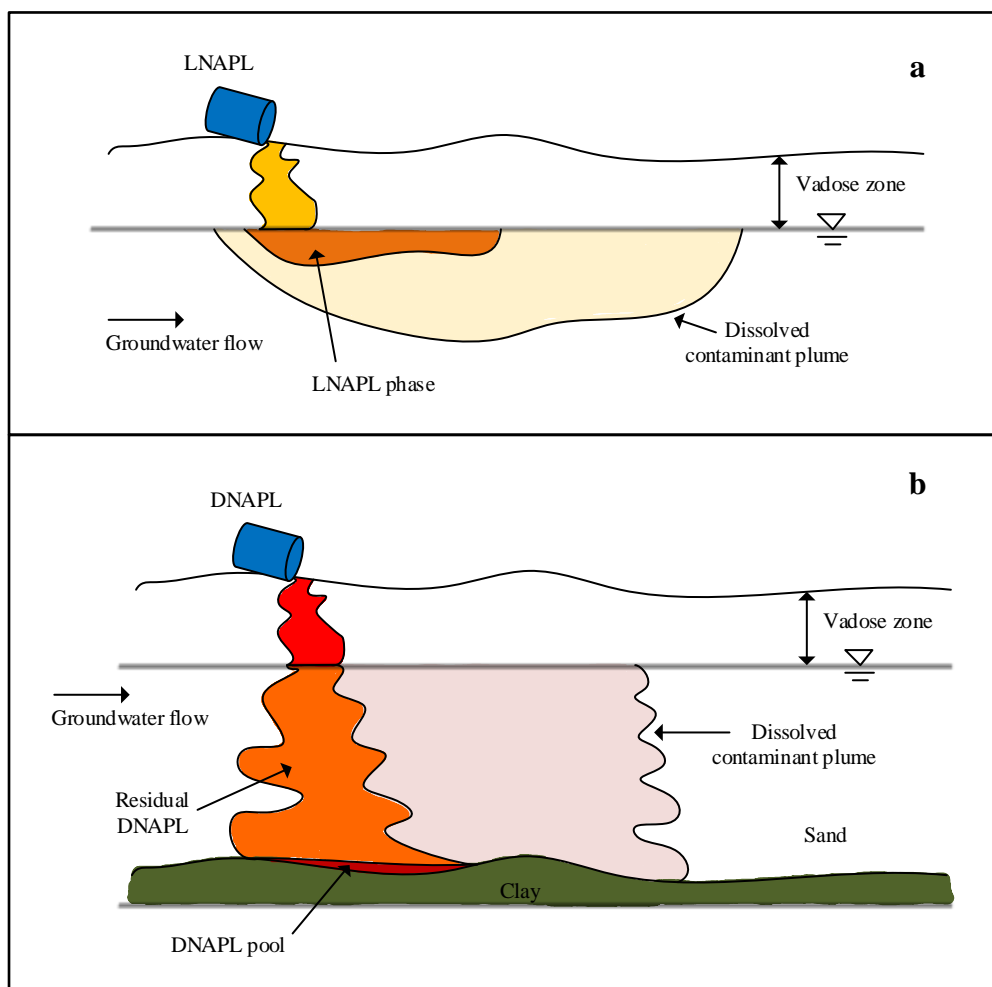


Figure 2.1. The spread of LNAPLs (a) and DNAPLs (b) in subsurface.

Many NAPLs exhibit relatively low aqueous solubility (typically in the ppm range). Therefore, NAPL constituents slowly partition into the aqueous phase thus causing a dissolved plume that pose a potential threat since it is mobile (Eberhardt and Grathwohl, 2002). Some NAPLs such as chlorinated solvents are highly volatile and they can partition into the soil gas causing further migration to the vadose zone. Depending on the characteristic properties, environmental conditions, geology and the content of the NAPL present in the subsurface, NAPLs (especially DNAPLs) may persist in the subsurface for many decades (Pankow and Cherry, 1996). Because of their long-term persistence as well as the large uncertainty in the distribution of NAPLs in the subsurface, remediation of the groundwater contaminated with NAPLs (especially DNAPLs) is an extremely challenging problem. In order to identify the difficulties in remediation of these contaminants, it is important to understand the characteristic properties of NAPLs.

## 2.2. Characteristic Properties of NAPL

The fate and transport of NAPLs in the subsurface are controlled by NAPL characteristics, subsurface media characteristics, and saturation dependent parameters. While porous media characteristics do not change easily, NAPL characteristics can potentially be changed favorably through different remedial techniques (Lunn and Kueper, 1999; Aydin et al., 2011; Yan et al., 2011; Aydin-Sarikurt et al., 2016). The main NAPL properties influencing their fate and transport in porous media are their solubility, interfacial tension with water, density, viscosity, and wettability. The governing subsurface media characteristics are their relative permeability and capillary pressure. Each of these properties is described below.

### 2.2.1. Solubility

The equilibrium concentration of a chemical in aqueous phase is defined as its solubility. It is a function of both temperature and pressure. NAPLs (with solubility typically on the order of hundreds of mg/L) distribute as residual and pool or dissolved plumes depending on their solubility. The ability of NAPLs to penetrate further into the subsurface is in large part due to their low solubility. Since NAPLs have low solubility that permit pools to persist for decades to centuries (Johnson and Pankow, 1992).

The dissolution rate of NAPLs depends on the solubility of the NAPL, the flow conditions of groundwater, and the contact area between flowing groundwater and the NAPL (Park and Parker, 2005). As the contact of NAPL and water increases, the aqueous concentration of NAPL increases. The low solubility of many compounds means that conventional treatment technologies such as pump & treat can only recover the NAPL mass at very low rates (Grubb and Sitar, 1994; Lowe et al., 1999). Through the use of chemical agents such as surfactants and/ or cosolvents, it is possible to enhance the solubility of NAPLs and hence shorten their recovery time. Despite the promise of such technologies, field applications have shown that they are unable to recover the entire NAPL mass (Christ et al., 2005; Childs et al., 2006). This is in large part due to the heterogeneity of the subsurface at the pore and local scales which causes the flushing solution to bypass some of the areas where the NAPL is entrapped.

### 2.2.2. Interfacial Tension

Interfacial tension (IFT) is defined as the tensile force that exists in the interphase of a two immiscible fluids. Once the IFT between these two immiscible liquids is depressed to near zero, they form a single phase and become miscible. For DNAPLs, such as chlorinated solvents, the interfacial tension which exists between water and DNAPL is on the order of 0.030 to 0.050 N/m (Cohen and Mercer, 1993). The interfacial tension of commonly encountered LNAPLs such as benzene and toluene is about 0.035 N/m (Cohen and Mercer, 1993).

When considering the mobility of the DNAPL, IFT is generally the control parameter. IFT decreases with increasing temperature and may be affected by pH, solvents and the gases in the solution (Mercer and Cohen, 1990). In order to increase the mobility of DNAPLs in the subsurface, IFT should be reduced significantly to near zero values.

### 2.2.3. Density

Density is a parameter used to distinguish DNAPLs from LNAPLs in a multicomponent NAPL. Most DNAPLs found in contaminated sites have densities ranging from 1,030 kg/m<sup>3</sup> to 1,700 kg/m<sup>3</sup> while LNAPL densities can be as low as about 750 kg/m<sup>3</sup> (Lowe et al., 1999). Generally, density is a function of temperature and pressure.

The density of a DNAPL is an important parameter when considering the application of an appropriate remediation design. In the case of cosolvent/surfactant flushing applications density manipulation is an important factor that changes the migration behavior and can cause unwanted downward migration of DNAPLs in the subsurface (Lunn and Kueper, 1997; Van Valkenburg and Anable, 2002). Therefore, it is critical to consider the density of DNAPLs to minimize the vertical DNAPL mobilization when selecting the remediation method.

### 2.2.4. Viscosity

Viscosity, which has a strong influence on the mobility of NAPLs, is defined as the resistance of a liquid to fluid flow. The relatively low viscosities of the chlorinated solvents provide relatively rapid downward movement in the subsurface. Viscosity is highly dependent on temperature. An increase in the temperature of a liquid generally will cause a decrease in its viscosity due to the reduction of interaction between molecules (Davis, 1997). The liquids with lower viscosities can

penetrate more easily in porous media. By increasing density/viscosity ratios, mobility of chlorinated solvents in the subsurface also increases (Cohen and Mercer, 1993).

### **2.2.5. Wettability**

Wettability is referred as the relative affinity of the soil to the different fluid phases. A liquid-liquid interface contacts with the solid surface with a specific angle which is called the contact angle or wettability angel. Generally, if the contact angle is less than  $90^\circ$ , the fluid can be accepted as wetting (such as water). If the contact angle is greater than  $90^\circ$ , the fluid is said to be the non-wetting fluid (such as NAPL) (Lowe et al., 1999). The wetting angle is an indicator that shows whether a porous media will be preferentially wetted by aqueous phase or the NAPL phase. In most natural systems, water is the wetting fluid and the immiscible phase is the non-wetting fluid. The wetting fluid tends to cover the surface of the media and occupy the smaller pores whereas non-wetting fluid is restricted in large openings. In the saturated zone, water is wetting fluid with respect to most NAPLs (Lowe et al., 1999).

## **2.3. Remediation Methods for NAPL Contamination**

In order to totally remove or at least reduce the source zone contamination of NAPLs, various contaminant remediation strategies have been developed and applied in varying degrees of success. Early efforts to remediate the groundwater involved pump & treat technology. Experiences with this technology show that dissolved phase removed with pumping is extremely small while the non-aqueous phase cannot be removed in most of the cases.

Conventional pump & treat technology involves extracting the contaminated groundwater through a recovery system for further ex-situ treatment at the surface. However, numerous field applications have demonstrated that pump & treat technology is ineffective for the restoration of groundwater contaminated by NAPLs due to the slow dissolution rates of residual and pooled DNAPLs into water (Mackay and Cherry, 1989; Grubb and Sitar, 1994; Okuda et al., 1996; Kavanaugh et al., 2003). Although pump & treat may be effective in controlling the downstream migration of dissolved contaminants, it is particularly ineffective and requires long operational periods for removing large amounts of NAPL mass due to the low aqueous solubility of NAPLs and large NAPL/water interfacial tension forces that tend to resist NAPL movement towards the extraction well. Therefore, innovative technologies have been developed in recent years to enhance the removal of NAPLs from subsurface. The commonly used techniques include soil vapor

extraction, air sparging, in-situ chemical treatment, reductive dechlorination by nanoparticles, and in-situ chemical agent flushing.

### **2.3.1. Soil Vapor Extraction**

Soil vapor extraction technology is based on vacuum application of the clean gas through wells near to the source of contamination in the subsurface and extraction of the volatile NAPL in the vadose zone and above the water table (Hyman and Dupont, 2001). This method is also effective for the removal of sorbed contaminants (Anwar et al., 2003). Subsurface temperature, soil permeability, soil moisture, and contaminant properties (solubility, vapor pressure and density) are the factors affecting the removal rates. The target contaminant groups for in-situ soil vapor extraction are volatile organic contaminants and some fuels.

### **2.3.2. Air Sparging**

The air sparging technology involves the injection of clean air into the saturated zone, enabling a phase transfer of hydrocarbons from the NAPL dissolved phases to a vapor phase. The volatilized contaminants then vented through the extraction wells in the unsaturated zones. Air sparging promotes biodegradation by increasing oxygen concentrations in the subsurface. Air sparging is applicable to volatile contaminants such as BTEX components, chlorinated solvents and various fuels (U.S.EPA, 1995). Waduge et al. (2004) conducted intermediate-scale tank experiments to investigate the effect of air sparging coupled with soil vapor extraction on the NAPL mass removal. The results of this study suggested that soil heterogeneity is major parameter that limits the complete remediation of NAPL due to complex entrapment.

### **2.3.3. In-situ Chemical Treatment**

In-situ chemical treatment technologies include destruction/degradation of the organic contaminants either with oxidation or with reduction. In-situ chemical oxidation involves the injection of the oxidants to convert organic contaminants in the groundwater to non-hazardous or less toxic compounds by degradative chemical reactions. The oxidizing agents most commonly used for treatment of contaminants are ozone, hydrogen peroxide/Fenton, potassium and sodium permanganate, and sodium persulfate (Siegrist et al., 2011). In recent years, applications of in-situ chemical treatment using oxidizing agents were highlighted in several published papers (Yin and Allen 1999; Siegrist et al., 2001; Krebs 2008, Brusseau et al., 2011; Akyol and Yolcubal, 2013).

#### **2.3.4. Reductive Dechlorination by Nanoparticles**

Nanotechnology is an emerging technology that could be applied in the environmental remediation efforts to reduce the costs and improve the cleanup performance. When implementing in-situ nanoremediation, no groundwater is pumped out or no soil is extracted for above ground treatment. In recent years many researchers have focused on zero valent iron (ZVI) which was found to be effective in remediation of various pollutants such as chlorinated methane, ethane and ethenes (Gillham and O'Hannesin, 1994); metals (Lien and Wilkin, 2005); and polychlorinated biphenyls (PCBs) (Yak et al., 2000).

Zero valent iron nanoparticles (nZVI) are more reactive than microscale ZVI and iron powders used in permeable reactive barriers (PRBs) because of their smaller particle sizes (10 to 100 nm) that give them a larger specific surface area (surface area per unit mass). Moreover, nZVI are smaller than most of the porous media pores (typically of the order of 0.01 to 1 mm), and therefore in principle nZVI can be transported to the contaminated source zone in subsurface. Consequently, nZVI have two advantages over the construction-grade ZVI used in conventional PRBs: (i) nZVI can be applied to the deep contaminated source zones by injections and (ii) nZVI are more effective in reducing contaminants because of their higher reactivity due to increased specific surface area. In particular, nZVI are being increasingly studied and tested for the in-situ remediation of groundwater sites contaminated with DNAPLs (Wang and Zhang, 1997; Liu et al., 2005; Saleh et al., 2007; Berge and Ramsburg, 2010; Phenrat et al., 2011; Fagerlund et al., 2012; Wang et al., 2012; Phenrat et al., 2015; Kumar et al., 2017). The results of these studies suggest that the successful nZVI remediation of DNAPL source areas may require significant enhancement in DNAPL dissolution. A major limiting factor found in many studies is the ability to deliver the nanoparticles to the source zone (Saleh et al., 2007).

#### **2.3.5. In-situ Chemical Agent Flushing**

In-situ chemical agent flushing is one of the most promising technologies for NAPL zone remediation. This remediation technique, which is the focus of this study, differs from conventional pump & treat technology since it involves the flushing of contaminants by injecting additives together with water upgradient of the NAPL-contaminated area. The additives and contaminants are subsequently extracted downgradient for further ex-situ treatment. The most commonly applied remedial agents are surfactants and cosolvents (alcohols). Surfactant/cosolvent flushing strategies

rely on mobilization of NAPLs by increasing the solubility and decreasing the interfacial tension to increase the rate of NAPL mobilization.

A surfactant molecule is typically composed of a strongly hydrophilic head and a strongly hydrophobic tail group. Therefore, the entire surfactant monomer is often referred as amphiphilic because of its dual structure (Lowe et al., 1999). When a sufficient amount of surfactant is added to aqueous solution, monomers aggregate and form micelles that are spherical in shape and these micelles involve hundreds of surfactant monomers (Lowe et al., 1999). In a micelle structure, hydrophobic tail group cluster together toward the inner part of the micelle while hydrophilic head group remain outside in water. The threshold concentration that micelles begin to form is called the critical micelle concentration (CMC). Beyond the CMC, any added surfactants will not increase the number of monomers; they will give rise to the formation of excess micelles.

When a surfactant is added to an aqueous solution, the properties of the multiphase system change. For instance, interfacial tension between NAPL and water will decrease by reaching a minimum at the CMC (Lowe et al., 1999). Both the IFT and surface tension will remain unchanged at this minimum value as surfactant is added beyond the CMC (Figure 2.2).

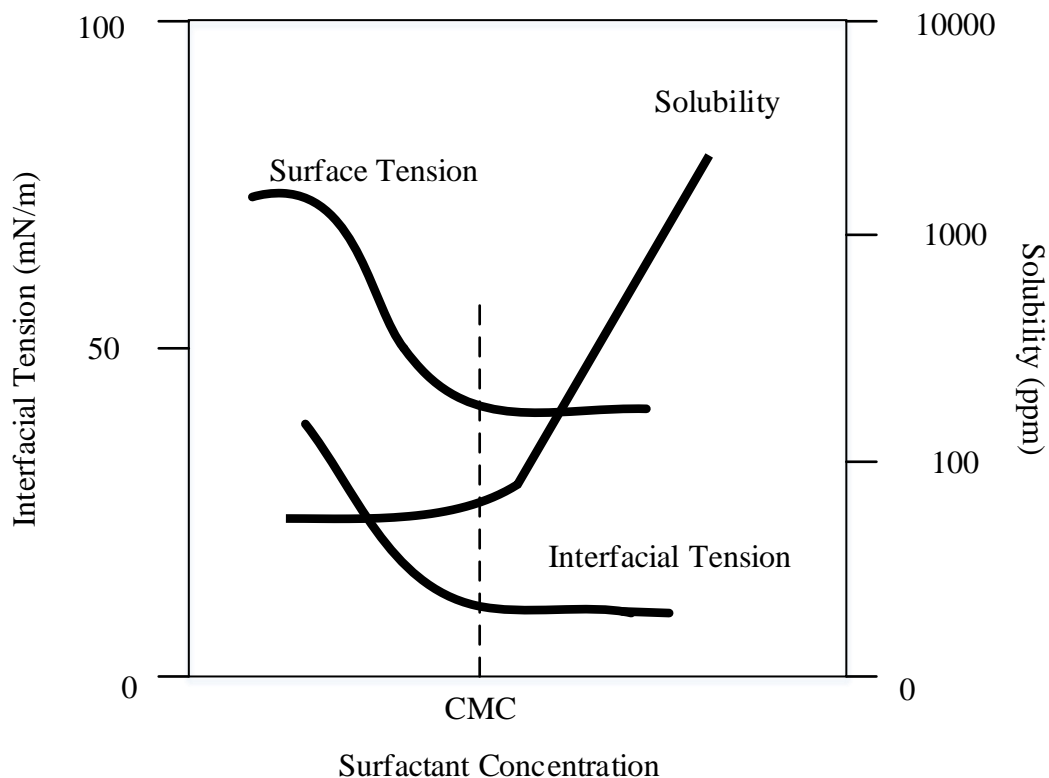


Figure 2.2. Variation of surface tension, solubility and interfacial tension with surfactant concentration (Lowe et al., 1999).

The polar exterior makes micelles highly soluble in water and the hydrophobic inner part of the structure is a sink of organic contaminant, thus leads to an apparent solubility enhancement for the organic contaminant that promotes mobility. The solubility of DNAPL increases dramatically as the surfactant is added beyond the CMC as a result of new micelle formation. A large number of studies have showed that, surfactant flushing is a promising technology for the DNAPL remediation when it is properly designed (Fortin et al., 1997; Hirasaki et. al., 2000; Sabatini et al., 2000; Abriola et al., 2005; Childs et al., 2006).

While surfactants may enhance the remediation efficiency of DNAPLs, some surfactants also introduce toxicity and refractory species into the system. For instance, cationic surfactants are known to be toxic in the mg/L range to a wide variety of aquatic organisms (West and Harwell, 1992). Therefore, the applied surfactants should have low toxicity and be biodegradable (Mulligan et al., 2001; West et al., 1992). The utilization of food grade surfactants (T-MAZ 28, T-MAZ 20, and T-MAZ 60) that are approved from Food and Drug Administration is suggested (Shiau et al., 1995). In recent years, biosurfactants have been widely used due to advantages such as biodegradability, low toxicity and better functionality in comparison to synthetic surfactants (Silva et al., 2014; Pacwa-Płociniczak et al., 2011).

In recent years, many researchers suggested the application of cosolvent flushing technologies in subsurface for the enhance remediation of DNAPLs trapped in the subsurface (Lunn and Kueper, 1999; Jawitz et al., 2000; Ramsburg et al., 2002; Hofstee et al., 2003; Brooks et al., 2004; Agaoglu et al., 2012; Aydin-Sarikurt et al., 2016). In cosolvent flushing, alcohol solutions in low concentration are injected (10 to 50 percent volume/volume) into the vadose zone, saturated zone or both in order to increase the aqueous solubility of many organic contaminants. The cosolvent mixture is injected upgradient of the NAPL zone. The degree of solubility enhancement of a system depends on both cosolvent concentration and specific component composition of DNAPL. Significant mobilization of DNAPL is not expected like in the case of high concentration of alcohol injection. If large amount of alcohol is added to a DNAPL-water system, alcohol changes the viscosity, density, solubility and IFT of the DNAPL (Imhoff et al., 1995; Lunn and Kueper, 1999). However, if sufficient amount of alcohol is added, complete solubilization of DNAPL can be reached. This behavior is illustrated by ternary-phase diagrams which depict the phase behavior of a multiphase system.

Mostly used alcohols in groundwater remediation are low molecular weight alcohols such as ethanol, 1-propanol and 2- propanol (Lowe et al., 1999). Other compounds such as humic acids and

cyclodextrins have also been evaluated for their potential to enhance DNAPL solubilization (Akyol and Turkkan, 2018). Johnson and John, (1999) reported that humic acids can enhance the solubility of DNAPLs but to a lesser extent than most surfactants. However, unlike surfactants they can solubilize contaminants irrespective of the humic acid concentration. Moreover, humic acids decrease IFT but to a lesser extent than surfactants which may be an advantage when downward mobilization of DNAPL is not desired. Wang and Brusseau (1993) investigated the solubility alteration of organic compounds by hydroxypropyl-beta-cyclodextrin (HPCD) in the aqueous phase. This study showed that there is a linear relationship between the solubility enhancement of the organic compounds and HPCD concentration.

Although the in-situ flushing is a promising technology for the rapid recovery of DNAPLs, there is a risk that manipulated mobilization by agents leads to the uncontrolled migration of DNAPL downward to the previously uncontaminated parts of the subsurface (Pennell et al., 1996). On the other hand, in-situ flushing applications have some problems and limitations when these technologies are upscaled to the field (Lowe et al., 1999). A major complication at the field scale is the heterogeneity of the soil properties which are typically not accounted for in most laboratory applications. Because the injected fluid will follow the path of least resistance, heterogeneity can cause the injected solution to bypass the DNAPL mass causing residual DNAPL to remain in the subsurface and continue to pose risk (Christ et al., 2005).

#### **2.4. Interphase Mass Transfer**

Interphase mass transfer between fluids in a multiphase system is a common process encountered in many industrial and natural systems. Interphase mass transfer can be explained as the transfer of components across the interface separating the different phases (Figure 2.3). Specifically in the area of NAPL remediation, significant efforts have been directed in recent years to elucidate the factors affecting the interphase mass transfer process (Imhoff et al., 1994; Kokkinaki et al., 2013a; Saba and Illangasekare, 2000; Agaoglu et al., 2015; Sarikurt et al., 2017). Much of the conducted researches define the interphase mass transfer by empirical expressions that are developed with laboratory experiments (Miller et al., 1990; Powers et al., 1992). However, these empirical expressions are mostly specific to the conditions present during laboratory experiments. Particularly under most field conditions, the local equilibrium assumption is not valid due to aquifer heterogeneity and NAPL zone by-passing. Therefore, it has become apparent in the literature that a rate-limiting expression is needed to realistically simulate the interphase mass transfer coefficient (Nambi and Powers, 2003; Soga et al., 2004; Marble et al., 2008; Aydin-Sarikurt et al., 2016).

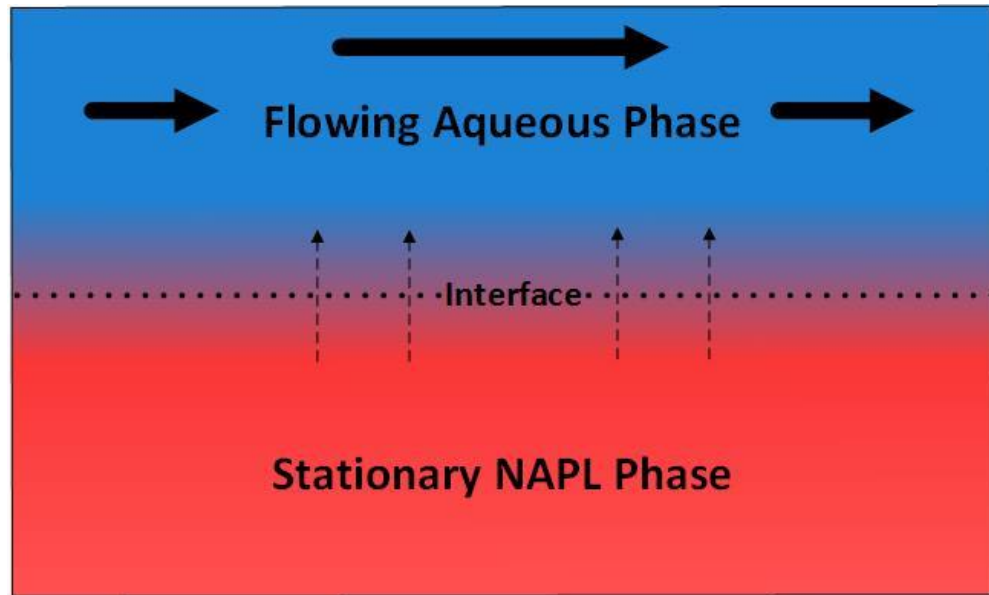


Figure 2.3. Schematic of the interphase mass transfer.

A common approach for modeling the interphase mass transfer between a stationary NAPL and the flowing aqueous phase is to express the interphase mass flux in terms of a linear driving force model (Miller et al., 1990; Powers et al., 1994b):

$$J = k_f a (C_s - C) \quad (2.1)$$

where

$J$ : interphase mass transfer rate due to NAPL dissolution per unit volume of porous media [M/L<sup>3</sup>-T]

$k_f$ : interphase mass transfer coefficient [L/T]

$a$ : interfacial area per unit volume of porous media [L<sup>2</sup>/L<sup>3</sup>]

$C_s$ : effective NAPL solubility [M/L<sup>3</sup>]

$C$ : aqueous phase concentration [M/L<sup>3</sup>].

The interphase mass transfer coefficient is commonly expressed in terms of Sherwood number ( $S_h$ ) that is correlated experimentally to system properties such as the flow parameters (expressed in terms of the Reynolds or Peclet numbers), grain diameter and NAPL saturation. The Sherwood number is defined as follows:

$$S_h = \frac{k_f d_m}{D_m} \quad (2.2)$$

where

$d_m$ : mean grain diameter of the porous medium [L]

$D_m$ : molecular diffusion coefficient [ $L^2/T$ ].

Sherwood number represents the ratio of the convective mass transfer to the rate of diffusive mass transport. If Sherwood number is high, convective mass transfer is high in the system.

A major challenge of the above approach for the modeling of interphase mass transfer is the inability to explicitly define the interfacial area,  $a$ , between the NAPL and aqueous phases. In practice, it is very difficult to observe the interfacial area because of the complex spatial distribution of NAPL which is controlled by the interaction of the hydraulic, gravitational and capillary forces that are in turn governed by the soil and fluid properties. To date, there are only two studies that have developed such Sherwood expressions for idealized NAPL distributions: Pfannkuch (1984) and Powers et al. (1994b). However, reliability of the data is low for these studies and, due to uncertainties in the experiments, the data is not recommended for the development of a mathematical expression for the prediction of dissolution as a function of velocity.

The difficulty in explicitly defining the interfacial area in porous media has led some researchers to incorporate the interfacial area within the interphase mass transfer coefficient yielding (Imhoff et al., 1994):

$$J = K_L(C_s - C) \quad (2.3)$$

where

$K_L = k_f a$ : the lumped interphase mass transfer coefficient [ $1/T$ ].

The lumped Sherwood number - also referred to as the modified Sherwood number ( $S_h'$ ) - corresponding to the lumped mass transfer coefficient is defined as:

$$S_h' = \frac{K_L d_m^2}{D_m} \quad (2.4)$$

In recent years, a substantial number of investigations were directed to correlate the lumped interphase mass transfer (through  $S_h'$ ) to fluid and porous medium properties (Miller et al., 1990; Imhoff et al., 1994; Powers et al., 1994a; Dillard and Blunt, 2000; Nambi and Powers, 2000; Saba

and Illangasekare, 2000; Held and Celia, 2001; Parker and Park, 2004; Schnaar and Brusseau, 2006; Maji and Sudicky, 2008; Agaoglu, 2015). These experiments are mostly derived from idealized laboratory experiments (Powers et al. 1994b; Brusseau et al. 2002; Agaoglu et al. 2015). Two examples of such Sherwood formulations developed by Saba and Illangasekare (2000) and Nambi and Powers (2003), respectively, are:

$$Sh' = 8Re^{0.28}S_n^{1.04} \quad (2.5)$$

$$Sh' = 37.15Re^{0.61}S_n^{1.24} \quad (2.6)$$

where

$Re$ : Reynolds number [-]

$S_n$ : initial NAPL saturation [-].

Reynolds number is defined as follows:

$$Re = vd_m/\mu_w \quad (2.7)$$

where

$v$ : velocity [L/T]

$\mu$ : aqueous phase kinematic viscosity [L<sup>2</sup>/T].

Reynolds number is the ratio of inertial forces to viscous forces. It is an important parameter that predicts if a flow condition will be laminar or turbulent. If  $Re$  is low, the viscous forces are dominant over the inertial forces then the flow is laminar.

The fluid properties most commonly considered in these models include a combination of the following parameters: the Reynolds or Peclet numbers, NAPL saturation, mean grain diameter, and the Schmidt number ( $S_c = \frac{\mu_w D}{\rho_w}$  where  $\mu_w$  and  $\rho_w$  are the dynamic viscosity and density of the aqueous phase, respectively). Examples of lumped Sherwood correlations from the literature derived from laboratory scale experiments and regression analyses are given in Table 2.1.

Table 2.1. Lumped Sherwood correlations from literature.

Correlation	Conditions	Reference
$Sh' = 12 Re^{0.75} \theta_n^{0.6} Sc^{0.5}$	Steady-state flow, glass bead column experiments for $0.016 \leq \theta_n \leq 0.07$ $0.0015 \leq Re \leq 0.1$	Miller et al., 1990
$Sh' = 150 \theta_n^{0.79} Re^{0.87}$ $Sh' = 340 \theta_n^{0.87} Re^{0.71} \left(\frac{x_d}{d_m}\right)^{-0.31}$	Steady-state flow, sand column $0 \leq \theta_n \leq 0.04$ $0.0025 \leq Re \leq 0.021$ $1.4 \leq \frac{x_d}{d_m} \leq 180$	Imhoff et al., 1995
$Sh' = 8 Re^{0.28} S_n^{1.04}$	2D cell experiments for NAPL pools $0.014 < Re < 0.17$	Saba and Illangasekare, 2000
$Sh' = 37.15 Re^{0.61} S_n^{1.24}$	Uniformly distributed NAPL ganglia $0.01 < S_n < 0.35$ ; $0.0048 < \theta_n < 0.168$ $0.018 < Re < 0.134$	Nambi and Powers, 2003

where  $Re$  is the Reynolds number,  $\theta_n$  is saturation of the organic phase,  $Sc$  is the Schmidt number defined as  $Sc = \mu_w / \rho_w D_m$ ,  $x_d$  is the travel distance into the region of residual organic phase, and  $d_m$  is the mean grain diameter;  $S_n$  is the initial NAPL saturation.

The attractive feature of the modified Sherwood correlations is that they have been used in cases when accurate estimates of the interfacial area between the two fluids are not available. On the other hand, lumping the interfacial area within the mass transfer coefficient limits the validity of the correlations to the specific conditions used in their development. A number of comparative studies have demonstrated that predictions made when developing these correlations can vary widely (Powers et al., 1994b; Maji and Sudicky, 2008; Kokkinaki et al., 2013b). The variations were attributed to the complex NAPL architecture, the hydrodynamics of the multiphase system and soil heterogeneity, highlighting the challenges of incorporating such expressions in real-life applications.

In a recent modeling approach referred to as the thermodynamics based model, interphase mass transfer was computed by combining the mass transfer coefficient,  $k_f$ , that is obtained from empirically derived Sherwood correlations, with the thermodynamics-based calculation of the

interfacial area (Grant and Gerhard, 2007a, 2007b; Kokkinaki et al., 2013a, 2013b). This approach has generated substantial interest in the field because it proposes to independently estimate the interfacial area using thermodynamics principles - specifically, from the capillary pressure saturation ( $P_c$ - $S_w$ ) curves that are incorporated in multiphase flow models. However the application of the thermodynamics requires an accurate expression of the non-lumped Sherwood correlation.

### 3. PURPOSE

As mentioned in the previous chapters of this dissertation, the presence of NAPLs in the subsurface is one of the most challenging contamination problems (Cohen and Mercer, 1993). Due to their low solubility and high interfacial tension, NAPLs can persist in the subsurface for decades and even for centuries. Conventional remediation techniques such as pump & treat are inefficient in the recovery of large fractions of NAPL mass because of entrapment of the NAPL in the porous media and their relatively low dissolution and degradation rates. Therefore, new technologies have been proposed in recent years for the accelerated removal of NAPLs entrapped in the subsurface. One of these technologies is in-situ cosolvent flushing, an innovative technology that has been developed to enhance the removal of NAPLs from subsurface.

The first major purpose of this study is to investigate the potential cosolvent-enhanced solubilization and mobilization of a DNAPL in saturated porous media. In order to achieve this purpose, intermediate-scale cosolvent flushing experiments were conducted. The DNAPL selected in this study was trichloroethylene (TCE), which is one of the most commonly encountered DNAPLs in porous media due to its extensive and widespread use as cleaning agent and metal degreaser (Stroo et al., 2003). The flushing solution consisted of ethanol-water mixtures with varying ethanol contents.

The specific objectives of the study are:

- Characterization of the ternary phase behavior of TCE-water-ethanol system including the measurement of interfacial tension, TCE solubility, and miscibility of the multiphase system as a function of ethanol concentration.
- Evaluation of the effect of cosolvent content, flow velocity, and pumping pattern (intermittent pumping versus continuous pumping) on TCE removal mechanism using an intermediate-scale tank.
- Investigation of the ability of a state-of-the-art multiphase flow modeling program to simulate cosolvent flushing for NAPL remediation under varying flow conditions.
- Estimation of the interphase mass transfer coefficient for flushing experiments and evaluation of the system properties on interphase mass transfer.

Moreover, a critical process influencing the effectiveness of NAPL mass recovery in the subsurface is the interphase mass transfer. The importance of the interphase mass transfer is obvious particularly when modelling the intermediate-scale flushing experiments in the first part of this dissertation. Therefore, the second major purpose of the study focuses on conducting controlled dissolution experiments from pooled NAPL to gain more insight into the mechanisms that affect interphase mass transfer. The DNAPL selected for this purpose was 1,2- dichlorobenzene (DCB) because of its low evaporation potential and low solubility.

The specific objectives of the dissolution experiments are:

- Investigation of the effects of flow velocity and porous media properties such as grain size diameter on interphase mass transfer.
- Interpretation of the dissolution experiments using a 2D pore network model in addition to a simplified 1D analytical solution. The 2D pore network computer program written in Fortran (listed in the Appendix) was developed as part of this study.
- Development of a revised correlation that can be used as a predictive tool for the estimation of rate-limited interphase mass transfer in future studies.

## 4. MATERIALS AND METHODS

This chapter describes the experimental methods and models used for the interpretation of the experiments. The chapter is organized as follows: Section 4.1 describes the batch tests conducted to characterize the multiphase NAPL-water-cosolvent system. Section 4.2 describes the intermediate-scale experiments conducted to demonstrate the impact of cosolvent content, velocity and pumping pattern on NAPL flushing in porous media. Section 4.3 describes the multiphase model used to simulate the cosolvent flushing experiments. Section 4.4 discusses the NAPL dissolution experimental setup. Section 4.5 presents the numerical model that was developed to simulate dissolution experiments leading to improved Sherwood number correlations.

### 4.1. Batch Experiments

In order to characterize the multiphase (DNAPL-water-cosolvent) system, batch tests were conducted. The measured parameters of the system were interfacial tension (IFT), solubility and miscibility by ternary phase diagram (TPD) as a function of cosolvent content. The considered DNAPL and cosolvent in this work were TCE and ethanol, respectively, both purchased from Sigma Aldrich. The batch test results were used to understand the performance of the ternary phase system (NAPL-water-cosolvent). The data were also used in the modeling of the experimental results which is described in Section 4.3.

#### 4.1.1. Interfacial Tension Measurements

The IFT between TCE and aqueous phase was measured using the Du-Nouy Ring Method with a KSV 703 digital tensiometer (Figure 4.1) at 20°C. The platinum ring was immersed into the TCE and aqueous phase mixture placed in the chamber and the IFT was measured by pulling the ring up by the tensiometer. Due to the sensitivity of the equipment on the changes of the system phase behavior, all of the IFT measurements were performed in triplicates. The measurements were conducted for different ethanol contents in the aqueous phase ranging from 0 to 65% by volume. Since the multiphase system was miscible at ethanol contents greater than 65%, IFT measurements were essentially zero at these ethanol contents.



Figure 4.1. Interfacial tension meter (KSV 703 Digital Tensiometer).

#### 4.1.2. Solubility Measurements

Solubility tests were performed to measure the solubility of TCE into the flushing solution. The measurements were conducted by following the method explained by Wang and Brusseau, (1993). 2 ml of TCE were put in glass vials containing 10 ml of flushing solution at different ethanol contents in the aqueous phase ranging from 0 to 60% by volume. The vials were sealed and settled into a horizontal shaker with a water bath at 20°C. After 48 hours of mixing in the shaker at 400 rpm, the equilibrium between two phases was attained. The vials were centrifuged at 3000 rpm for 20 min to achieve the phase separation. At the end, the dissolved TCE in the aqueous phase was analyzed using a Shimadzu UV-160A UV-vis spectrophotometer at a wavelength of 200 nm. All solubility experiments were performed in duplicates for quality control.

#### 4.1.3. Miscibility Measurements

The miscibility of the TCE-water-ethanol system was determined using ternary phase diagrams to evaluate the dissolution potential of the system components within different phases. The miscibility curve was formed on ternary phase diagram by following the “Cloud Point Titration” method (Martel et al. 1998; St-Pierre et al. 2004). The turning points between one-phase and two-phase regions were determined by the titration procedure. A mixture of components (TCE-water-ethanol) with known amounts was placed in a 40 ml glass vial capped with a teflon mini-valve to

minimize TCE losses due to evaporation. During the experiment, the solution was agitated by using a teflon coated magnetic stirrer to provide necessary mixing. Water and ethanol were gradually added to the mixture in the titration vial using gastight macro-syringes. The turning points were recorded by observing the change in transparency of the mixture. At the beginning, the solution was at the cloudy zone. After adding the ethanol, the mixture moved out of the cloudy zone to reach the one phase zone. In order to reach cloudy zone again, water was added. The volumes of the components that change the transparency of the solution were recorded as turning points. 10 points were used to draw the miscibility curve on a TPD. The titration procedure was performed at 20°C.

#### 4.1.4. TCE Analysis

The effluent samples at lower TCE concentrations (0.09-7.31 mg/L) were analyzed using a Perkin Elmer Clarus 600 Gas Chromatography equipped with mass spectrometer (GC-MS). TCE was first extracted from the aqueous phase by liquid-liquid extraction method using hexane (Wu and Ritchie, 2006). During hexane extraction, samples were prepared by adding 1 ml of aqueous phase solution to 3 ml of hexane into a glass vial and sealed immediately with Teflon coated caps. The vials were shaken for 2 min, equilibrated for 5 min for the phase separation, and then the extract was analyzed for TCE after the necessary dilutions. For GC analyses, the DB-5MS column (0.25  $\mu$ m, 30 m, 0.25 mm) was used. The oven temperature was set to 35 °C for 4 min then raised to 150°C with an increase of 40°C per minute. The samples were split injected (split ratio 1:50) at 250°C. The TCE peak detected at 3.61 min. This peak can be seen at Figure 4.2.

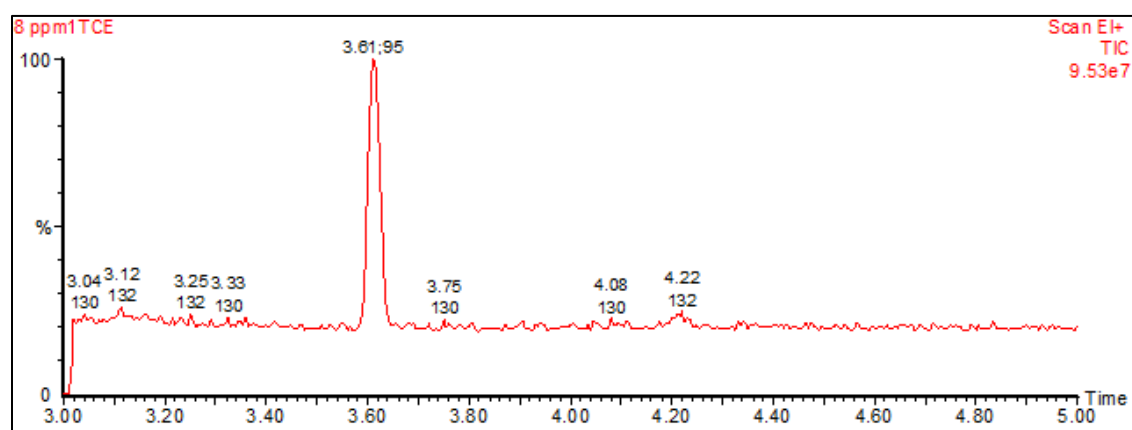


Figure 4.2. TCE peak obtained from GC-MS analysis.

The effluent samples at higher TCE concentrations (1-32 mg/L) were analyzed using a Shimadzu UV-160A UV-vis Spectrophotometer at a wavelength of 200 nm (Akyol et al, 2011).

## 4.2. Intermediate-Scale Flushing Experiments

Intermediate-scale flushing experiments were conducted in a 2D vertical plane tank (Figure 4.3). The purpose of using an intermediate-scale tank is to allow for a more realistic evaluation of the enhanced cosolvent flushing compared to columns because they allow for the downward migration of the DNAPL due to the density differences. The tank (L=0.8 m, H=0.4 m, W=0.05 m) was made of stainless steel with a glass front that enables a visual detection of TCE movement. Various ports were drilled in the back of the tank, to be used for TCE injection purposes. Three inlet and three outlet ports were drilled at both sides. The purpose of the three inlet ports and an upstream gravel chamber was to make the flow more uniform. The tank also has three outlet ports for sampling (Figure 4.3). The tank has a downstream chamber filled with gravel to prevent sand from exiting the tank and clogging the ports. The flow through the tank was attained by connection of a peristaltic pump with tubing to the inlet ports. Before filling the tank with sand, leaking test was conducted by filling the tank with water. No leaking was observed.

Before each flushing experiment, the tank was packed with clean and homogeneous sand. Packing of the tank was performed with dry sand in 1 cm increments to have a uniform distribution of the sand. The silica content of the sand was 98.6% SiO<sub>2</sub> with a mean grain diameter of 0.2 mm.



Figure 4.3. Front view of the intermediate-scale flushing tank.

At the beginning of the each flushing experiment, the compacted sand in the tank was saturated by deionized water for 48 h at a low flow rate of less than 2 ml/min to prevent the entrapment of air bubbles in the sand. The porosity of the sand was determined from the volume of the water needed to saturate the sand placed in the tank as 0.36. Another way to determine the porosity was from the

tracer tests (The tracer tests are described in Section 4.2.2). The result was consistent with the tracer test.

#### 4.2.1. Cosolvent Flushing Experiments

The flushing experiments were conducted with flushing solutions containing 0, 20, and 50% ethanol by volume for three different flow velocities and for two different pumping patterns. A list of conducted experiments is presented in Table 4.1. The flow velocities considered in these experiments were: 0.6 (low), 1.2 (intermediate), and 3.05 (high) m/day. These values are consistent with groundwater velocities in the field. Typical groundwater velocities under natural conditions are in the order of 0.1 to 1 m/day (Puls et al. 1999; Vogan et al. 1999; Salanitro et al. 2000). During cosolvent enhanced flushing, the velocities in the region between the injection and extraction wells would increase, possibly by a factor of 10. The effect of pumping pattern on NAPL recovery was evaluated by one of the experiments with intermittent injection of the flushing solution. In the intermittent experiment, repetitive cycles of flushing for 3 h followed by no flow for 1 h were applied.

At the beginning of each flushing experiment, a volume of 10 ml dyed TCE was gradually injected with gas tight syringes into the sand tank through the injection ports at the back of the tank. The injected TCE mass was dyed with Sudan IV (Sigma Aldrich) 0.01% by weight, for the visual inspection of the contaminant plume in the sand. After the injection of TCE, the flushing solution (with known cosolvent content) was injected from the inlet ports at the inlet side of the tank using a peristaltic pump (Masterflex) and viton tubing (Cole Parmer). For each experiment, 2 pore volumes of flushing solution was injected to the tank. The flow was maintained steady through the experiment. Temporal samples were collected individually from the three outlet ports. The collected effluent samples were analyzed as explained in the TCE Analysis section of this dissertation.

Table 4.1. List of tank flushing experiments.

<b>Experiment</b>	<b>Ethanol content (v%)</b>	<b>Flow velocity (m/day)</b>	<b>Pumping pattern</b>
1	0	3.05 (high)	continuous
2	20	3.05 (high)	continuous
3	50	3.05 (high)	continuous
4	50	1.2 (intermediate)	continuous
5	20	3.05 (high)	intermittent
6	50	0.6 (low)	continuous

#### 4.2.2. Tracer Tests

In order to evaluate the transport characteristics of the tank system, tracer tests were performed using 0.01 M NaCl at two different velocities: 3.2 m/day (high) and 1 m/day (low). NaCl was chosen as the tracer since it is a non-reactive species that does not undergo any sorption. The velocity of the flow was calculated with the following equation (4.1):

$$v = \frac{Q}{n A} \quad (4.1)$$

where

$v$ : velocity [L/T]

$Q$ : flow rate [L<sup>3</sup>/T]

$n$ : porosity of the porous media [-]

$A$ : cross sectional area of the tank [L<sup>2</sup>]

Two pore volumes of the tracer solution were injected through the inlet ports. The effluent samples were collected at 45-min intervals and the electrical conductivity of the samples were measured using a conductivity probe. The experimental data were compared with the solution of the 1D advection-dispersion equation given in equation (4.2):

$$C = \frac{C_0}{2} * erfc \left( x - \frac{vt}{2\sqrt{Dt}} \right) \quad (4.2)$$

where

$C_0$ : influent concentration [M/L<sup>3</sup>]

$D$ : dispersion coefficient [L<sup>2</sup>/T]

$x$ : length in the direction of flow [L]

$t$ : time [T]

The dispersion coefficient in the porous media is defined as the sum of the molecular diffusion and the mechanical mixing (Fetter, 1999). The mechanical mixing is a linear function of the velocity and the dispersivity (Equation 4.3):

$$D = \alpha V + D_m \quad (4.3)$$

where

$\alpha$ : dispersivity [L]

$D_m$ : molecular diffusion coefficient [ $L^2/T$ ]

The dispersion coefficient was determined such that the RMSE (root mean square error) of the sum of the squares difference between the measured and predicted effluent concentrations is minimum. This was achieved by minimizing the RMSE between the measured and simulated concentrations.

For the visualization of the tracer solution and to determine if preferential flow pathways existed in the tank, the injected NaCl solution was dyed with bromocresol green (Sigma Aldrich) which is a non-reactive dye. The dyed tracer tests were conducted with one pore volume solution and at high velocity. The movement of the dyed tracer solution was monitored using a camera. The purpose here was to confirm that the tank was compacted uniformly and that no preferential flow paths exist that can lead the injected flushing solution to bypass the NAPL zone.

### 4.3. Modelling

#### 4.3.1. Model Description

The flushing solution experiments were simulated using a multiphase model called UTCHEM. UTCHEM is a three-dimensional, multiphase, multicomponent, compositional, and finite difference numerical model. The model is capable of modeling cosolvent flushing and was originally developed by Pope and Nelson to simulate the enhanced recovery of oil using surfactant and polymer processes (Pope and Nelson 1978). Roeder and Falta (2001) modified the UTCHEM code, to model unstable conditions which may occur during cosolvent flushing of DNAPLs. Since a cosolvent (ethanol) was used in this study, a modified version of the multiphase flow simulator UTCHEM-9.0 was used in the modelling part of this study. This modified version included the interfacial tension calculation method for cosolvents developed by Li and Fu (1992) and implemented by Liang and Falta (2008). By this method, UTCHEM enables to simulate cosolvent concentration-dependent interfacial tension lowering such as that occurring in the flushing experiments.

UTCHEM accounts for effects of surfactant/cosolvent on interfacial tension, phase behavior, capillary trapping, and surfactant/cosolvent adsorption. Capillary pressures, relative permeability,

dispersion, molecular diffusion, and the partitioning of NAPL to the aqueous phase (under equilibrium and nonequilibrium assumptions) are some of the important components of the simulator that were utilized in this work. These components are described in the following subtitles.

4.3.1.1. Capillary Pressure. The capillary pressure was calculated by the Brooks–Corey method which can be defined as the following equation (Brooks and Corey, 1966):

$$\left(\frac{P_{bl}}{P_{cll'}}\right)^\lambda = 1 - S_{nl'} \quad (4.4)$$

where

$P_{bl}$ : bubbling pressure for phase  $l$  [M/L-T<sup>2</sup>]

$P_{cll'}$ : capillary pressure between phase  $l$  and  $l'$  [M/L-T<sup>2</sup>]

$S_{nl'}$ : standardized saturation [-]

$\lambda$ : pore size distribution coefficient [-]

The capillary pressure function is scaled with respect to interfacial tension, porosity, and permeability (Brooks and Corey, 1966). The flushing solution injection process is assumed to be in the imbibition direction for the entire injection period (Delshad et al., 1996). The entry pressure for TCE is determined using the Young–Laplace equation with a contact angle of 20° (highly hydrophilic medium). The computed entry pressure of 5.032 kP showed good agreement with the literature (Eichel et al., 2005). The pore size distribution index was taken as 2 which is a typical value for fine sand (Agaoglu et al., 2012).

4.3.1.2. Relative Permeability. The Brooks-Corey formulation, which is scaled by the interfacial tension, was used to compute the relative permeability for each phase (Brooks and Corey, 1966). The interfacial tension in the presence of ethanol was computed according to the correlation of Li and Fu (1992). This correlation is adapted to NAPL/cosolvent problems by Liang and Falta (2008).

$$\sigma = \sigma_0 \left(\frac{X}{X_0}\right)^{k_{Li\&Fu}} \quad (4.5)$$

$$X = \log(C_n^w + C_w^n + C_p^c) \quad (4.6)$$

$$X_0 = X \text{ when } C_p^c = 0$$

where

$\sigma$ : interfacial tension when a cosolvent is present [M/T<sup>2</sup>]

$\sigma_0$ : interfacial tension in the absence of a cosolvent [M/T<sup>2</sup>]

$k_{Li&Fu}$ : exponent of the IFT expression [-]

$C_n^w$ : water concentration in the NAPL phase [M/L<sup>3</sup>]

$C_w^n$ : NAPL concentration in the aqueous phase [M/L<sup>3</sup>]

$C_p^c$ : cosolvent concentration in the cosolvent poor phase (in this case, the cosolvent poor phase is the NAPL phase) [M/L<sup>3</sup>]

4.3.1.3. NAPL Partitioning. In this study, the dissolution of TCE into aqueous phase was modeled in two ways: (i) local equilibrium and (ii) as a non-equilibrium process. There is increasing evidence in the literature that the local equilibrium assumption over-estimates the NAPL dissolution (e.g., Marble et al., 2008). In this study both methods were tested. For non-equilibrium mass transfer, a linear mass transfer expression (by Powers et al., 1992) was used. For this expression, NAPL solubility and the lumped mass transfer coefficient are the input parameters. When the NAPL is dissolved into the aqueous phase (cosolvent+water), Hand's equation is used to determine the equilibrium solubility value used in the rate limited mass transfer term.

4.3.1.4. Ternary Phase Diagram. Ternary phase diagram is used to model the cosolvent phase behavior (Hand, 1939). Hand's rule is based on the empirical observation that equilibrium phase concentration ratios are straight lines on a log-log scale. The binodal curve is computed by:

$$\frac{C_{3l}}{C_{2l}} = A_e \left( \frac{C_{3l}}{C_{1l}} \right)^B \quad l = 1,2,3 \text{ and } A_e = \left( \frac{2C_{3max}}{1 - C_{3max}} \right)^2 \quad (4.7)$$

where

$C_l$ : concentration of each component in each phase [M/L<sup>3</sup>]:  $l=1$  is the aqueous phase,  $l=2$  is the NAPL phase, and  $l=3$  is the microemulsion.

$A_e$ : empirical parameter that depends on  $C_{3max}$  [-]

$C_{3max}$ : maximum height of the binodal curve of the TPD [-]

$B$ : empirical parameter that depends on the shape of the binodal curve [-] (Liang and Falta 2008)

### 4.3.2. Model Development

In order to simulate the NAPL flushing experiments in the intermediate tank, the model domain was discretized into 2220 (30 rows and 74 columns) equally spaced gridblocks. The water saturation was initially assumed 1 everywhere except in the NAPL zone. The NAPL zone dimension were 5 cm length and 5 cm height which based on visual inspection (Figure 4.4). Within the NAPL injection zone the pore volume can be estimated as  $0.36 \times 5 \times 5 \times 5 = 45 \text{ cm}^3$ , leading to a NAPL saturation of 0.22 and water saturation of 0.78 based on an injected NAPL volume of 10 ml. Since it is difficult to accurately define the NAPL zone dimensions, sensitivity simulations were also conducted with an initial NAPL zone of 3 by 3 by 5 cm (5 cm being the thickness of the tank), leading to an initial NAPL saturation equal to 0.61.

Boundary conditions corresponded to water levels of  $h_1 = 30 \text{ cm}$  on the left side of the main tank and  $h_2 = 25 \text{ cm}$  on the right side were used in the model. These corresponded to the water levels at the inlet and outlet sides of the tank. The boundary conditions were implemented by defining pseudo-wells (injection well and production well) on either side of the model. Prescribed flow rates were defined at the two wells corresponding to the flow rates used in the flushing experiments. Flow in the model was presumed to be unconfined as in the experiments.

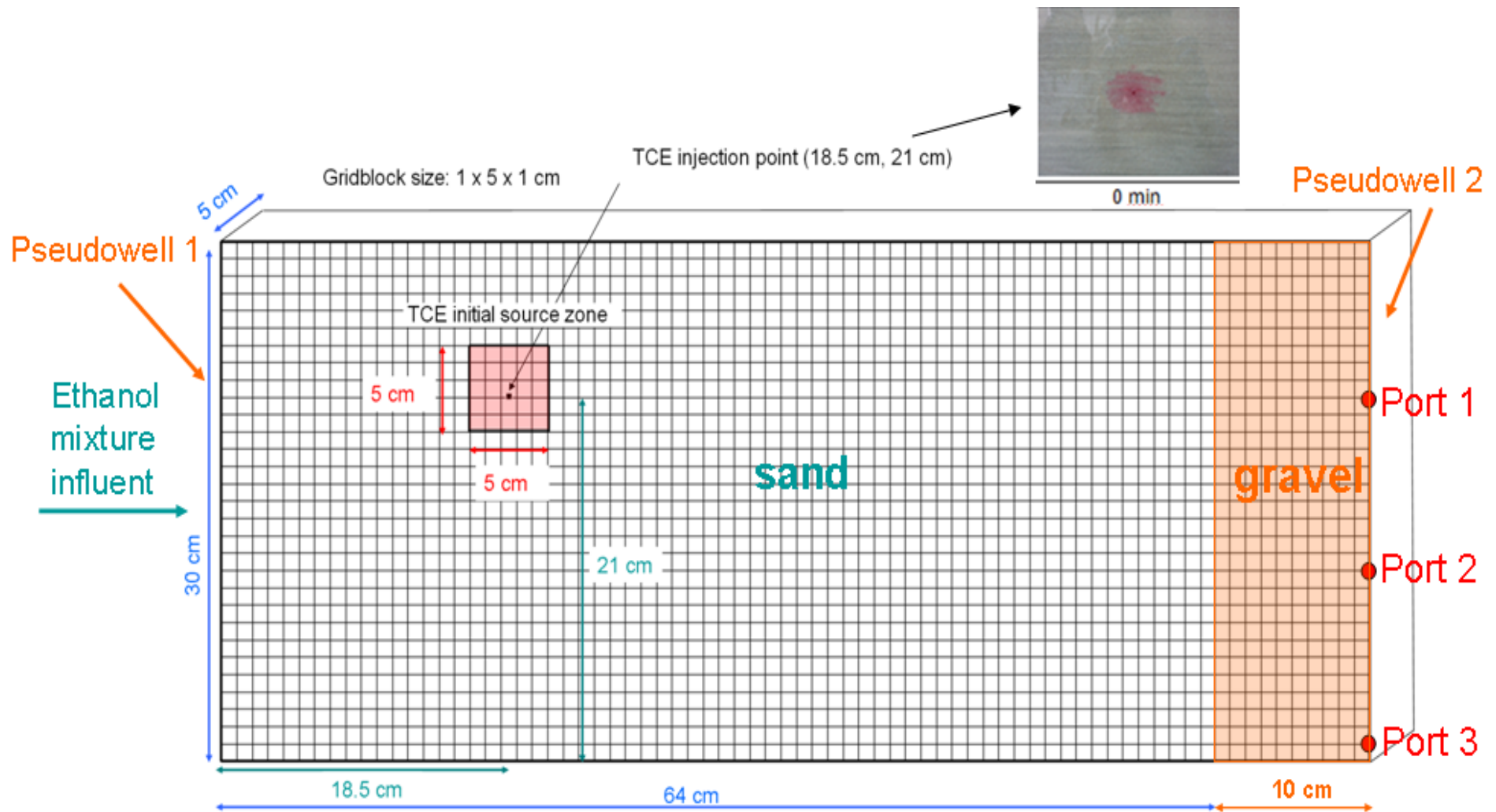


Figure 4.4. Model discretization and TCE injection point and source zone.

#### 4.4. Flow Cell Experiments

As it was comprehensively stated earlier in this dissertation, the critical process that controls the persistence of NAPLs in the subsurface and the effectiveness of any in-situ remediation action is the rate of interphase mass transfer. During the intermediate-scale flushing experiments, it was observed that robust expressions defining the interphase mass transfer in porous media are lacking in the literature. In order to fill this gap and gain further insight on the interphase mass transfer mechanism, dissolution experiments were conducted. The influences of pore-scale medium characteristics and flow velocity on interphase mass transfer were investigated through these experiments.

##### 4.4.1. Dissolution Experiments

The dissolution experiments were conducted in a specially-designed vertical plane flow cell with dimensions of  $L=0.1$  m,  $H=0.04$  m,  $W=0.04$  m. The flow cell was made of stainless steel with a glass front to enable visual detection of NAPL injection and emplacement (Figure 4.5).

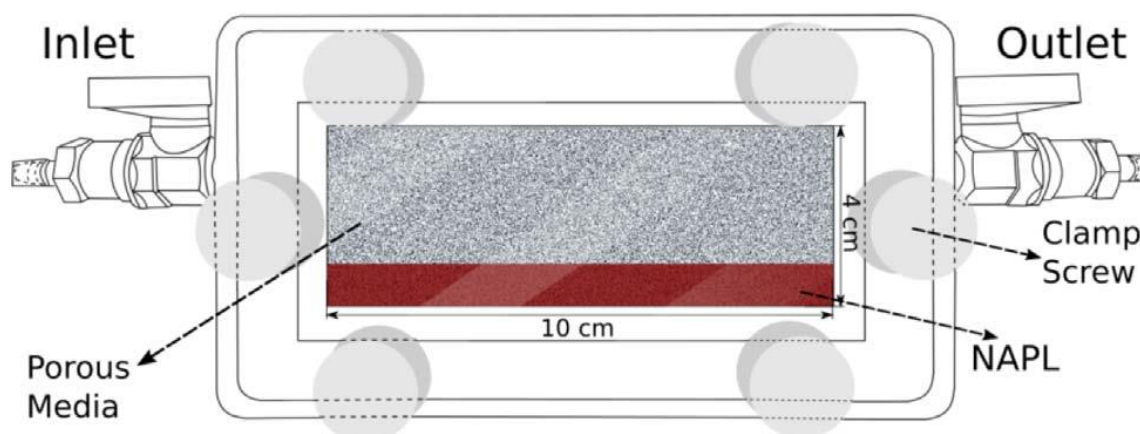


Figure 4.5. Sketch of the flow cell.

In the experiments, the target was to place the NAPL pool in the bottom part of the flow cell with water flowing horizontally over the immobile NAPL zone. The NAPL selected for these experiments was 1,2-dichlorobenzene (DCB) (purchased from Sigma Aldrich) because of its low evaporation potential and low solubility (saturation vapor pressure= 1.36 mm Hg at 25°C, Daubert et al., 1998; aqueous solubility of DCB =156 mg/L, Banarjee, 1980). Dissolutions experiments were conducted for two different porous media (sand or glass beads) (Figure 4.6) and for a wide range of flow velocities. At the beginning of the each experiment, the flow cell was packed with clean glass beads or sand with a mean grain diameter of 1 mm and 0.2 mm, respectively, as specified by the

supplier. The velocities considered in these experiments ranged over almost 2-3 orders of magnitude: from  $6.4 \times 10^{-6}$  to  $1 \times 10^{-3}$  m/s (corresponding to  $Pe = 1.3$  to 216) for the sand experiments and from  $8.7 \times 10^{-6}$  to  $1 \times 10^{-3}$  m/s (corresponding to  $Pe = 8.7$  to 980) for the glass bead experiments. These ranges are consistent with other dissolution studies such as Pfannkuch (1984) and Powers et al. (1994b).

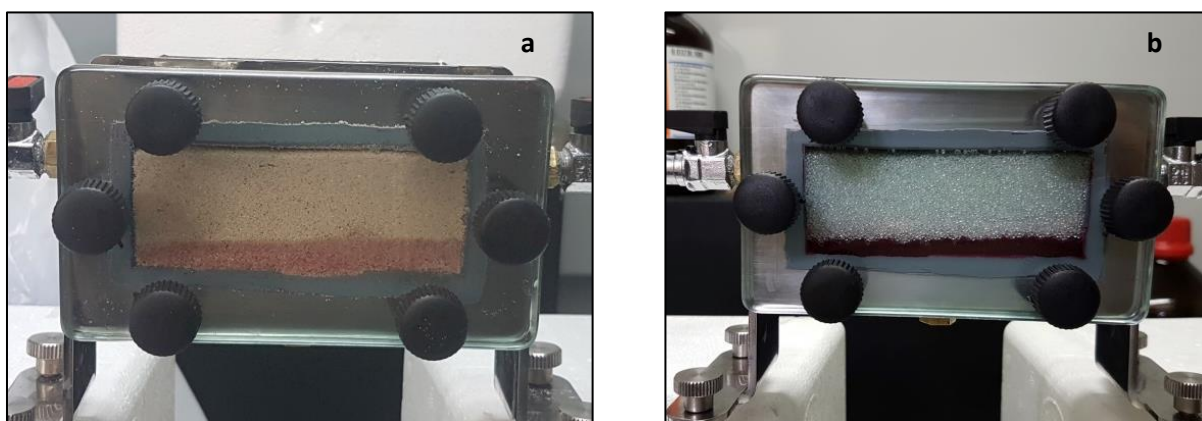


Figure 4.6. Flow cell compacted with two different porous media a) sand and b) glass beads.

For visualization of the NAPL mass, the injected DCB was dyed with Sudan IV (Sigma Aldrich) 0.01% by weight. After the compaction of the flow cell, a volume of 5 ml DCB was gradually injected with gas tight syringes into the flow cell through an injection port located at the bottom of the tank. It was observed that the injected DCB remained in the lower part of the medium providing a near flat interfacial area. Throughout the dissolution experiments, it was also observed that the NAPL was immobile and that the interfacial area between two phases did not change. Consequently, the interfacial area was assumed to be constant, equal to  $A = nLW$  where  $n$  is the porosity and  $L$  and  $W$  are the length and width of the flow cell, respectively. The flow cell was connected to a peristaltic pump with tubing from the inlet port. After the DCB injection, two pore volumes of water was injected from the inlet port at a side of the tank using the peristaltic pump at a constant rate. Two pore volumes of water was sufficient to reach equilibrium effluent concentrations. All experiments were conducted at a temperature of 20 °C. Temporal samples were collected individually from the outlet port. The DCB effluent samples were analyzed using a Shimadzu UV-160A UV-vis spectrophotometer at a wavelength of 220 nm. All measurements were performed multiple times (6-12 times) and the values reported were the average of all measurements.

#### 4.4.2. Tracer Tests

Prior to the dissolution experiments, tracer tests were performed to estimate the dispersivity and porosity of the porous media in the flow cell. The tracer experiments were conducted for both porous media, at two different velocities:  $1.5 \times 10^{-4}$  m/day (high) and  $2.5 \times 10^{-5}$  m/day (low). Two pore volumes of 0.01 M NaCl tracer solution was injected through the inlet port and the effluent samples were collected in 1 and 4 min intervals for the high and low flow rate experiments, respectively. The collected NaCl samples were measured in terms of the electrical conductivity using a conductivity probe. The longitudinal dispersion coefficient was calculated using the pore network model (described in the following section) assuming no NAPL is present. The determined dispersion coefficient was also confirmed with the analytical 1D advection-dispersion equation (Fetter, 1999). The molecular diffusion coefficient, needed to calculate the dispersivity, was assumed to be  $D_m = 1 \times 10^{-9}$  m<sup>2</sup>/s (Gabler et al., 1996).

#### 4.5. Estimation of the Mass Transfer Coefficient and Development of Sherwood Correlation

The 1D steady-state transport equation of dissolved species in the aqueous phase, assuming that dispersion can be ignored, can be written as (Powers et al., 1994b):

$$nv \frac{\partial C}{\partial x} = k_f a (C_s - C) \quad (4.8)$$

where

$n$ : porosity of the porous media [-]

$x$ : length coordinate in the direction of flow [L]

$k_f$ : interphase mass transfer coefficient [L/T]

$a$ : interfacial area per unit volume of porous media [1/L]

$C_s$ : effective NAPL solubility [M/L<sup>3</sup>]

$C$ : aqueous phase concentration [M/L<sup>3</sup>].

Integrating Equation (4.8) yields an analytical expression for the interphase mass transfer:

$$k_f = - \left( \frac{nv}{La} \right) \ln \left( 1 - \frac{C_{eff}}{C_s} \right) \quad (4.9)$$

where

$C_{eff}$ : steady-state effluent concentration at the downstream end of the NAPL zone ( $x=L$ ) which is determined from the flow cell experiments [M/L<sup>3</sup>]

$L$ : length of the flow cell (=0.1 m) [L]

$a$ : contact area between the mobile aqueous phase and the entrapped NAPL per unit volume of porous media. For the current flow configuration assuming the NAPL surface is flat, the contact area per unit volume of porous media is:  $a = \frac{nL}{HL} = \frac{n}{H}$  where  $H$  is the height of the aqueous phase flow area.

Once  $k_f$  is calculated for a particular dissolution experiment with the above analytical solution (Equation 4.9), the corresponding Peclet ( $Pe$ ) and Sherwood numbers are calculated as:

$$Pe = \frac{vd_m}{D_m} \quad (4.10)$$

$$Sh = \frac{k_f d_m}{D_m} \quad (4.11)$$

$Pe$  number relate the effectiveness of mass transport by advection to the effectiveness of mass transport by diffusion. If  $Pe$  is small, diffusion is considered as the dominant transport mechanism and if  $Pe$  is large advection is dominated.

In addition to the 1D analytical solution, the interphase mass transfer coefficient was estimated using a two-dimensional pore network model along a vertical plane. The model simulates the aqueous phase transport above the NAPL emplaced at the bottom of the flow cell. Flow is assumed to be uniform with no flow occurring through the NAPL phase. The pore network model is assumed to consist of chambers representing individual pores connected to each other through a network of throats (Lenormand et al., 1988). A schematic of the pore network used to simulate the dissolution experiments is shown in Figure 4.7. Given the uniform grain size and packing, a regular structured network with coordination number of 4 (i.e., any chamber is connected to adjacent chambers through 4 tubes) was used to simulate the dissolution experiments (Joekar-Niasar and Hassanizadeh, 2012).

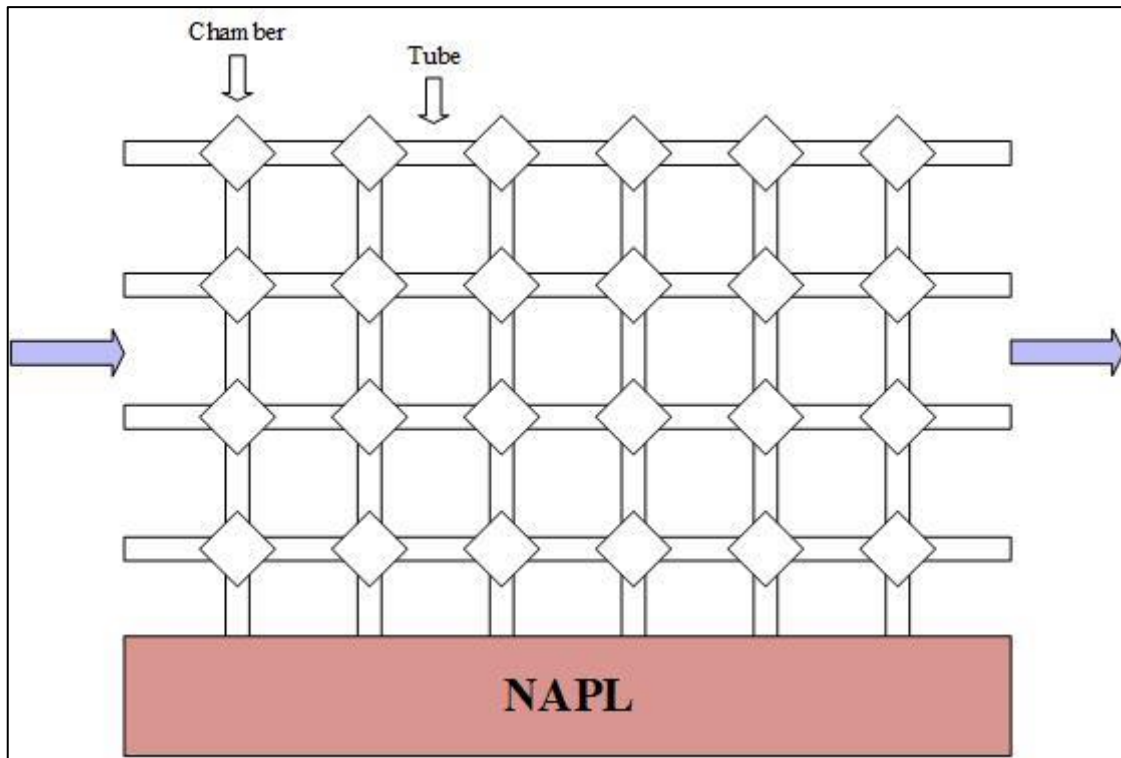


Figure 4.7. Pore network model used to simulate NAPL dissolution.

The transient two-dimensional equation describing the transport through the pore network model is based on the model developed by Jia et al. (1999) and used in other studies (e.g., Dillard and Blunt, 2000; Agaoglu et al., 2016). The change in concentration of chamber  $i$  as a function of time can be written as follows:

$$V_s \frac{\partial C_i}{\partial t} = \sum_{m=1}^M \{Q_m C_m\} + \sum_{m=1}^M \left\{ DA \frac{\Delta C_{im}}{l} \right\} + k_f A (C_s - C_i) \quad (4.12)$$

where

$i$ : chamber index

$V_s$ : volume of chamber  $i$  [ $L^3$ ]

$C_i$ : aqueous-phase concentration in chamber  $i$  [ $M/L^3$ ]

$M$ : number of adjacent chambers

$Q_m$ : flow rate into/out of chamber  $i$  to adjacent chambers [ $L^3/T$ ]

$C_m$ : concentration associated with  $Q_m$  [ $M/L^3$ ]

$D$ : dispersion coefficient [ $L^2/T$ ]. The dispersion coefficients in the longitudinal and lateral (vertical) directions were defined based on the tracer tests.

$\Delta C_{im}$ : difference in concentration between chamber  $i$  and adjacent chambers  $m$  [ $M/L^3$ ]

$k_f$ : mass transfer coefficient (along the water-NAPL interface only) [ $L/T$ ]

$C_s$ : aqueous phase solubility [ $M/L^3$ ]

$l$ : length of the tube connecting chamber  $i$  to adjacent chambers [L]

$A$ : cross-sectional area of the tube connecting chamber  $i$  to adjacent chambers [ $L^2$ ]

The primary difference between the pore network model described through Equation 4.12 and a 2D continuum scale transport equation is that the former accounts for the configuration of individual pores and their shapes through the chamber volumes and tube length parameters. On the other hand, 1D analytical solution (Equation 4.8) accounts for advection in the direction of flow; however, it completely ignoring dispersion.

The model domain extended over the aqueous phase area (0.03 m height by 0.1 m length). The concentration was simulated until steady state condition is achieved. The best fit mass transfer coefficient was determined such that the steady-state concentration at the end of a simulation is equal to the observed concentration from the dissolution experiments.

The input parameters used in the pore network model are given in Table 4.2. The porosity and dispersivity values were determined from the tracer tests which are discussed in the following section. Given the uniform porous media used in these experiments, the pore chambers were assumed to have a cubical shape, which are commonly used in pore network models (Dillard and Blunt, 2000; Joeekar-Niasar and Hassanizadeh, 2012) with dimension  $L_c = 0.7 d_m$ . This yields a total chamber volume that is  $0.7^3 = 0.343$  of the total domain size, approximately equal to the porous media porosity as determined from the tracer tests. The tubes connecting the chambers were assumed to have a square cross section area,  $A$ , and length,  $l$ . The length of the tubes was assumed to be 30% of the mean grain diameter:  $l = 0.3 d_m$ , while the cross-sectional area of the tube was defined as  $A = (0.5 d_m)^2$ . These values are consistent with suggested values in the literature for unconsolidated porous media such as the sand and glass beads used in this study (e.g., Dillard and Blunt, 2000; Agaoglu et al., 2016).

The model boundary conditions were as follows. The inflow concentration was assumed to be equal to zero. Along the bottom boundary, NAPL dissolution (Equation 2.1) was imposed. At the downgradient and top boundary, a zero concentration gradient was imposed. The model was solved explicitly in time until steady-state concentrations were obtained. Aqueous phase flow was assumed to be uniform over the NAPL. It was further assumed that the NAPL mass did not decrease with time which is a reasonable assumption given the low solubility of the DCB and the relatively small flushing volume (2 pore volumes) of each experiment.

To validate the model, several test runs were conducted. First, it was confirmed that the model agrees with the analytical 1D solution of Ogata and Banks (Fetter, 1999) for the case of influent contaminated water without the presence of any NAPL in the flow cell. Second, the analytical solution was compared to model simulations for the case when lateral transport (along the height of the flow cell) is ignored. Finally, for all simulations, mass balance for individual chambers and for the entire domain was checked to confirm that the solute mass balance is indeed conserved.

Table 4.2. Input parameters of pore network model for the two different porous media.

<b>Input parameters</b>	<b>Glass beads</b>	<b>Sand</b>
<b>Porosity</b>	0.34	0.36
<b>Longitudinal dispersivity (m)</b>	0.002	0.002
<b>Mean grain diameter (m)</b>	0.001	0.0002
<b>Chamber dimensions (m)</b>	0.0007	0.00014
<b>Chamber volume (m<sup>3</sup>)</b>	$3.43 \times 10^{-10}$	$2.74 \times 10^{-12}$
<b>Length of tube (m)</b>	0.0003	0.00006
<b>Area of tube (m<sup>2</sup>)</b>	$2.5 \times 10^{-7}$	$1 \times 10^{-8}$

## 5. ENHANCED DNAPL SOLUBILIZATION IN SATURATED POROUS MEDIA AND NUMERICAL MODELLING <sup>1</sup>

In this chapter, the results of the enhanced DNAPL recovery experiments and the numerical modelling are presented and discussed. The chapter is organized as follows: Section 5.1 gives the calibration curve used in the determination of the TCE concentrations. Section 5.2 presents results of the batch tests. Section 5.3 gives the results of the intermediate-scale experiments conducted in a 2D tank. Section 5.4 presents the results obtained from the multiphase model used to simulate the cosolvent flushing experiments.

### 5.1. Calibration Curve of TCE

As mentioned previously in the Materials and Methods section, the effluent samples from the cosolvent flushing experiments at lower TCE concentrations were analyzed using GC-MS. The calibration curve was achieved for TCE standards in hexane that have a concentration range of 0.09-7.31 mg/L. Figure 5.1 presents the calibration curve used for the quantification of the TCE.

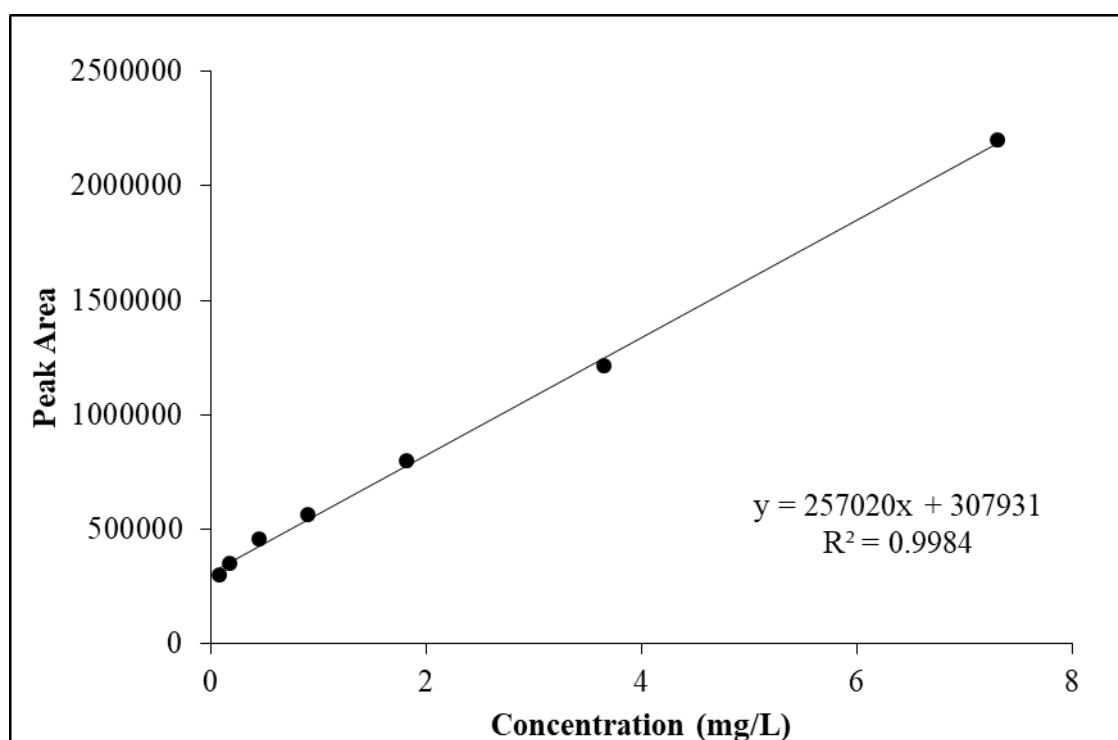


Figure 5.1. TCE calibration curve for GC-MS.

<sup>1</sup> The results presented in this chapter were published in Water, Air, & Soil Pollution (Aydin-Sarikurt et al., 2016).

The effluent samples at higher TCE concentrations were analyzed using UV-vis spectrophotometer at a wavelength of 200 nm. The calibration curve range was between 1-32 mg/L for the UV-vis spec analyses (Figure 5.2). For the range of concentrations considered, the correlation coefficient  $R^2$  of both calibration curves for TCE exceeded 0.99 indicating good fit to a straight line.

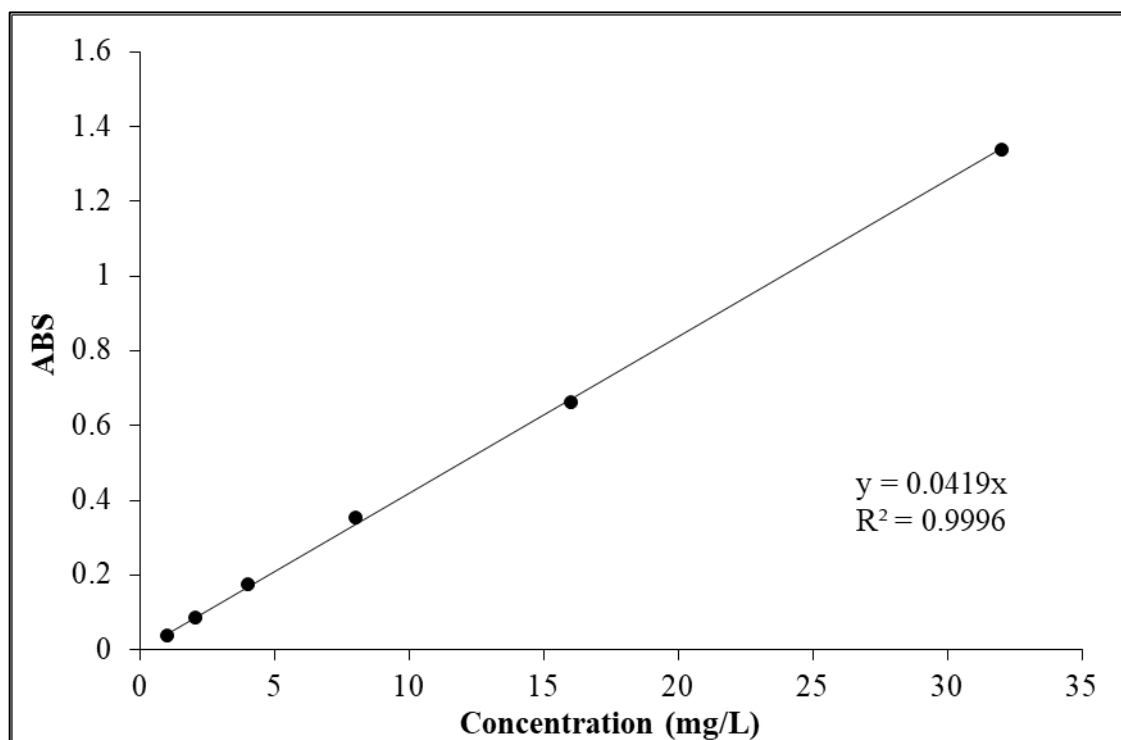


Figure 5.2. TCE calibration curve for UV-vis Spectrophotometer.

## 5.2. Batch Experiments

The results of the batch tests are presented in this section. As mentioned in the previous chapter, batch tests were conducted to characterize the multiphase system. The results of the batch experiments were used to gain more insight into the behavior of the multiphase system and to define some of the input parameters of the multiphase model.

### 5.2.1. Interfacial Tension Measurements

The measured IFT between TCE and aqueous phase as a function of ethanol content is shown in Figure 5.3. The IFT gradually decreases with increase in ethanol content. The significantly decreased IFT at ethanol contents higher than 50% indicates that such high ethanol content would

induce TCE mobility under normally encountered pressure gradients. At lower ethanol contents, the IFT remains high and TCE mobilization is not expected to occur.

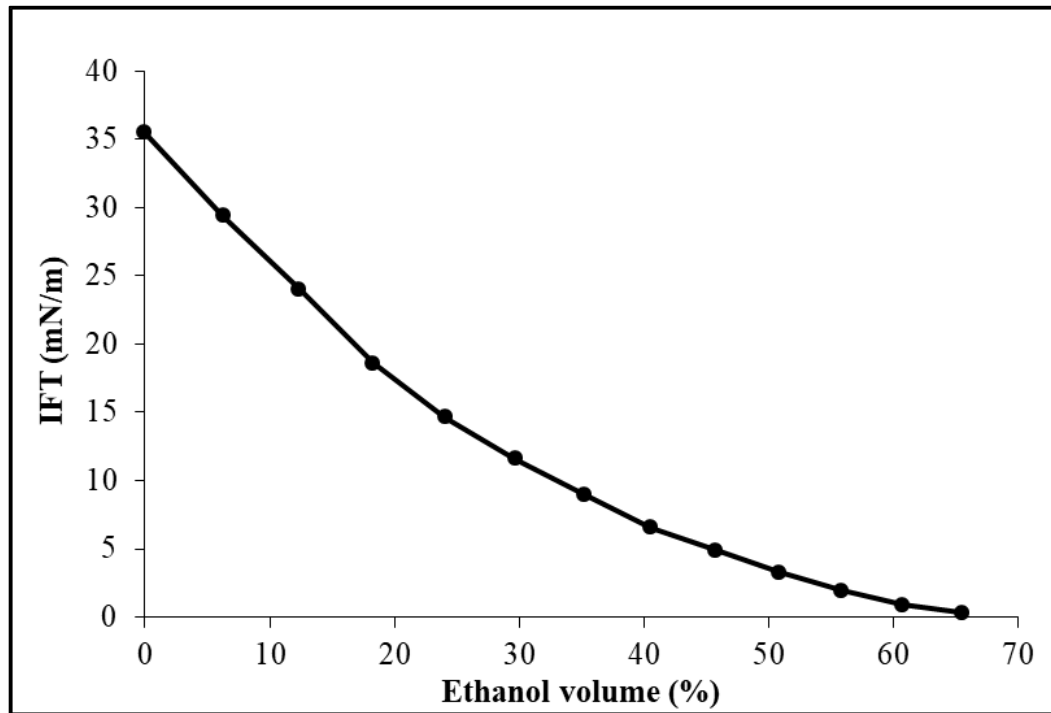


Figure 5.3. Interfacial tension between TCE and the aqueous phase as a function of ethanol content (% by volume) in the aqueous phase.

### 5.2.2. Solubility Measurements

The measured solubility of TCE for ethanol contents ranging from 0 to 60% by volume are presented in Figure 5.4. For relatively small ethanol contents, the TCE solubility showed only small increase with the ethanol content. The solubility of TCE increased rapidly for ethanol contents greater than about 30% in the flushing solution. TCE solubility increases up to 19,000 mg/L for ethanol contents of 50%.

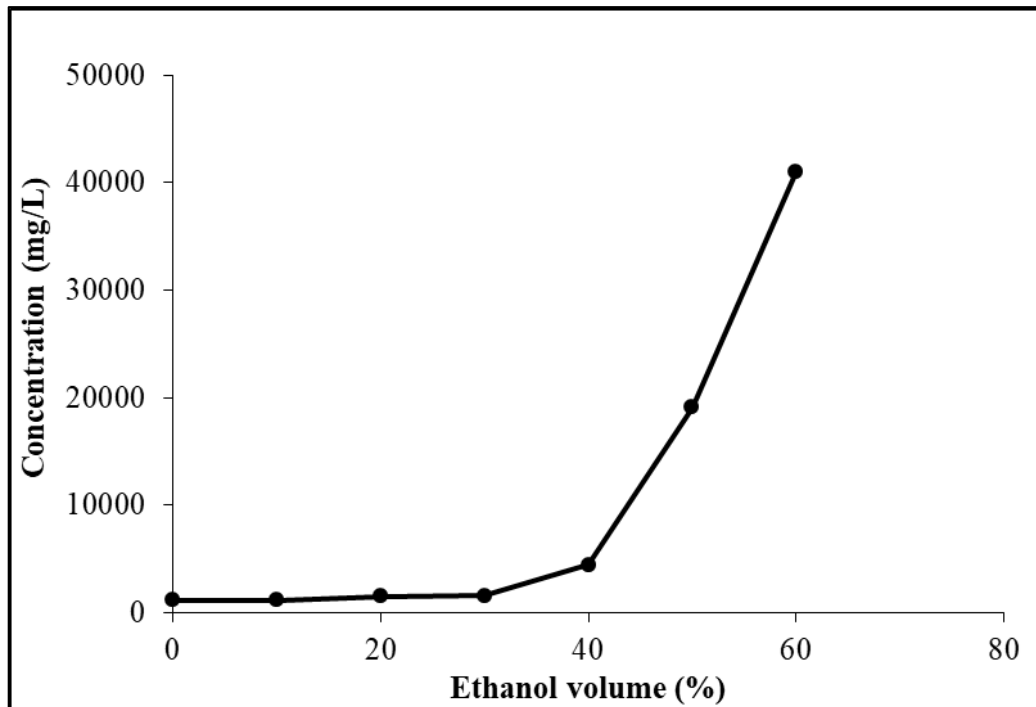


Figure 5.4. Solubility of TCE in ethanol-water system as a function of volume fraction of ethanol in the aqueous phase.

### 5.2.3. Miscibility Measurements

Figure 5.5 shows the miscibility curve of TCE and water in the presence of ethanol. The ternary phase diagram is plotted on the basis of mass percentage fractions of the components. The graph gives the miscibility of the TCE-water system for different cosolvent contents. Specifically, for the compositions above the ternary phase, the system is fully miscible, and only one phase is present. For compositions below the miscibility curve, two phases would be present which are the aqueous phase and NAPL-rich phase. The multiphase system is fully miscible at ethanol contents higher than 50%.

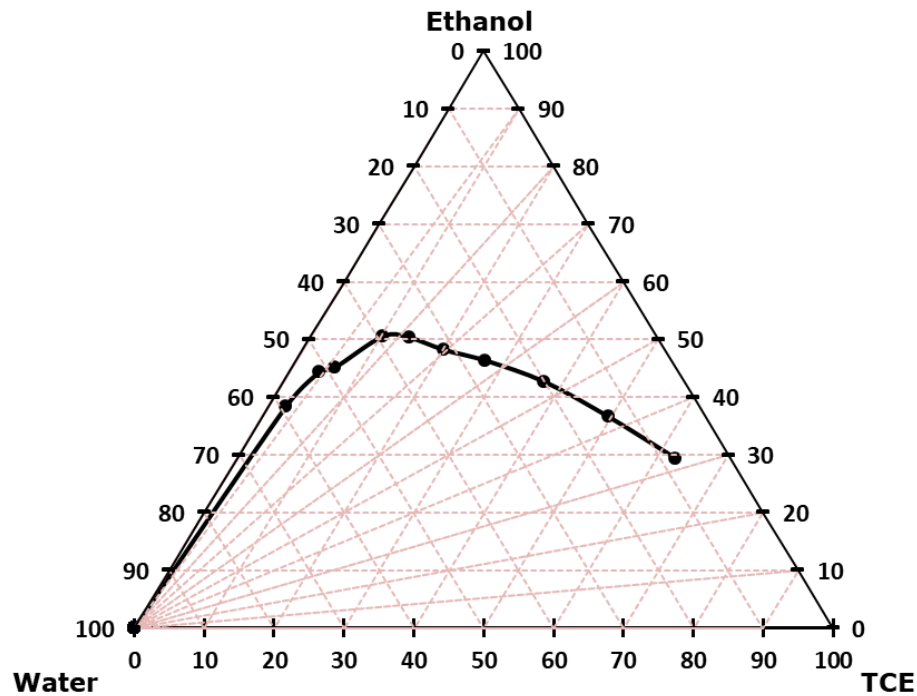


Figure 5.5. Ternary phase diagrams for TCE-ethanol-water (mass %).

### 5.3. Intermediate-scale Flushing Experiments

The results of the intermediate-scale flushing experiments are presented in this section. Before the cosolvent flushing experiments, tracer tests were conducted to investigate the transport characteristics of the tank system. After the tracer test, 6 flushing experiments for various flow conditions were conducted as indicated in Table 4.1.

#### 5.3.1. Tracer Tests

The breakthrough curves and best fit analytical solutions for the low (1 m/d) and high (3.2 m/d) velocity intermediate-scale experiments are presented in Figure 5.6 a and b, respectively.

The shape of the breakthrough curves was very close to the theoretical curves suggesting that the compaction of the tank was fairly uniform with no preferential flow paths. The porosity of the sand determined from these tracer tests was 0.36. The dispersion coefficients for the high and low velocity tracer experiments were estimated as  $0.3 \times 10^{-6} \text{ m}^2/\text{s}$  (NRMSE = 0.023) and  $0.2 \times 10^{-6} \text{ m}^2/\text{s}$  (NRMSE = 0.056), respectively. The corresponding average dispersivity is 0.015 m. The dispersivity value was used in the numerical model.

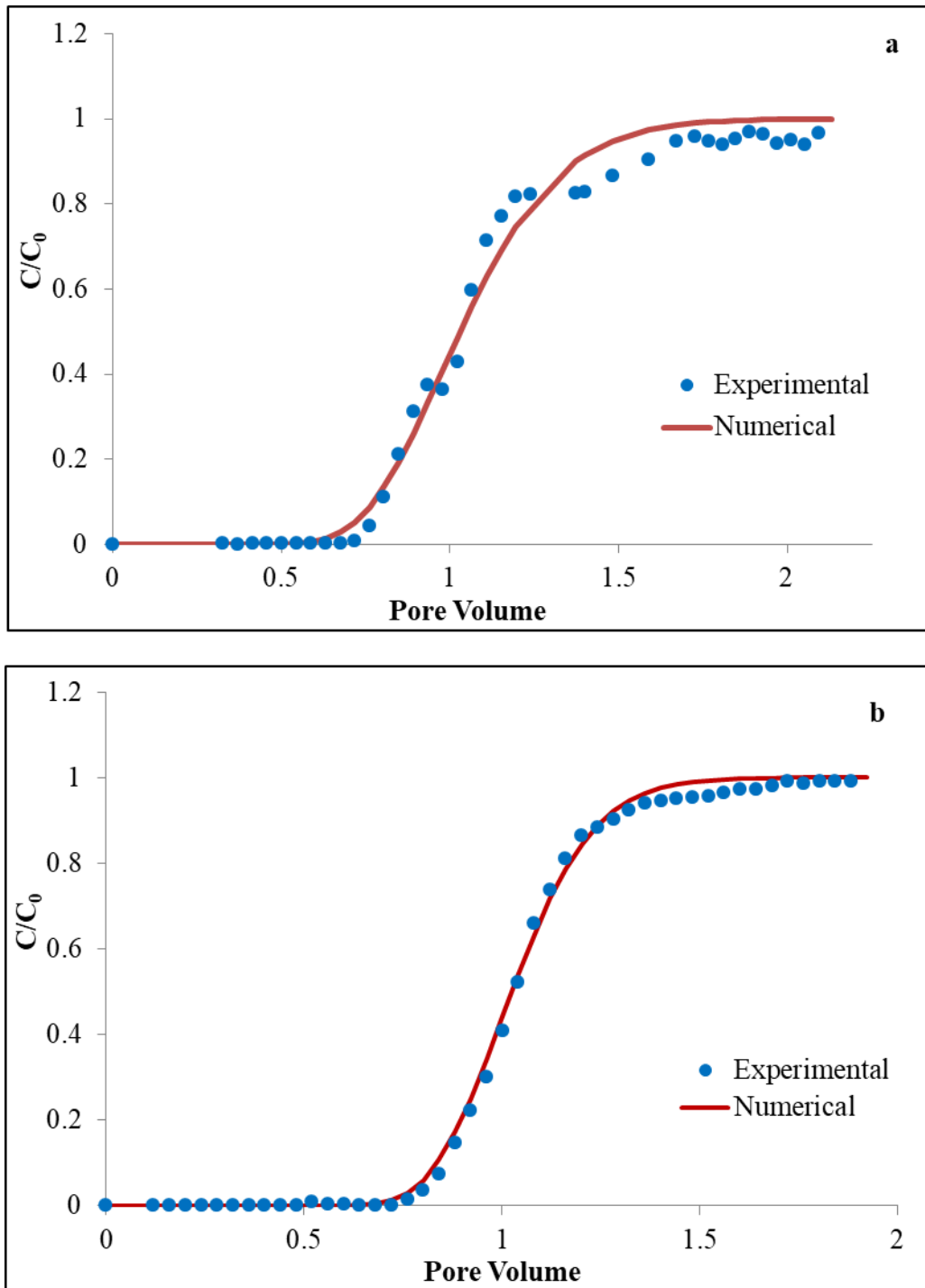


Figure 5.6. Tracer test experimental data and best fit solutions a) low flow (1 m/d) and b) high flow (3.2 m/d).

The images in Figure 5.7 show the movement of the dyed tracer in the tank at high velocity. The movement of the dyed tracer shows that there is vertical mixing in the tank. It has been observed that the flow was higher in the upper part of the tank since the compaction is low in this section. As a result, providing the equal compaction along the vertical side of the tank is not possible with the used sand even if it is homogeneous.

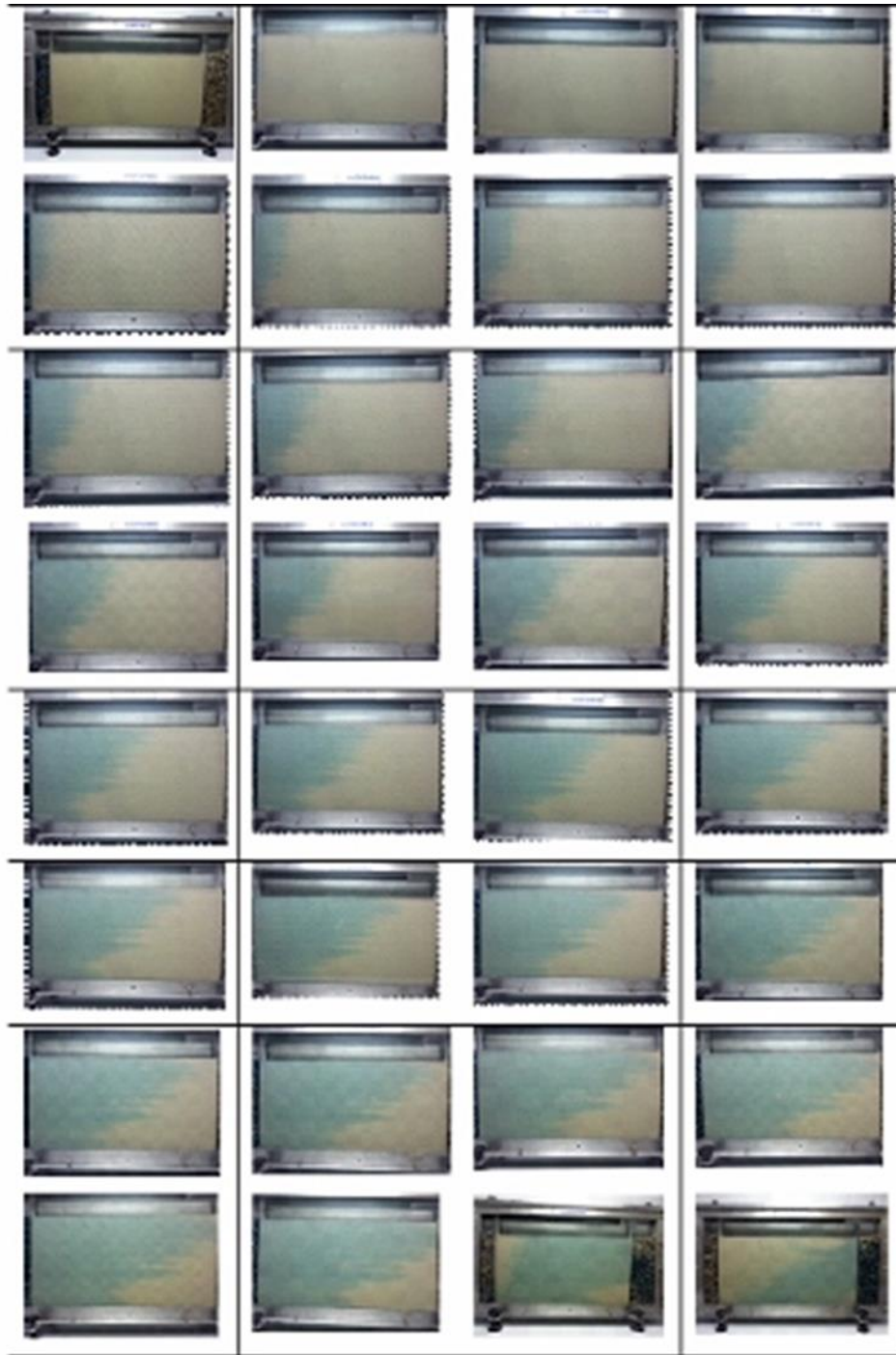


Figure 5.7. The photos of the dyed tracer test.

### 5.3.2. Cosolvent Flushing Experiments

The cumulative TCE mass removal as a function of pore volume for each flushing experiment is presented in Figure 5.8.

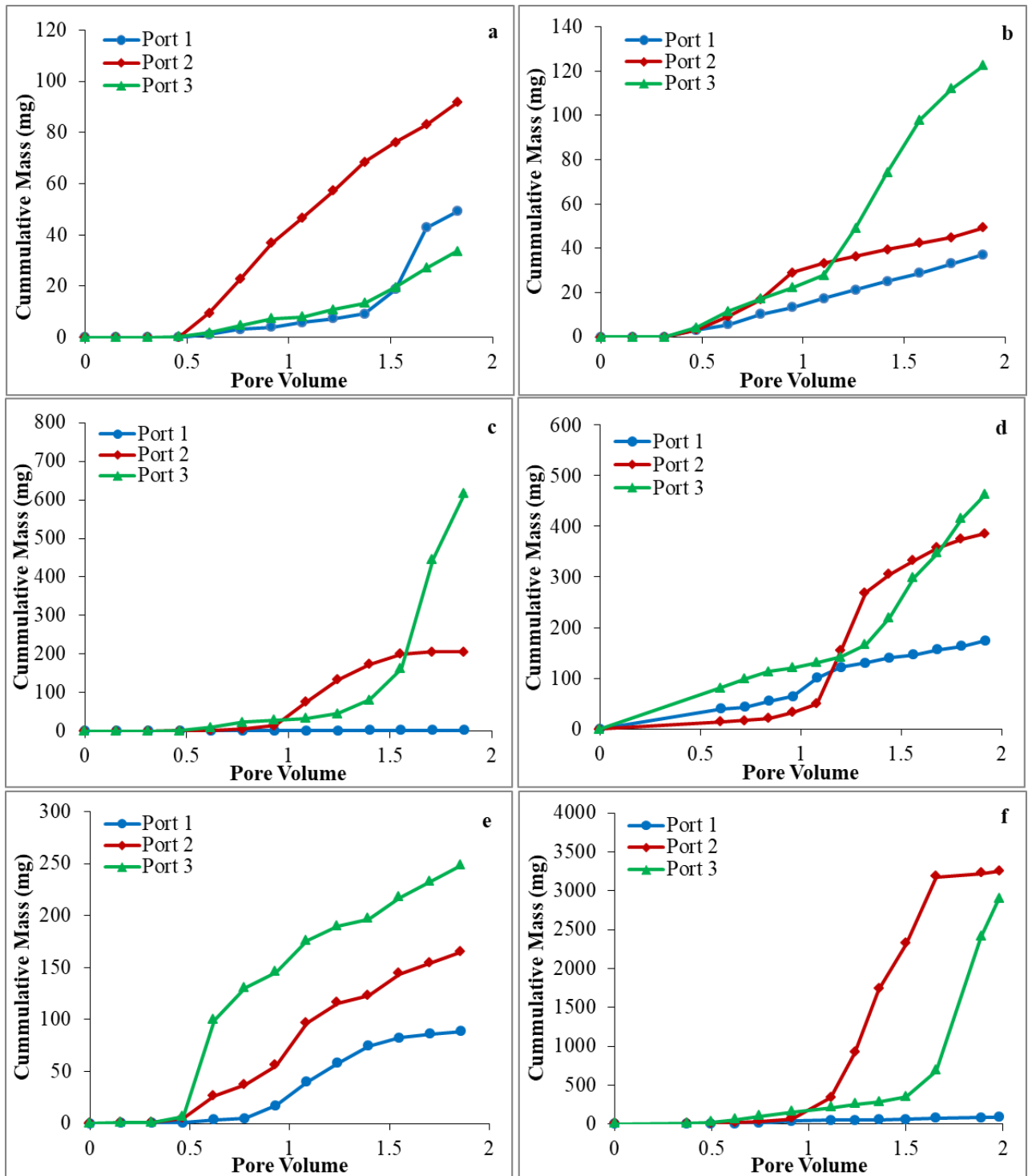


Figure 5.8. Cumulative TCE mass in the effluent a) Exp 1: high velocity, continuous flow, 0% ethanol content, b) Exp 2: high velocity, continuous flow, 20% ethanol content, c) Exp 3: high velocity, continuous flow, 50% ethanol content, d) Exp 4: intermediate velocity, continuous flow, 50% ethanol content, e) Exp 5: high velocity, intermittent flow, 20% ethanol content, f) Exp 6: low velocity, continuous flow, 50% ethanol content.

The collected mass from upper ports was higher for the 0 and 20% ethanol flushing solutions while the highest TCE mass was collected from lower ports for the 50% ethanol solutions at high

velocity. This is attributed to density differences which may cause the movement of the TCE towards the bottom of the tank in the higher ethanol content experiments compared to the lower ethanol contents in the flushing solution.

The results of the flushing experiments show the strong dependency of the recovered TCE mass on the ethanol content and flushing velocity. Figure 5.9 shows the total TCE mass recovery (mg and %) from the flushing experiments after two pore volumes.

The cumulative mass recovered from the flushing experiment with 50% ethanol content was significantly higher when compared to 0 and 20% ethanol contents (Figure 5.9a) due to the enhanced solubility. The enhanced recovery at higher ethanol contents is consistent with the solubility and IFT data (Figure 5.3 and Figure 5.4) which show a large increase in the solubility and a decrease in the IFT at 50% ethanol content, but only a relatively small change at 20% ethanol content.

The impact of the flushing solution velocity is shown in Figure 5.9b. The TCE was partially bypassed by the flushing solution at the higher velocities, resulting in shorter contact time, and lower TCE mass recovery. Figure 5.9c shows the potential increase in recovered NAPL mass when intermittent flushing is performed. For the same flushing solution composition and velocity, intermittent injection (experiment 5) allowed for greater contact time between the flushing solution and the NAPL compared to the continuous injection case (experiment 2), leading to significantly higher effluent TCE concentrations (Figure 5.8) and enhanced TCE mass recovery (Figure 5.9c).

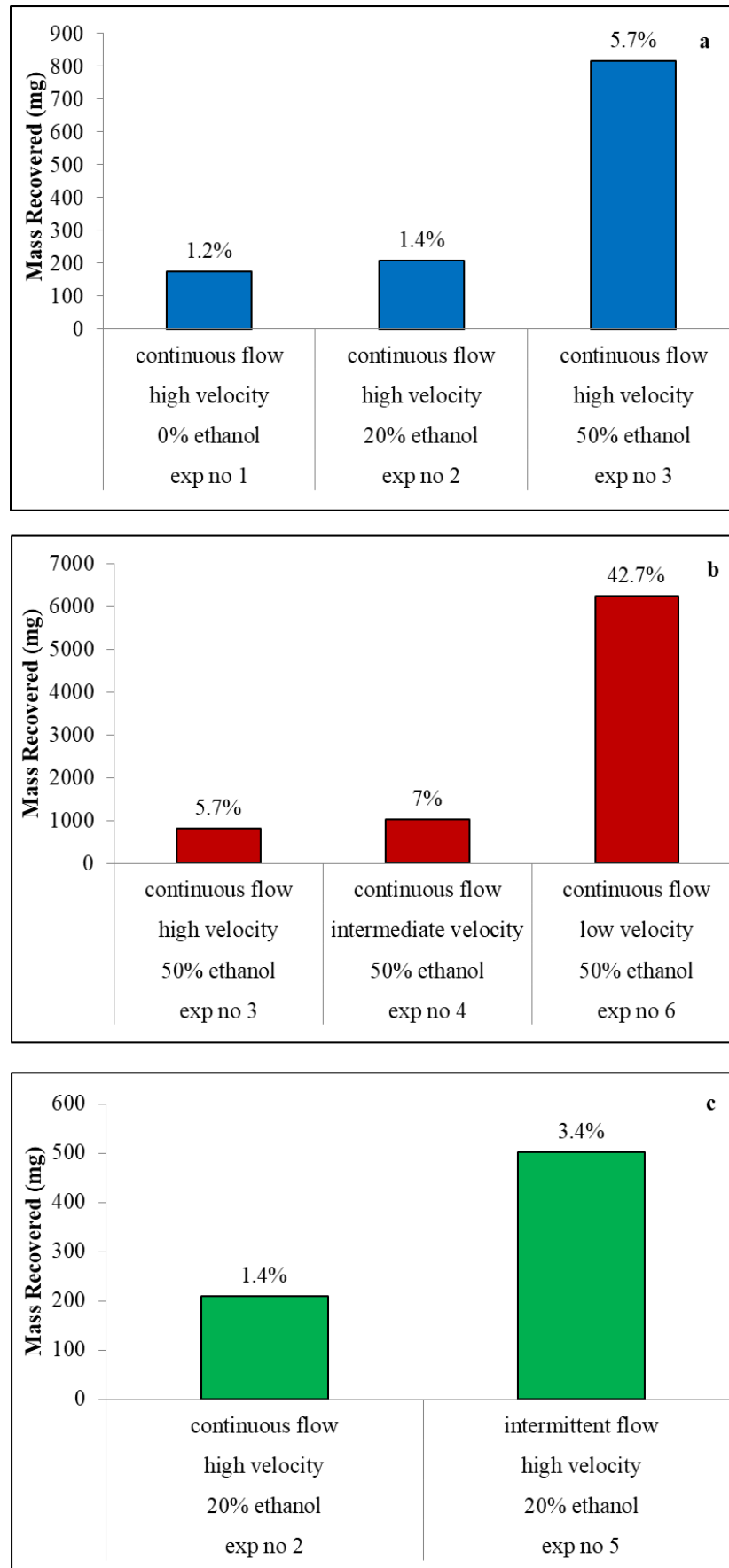


Figure 5.9. Effect of different flow conditions on TCE mass recovery (mg and %). a) The effect of ethanol, b) The effect of velocity, c) The effect of pumping pattern.

To gain further insight into the conducted flushing experiments, the capillary, bond, and trapping numbers were calculated. These non-dimensional parameters can be used to assess the potential of NAPL mobility (Pennell et al. 1996):

$$N_{Ca} = \frac{q_w \mu_w}{\sigma_{ow} \cos \theta} \quad (5.1)$$

where,

$N_{Ca}$ : the capillary number [-]

$q_w$ : the Darcy velocity of the aqueous phase [L/T]

$\mu_w$ : the is the dynamic viscosity of the aqueous phase [M/L-T]

$\sigma_{ow}$ : the interfacial tension between the organic liquid and water [M/T<sup>2</sup>]

$\theta$ : the contact angle between water and the organic liquid [-]

$$N_B = \frac{\Delta \rho g k k_{rw}}{\sigma_{ow} \cos \theta} \quad (5.2)$$

where,

$N_B$ : the bond number [-]

$\Delta \rho$ : the density difference between water and organic liquid phase [M/L<sup>3</sup>]

$g$ : the gravity [L/T<sup>2</sup>]

$k$ : the intrinsic permeability of the porous medium [L<sup>2</sup>]

$k_{rw}$ : the relative permeability to the aqueous phase [-]

$$N_T = \sqrt{N_{Ca}^2 + N_B^2} \quad (5.3)$$

where,

$N_T$ : the trapping number for horizontal flow [-].

It is reported in the literature that NAPL mobility is initiated at trapping numbers of  $2-5 \times 10^{-5}$  and complete displacement of the NAPL is observed as trapping number approaches to  $1 \times 10^{-3}$  (Pennell et al. 1996). For the case of 50% ethanol and high velocity, which is the most likely experiment to produce NAPL mobility, the trapping number was calculated to be  $0.4 \times 10^{-5}$ . This value was based on a contact angle of  $30^\circ$ , absolute viscosity of  $0.001 \text{ N-s/m}^2$ , and IFT of  $4 \text{ mN/m}$

(Figure 5.3). These results suggest that NAPL mobility did not occur in the experiments and that the resultant increase in NAPL recovery is due to enhanced solubility.

## 5.4. Modelling

In this part of the chapter, the results of the multiphase flow model, described in Section 4.3., is applied to the intermediate-scale experiments. The model was first calibrated and then used to simulate the ethanol flushing experiments. The model results expressed in terms of effluent TCE concentration and the best-fit interphase mass transfer coefficient for all experiments are presented.

### 5.4.1. Calibration of the Model

The flow calibration of the model was performed by slightly adjusting the permeability values based on the first flushing experiment (0% ethanol). The permeability was adjusted so that the imposed pressure difference in the tank would produce the observed velocities. The estimated permeability value that was obtained by the calibration process was 16.7 Darcy for the sand and 50 Darcy for the gravel. These values were also used as constant for the rest of the experiments.

For the TCE flushing calibration, the average concentration of all three ports was used as a calibration target. This corresponds to the concentration that would be measured in a well in the field. The model was tested under local equilibrium dissolution conditions and non-equilibrium mass transfer but the observed TCE concentrations were overestimated for all experiments. For this reason, non-equilibrium conditions were adopted. The mass transport model calibration was performed by adjusting the lumped mass transfer coefficient in order to reproduce the experimental results as closely as possible. The dispersivity values were obtained from tracer experiments. The list of input key parameters that were used for the model development is presented in Table 5.1.

Table 5.1. List of key parameters used in the model simulations.

		<b>From</b>
<b>Porosity</b>	0.36	Tracer test
<b>Intrinsic permeability</b>	16.7 Darcy (sand), 50 Darcy (gravel)	Calibration
<b>Longitudinal dispersivity</b>	5 cm <sup>a</sup>	Tracer test
<b>Transverse dispersivity</b>	0.8 cm <sup>a</sup>	Calibration
<b>Hand's parameters for TCE</b>	C <sub>3max</sub> =0.34 (v/v) <sup>b</sup>	TPD experiments
<b>Interfacial tension for TCE</b>	k <sub>Li&amp;Fu</sub> = 2 <sup>c</sup> , X <sub>0</sub> = -3.09	Li and Fu, 1992
<b>Capillary pressure parameters</b>	λ = 2 <sup>d</sup> , P <sub>bl</sub> = 5.032 kPa	Corey, 1994
<b>Residual saturations (low capillary number)</b>	S <sub>r</sub> = 0.2 <sup>e</sup> for all phases	Shah et al., 1995
<b>Residual saturations (high capillary number)</b>	S <sub>r</sub> = 0.05 <sup>e</sup> for all phases	Shah et al., 1995

#### 5.4.2. Modelling Results

The simulated and observed effluent TCE concentrations are presented in Figure 5.10 as a function of pore volume for an initial NAPL zone of 5x5 cm. For comparison between experimental and simulation results, the computed root mean square error (RMSE) and normalized error (NRMSE) values have been summarized in Table 5.2 along with the best-fit mass transfer coefficients,  $K_l$ , used in the model.

Table 5.2. Comparative measures (RMSE and NRMSE) and lumped mass transfer coefficients for different DNAPL injection zone sizes of 5x5 cm and 3x3 cm.

<b>Experiment</b>	<b>Mass transfer coefficient (1/d)</b>		<b>RMSE (ppm)</b>		<b>NRMSE</b>	
	<b>5x5 cm</b>	<b>3x3 cm</b>	<b>5x5 cm</b>	<b>3x3 cm</b>	<b>5x5 cm</b>	<b>3x3 cm</b>
1	3.2	3.3	5.396	5.175	0.130	0.125
2	3.4	3.4	8.349	8.557	0.157	0.161
3	1.3	1.2	78.165	75.351	0.204	0.196
4	0.5	0.5	38.496	37.624	0.158	0.155
5	4.8	4.2	25.519	26.827	0.296	0.312
6	2.2	1.9	402.849	457.724	0.214	0.244

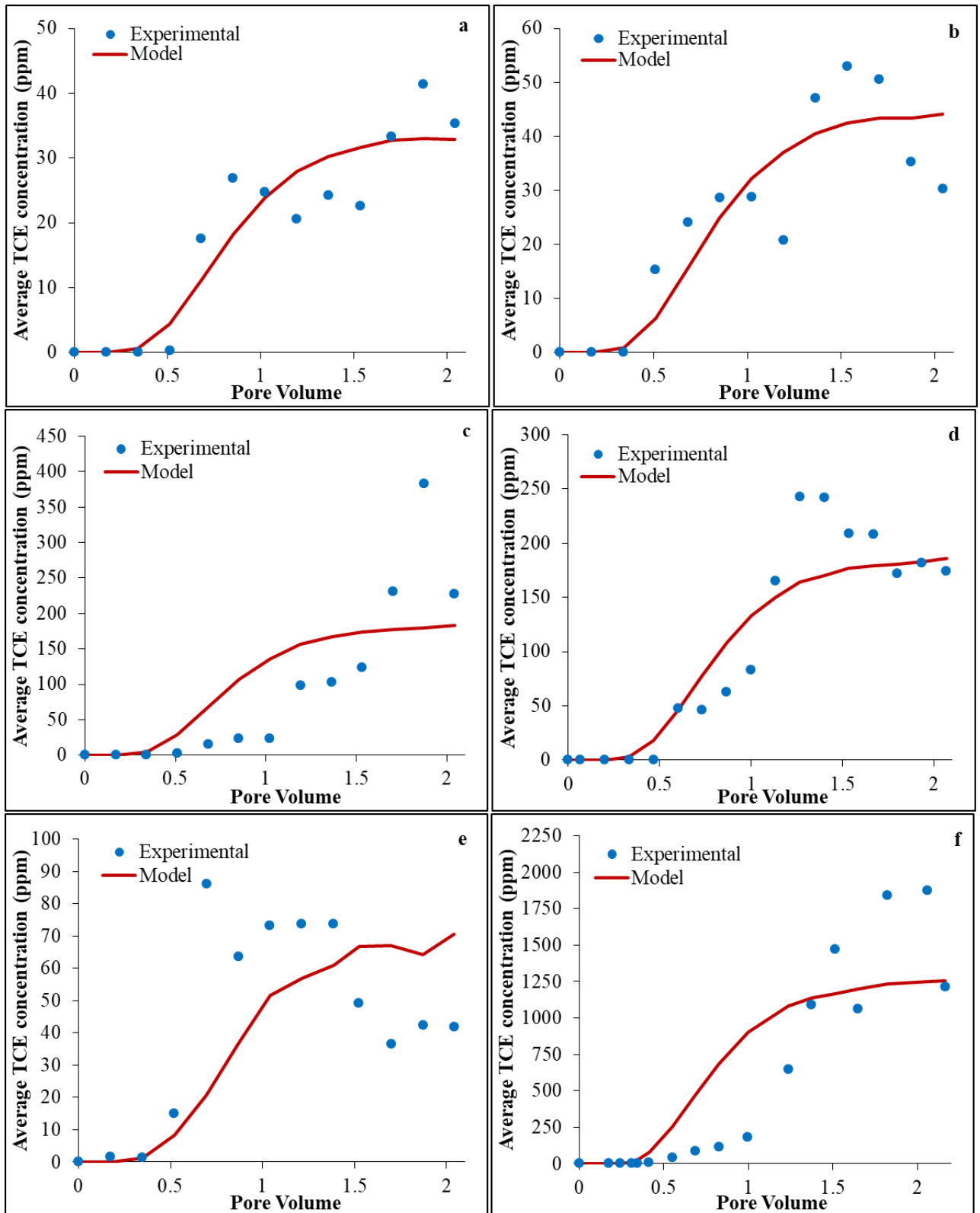


Figure 5.10. Modeling results for DNAPL injection zone size of 5x5 cm, a) Exp 1: high velocity, continuous flow, 0% ethanol content, b) Exp 2: high velocity, continuous flow, 20% ethanol content, c) Exp 3: high velocity, continuous flow, 50% ethanol content, d) Exp 4: intermediate velocity, continuous flow, 50% ethanol content, e) Exp 5: high velocity, intermittent flow, 20% ethanol content, f) Exp 6: low velocity, continuous flow, 50% ethanol content.

For the NRMSE, the difference between the observed and simulated concentrations was normalized by maximum observed concentration of each experiment. Hence, the NRMSE reports the error in the form of a fraction of the observed concentrations.

The modeling results are considered acceptable in all cases as the NRMSE is relatively low (0.125-0.312). In general, the enhanced solubilization of TCE with the introduction of ethanol in the flushing solution is evident, leading to higher concentrations. For some of the experiments, the measured TCE concentration rises up to a point and then starts to fall, a trend that cannot be captured by the model using a single mass transfer coefficient. This phenomenon could be attributed to the bypassing of the NAPL source by the flushing solution. The blocking of some pores by the NAPL causes the flow to divert away the NAPL mass, resulting in a significant decrease in NAPL recovery compared to what is predicted by multiphase models. This phenomenon was found to be more pronounced for high velocities and concurs with the findings of other researchers (e.g., Keely and Boulding 1989; Hoffman 1993; Brusseau et al. 2002; Brooks et al. 2004; Agaoglu et al. 2012).

Figure 5.11 compares the simulated and observed effluent TCE concentrations for the case of a 3x3 cm initial DNAPL zone. The corresponding best-fit  $K_1$  values for this case are presented in Table 5.2. It is interesting to note that the effluent concentrations and best-fit  $K_1$  values are almost identical. This was a result of DNAPL redistribution of 3x3 cm and 5x5 cm DNAPL zones to similar areas. Although the initial DNAPL saturation is often cited as a major source of uncertainty in many problems, the current simulations suggest that in some instances defining the correct DNAPL spill volume may be sufficient for accurately simulating the contamination transport problem. It is important to note however that at some sites, an accurate estimate of the NAPL spill may not be available.

Figure 5.12 compares the cumulative recovered mass calculated with experimental data and model for each flushing experiment. The results show that experimental calculations match well with the model estimations with an average absolute error of 11%. This suggests that modelling results are considered acceptable for all experiments.

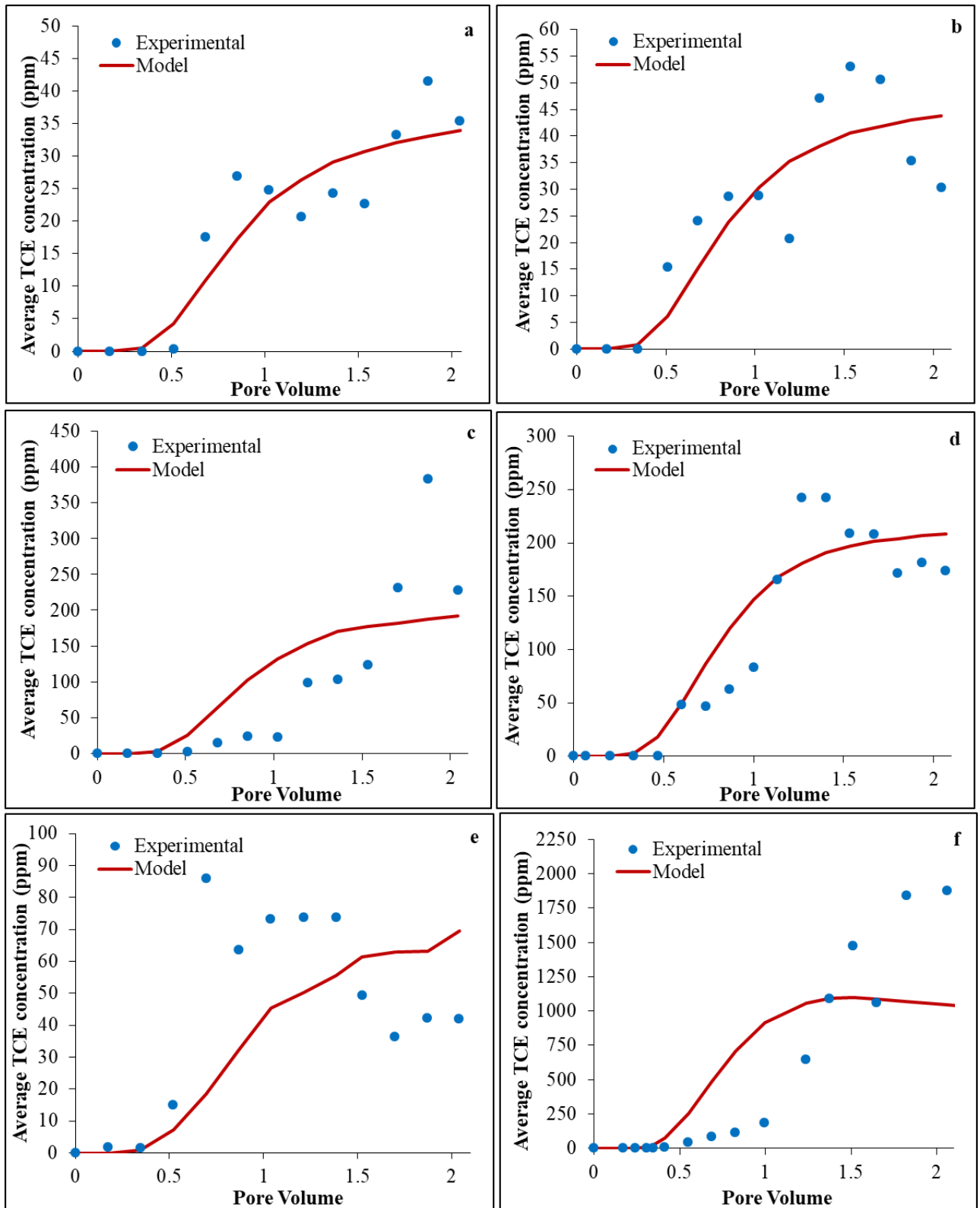


Figure 5.11. Modeling results for DNAPL injection zone size of 3x3 cm, a) Exp 1: high velocity, continuous flow, 0% ethanol content, b) Exp 2: high velocity, continuous flow, 20% ethanol content, c) Exp 3: high velocity, continuous flow, 50% ethanol content, d) Exp 4: intermediate velocity, continuous flow, 50% ethanol content, e) Exp 5: high velocity, intermittent flow, 20% ethanol content, f) Exp 6: low velocity, continuous flow, 50% ethanol content.

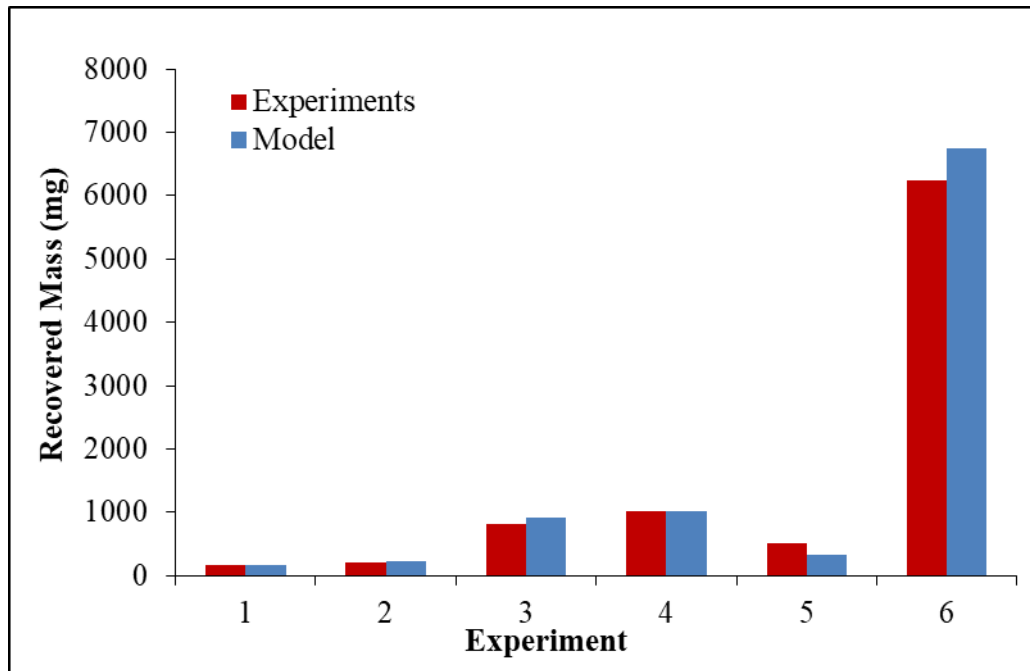


Figure 5.12. Recovered TCE mass calculated from experiments and with model.

Figure 5.13 presents a plot of the modified Sherwood numbers as a function of the Reynolds number calculated for the best-fit mass transfer coefficients using Equation 2.4. For comparison, the modified Sherwood correlations developed by Saba and Illangasekare (2000) and Nambi and Powers (2003) Equations 2.5 and 2.6 are also plotted on the graph. The Reynolds numbers were calculated using the Equation 2.7. The grain size diameter was taken as  $d_m = 0.0002$  m and kinematic viscosity of the flushing solution was determined for each experiment and these values with velocity were used to calculate Reynolds number. Because the characteristic length is taken as the grain diameter in porous media, the computed Re number is small in the range of 0.0006 to 0.004. The modified Sherwood numbers were calculated using the Equation 2.4. The grain size diameter was taken as  $d_m = 0.0002$  m and molecular diffusion coefficient was taken as  $D_m = 0.2 \times 10^{-8}$  m<sup>2</sup>/s which is determined from tracers tests. The calculated modified Sherwood numbers from the experimental data were found to be about 10 to 200 times lower than the modified Sherwood numbers from the literature for the same Reynolds numbers. Similar observations have been noted in the literature, particularly when Sherwood correlations developed from lab-scale experiments are applied in the field (Maji and Sudicky 2008; Kokkinaki et al. 2013b). These discrepancies are a result of pore scale variations in the NAPL distributions which tend to be uniform in the lab-scale experiments but are much complex in the field. Whereas the Sherwood correlations are generally developed for pooled or ganglia NAPL, the initial NAPL distribution in this intermediate-scale study were larger than residual saturation. This is closer to a real spill that is likely to consist of both NAPL configurations.

Figure 5.13 also suggests that the modified Sherwood number may decrease with increase in ethanol content. Specifically, the experiments with 50% ethanol contents yield Sherwood numbers (or interphase mass transfer coefficients) that are on average about three to four times lower than the experiments with 0 and 20% ethanol contents. As most mass transfer studies have focused on the dissolution of NAPLs into pure water, fluid properties such as density or viscosity are not explicitly accounted for in the developed Sherwood expressions. Moreover, the interphase mass transfer is also dependent on the lateral diffusion coefficient and its ability to transport the dissolved NAPL away from the interface to facilitate further dissolution. The diffusion coefficient is also a function of the flushing solution composition. As such, flushing solution properties are lumped into the interphase mass transfer coefficient. This suggests that published correlations may not accurately estimate the interphase mass transfer rate in the presence of cosolvents. This can have a significant impact on modeling studies involving the use of cosolvent for enhanced NAPL dissolution. Further detailed experiments would be needed to assess and quantify the factors influencing interphase mass transfer rate when cosolvents are present.

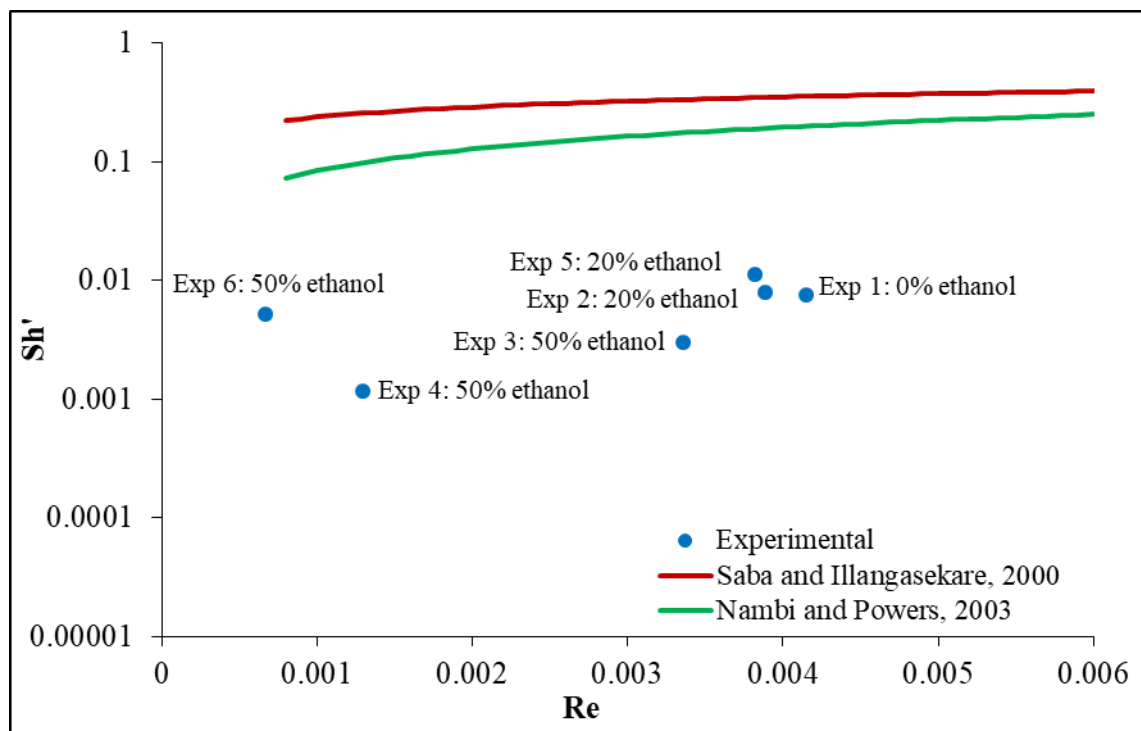


Figure 5.13. Modified Sherwood number versus Reynolds number for all experiments, Exp 1: high velocity, continuous flow, Exp 2: high velocity, continuous flow, Exp 3: high velocity, continuous flow, Exp 4: intermediate velocity, continuous flow, Exp 5: high velocity, intermittent flow, Exp 6: low velocity, continuous flow, 50% ethanol content.

## 6. INTERPHASE MASS TRANSFER FROM POOLED DNAPL AND DETERMINATION OF THE SHERWOOD CORRELATION \*

In this part, controlled dissolution experiments were conducted to investigate the factors influencing the interphase mass transfer from pooled DNAPL. As reported in the Introduction section, NAPL in the form of DNAPLs are often encountered in the field. However, hard data quantifying the interphase mass transfer are limited in the field. Section 6.1 gives the calibration curve used in the determination of the DCB concentrations. Section 6.2 presents the results of the NAPL dissolution experiments. Section 6.3 discusses the numerical model that was developed to simulate the dissolution experiments. Section 6.4 presents the newly derived Sherwood number correlations.

### 6.1. Calibration Curve of DCB

The DCB effluent samples from the dissolution experiments were analyzed using a UV-vis spectrophotometer at a wavelength of 220 nm. The concentration range of the calibration curve was 1-25 mg/L. The calibration curve obtained with this wavelength was very close to linearity with a correlation coefficient  $R^2$  exceeding 0.99 (Figure 6.1).

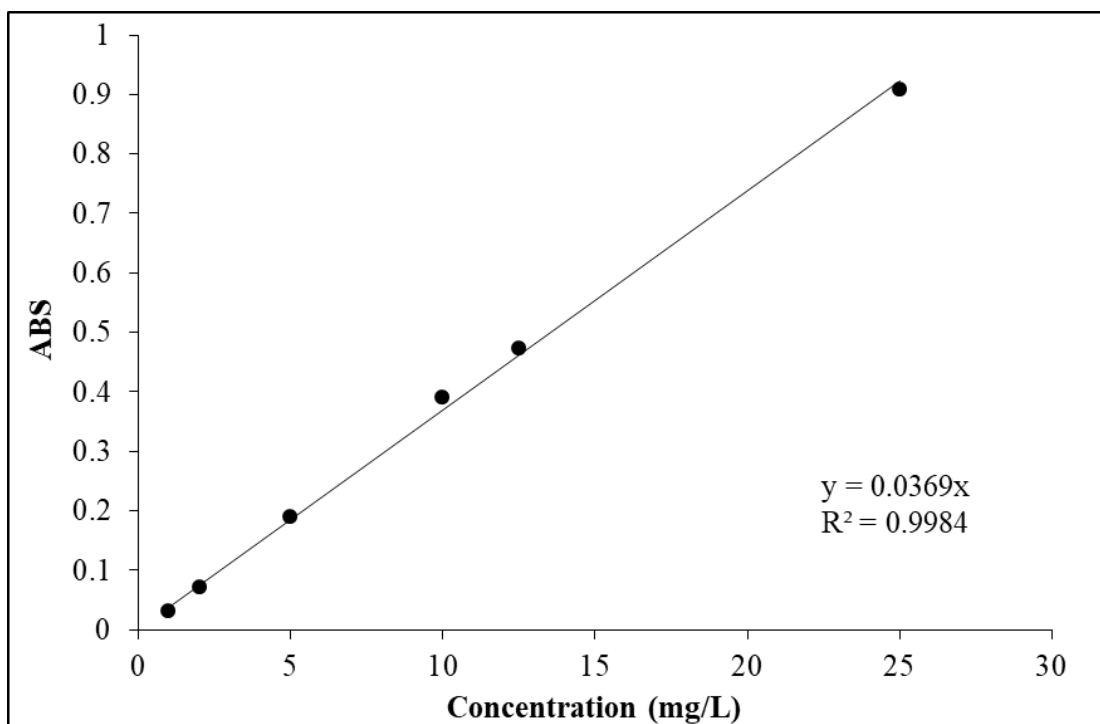


Figure 6.1. DCB calibration curve for UV-vis Spectrophotometer.

\* The results presented in this chapter were published in Sarikurt et al., 2017

## 6.2. Flow Cell Experiments

### 6.2.1. Tracer Tests

As in the intermediate-scale experiments, tracer experiments were first conducted in the flow cell to identify the dispersion coefficient and dispersivity. These two parameters are dependent on the specific experiments- the flow, existing flow regime, the porous media used, and the scale of the problem- therefore they need to be performed with each experiment.

The breakthrough curves and best-fit numerical solutions for the glass beads and sand tracer experiments are shown in Figure 6.2. The analytical solutions were essentially identical to the numerical solution. The shape of the experimental breakthrough curves shown in Figure 6.2 is very close to the theoretical curves suggesting that the compaction of the tank was uniform with no preferential flow paths.

The porosity of the glass beads and sand determined from these tracer tests were 0.34 and 0.36, respectively. The values were determined by minimizing the root mean square error (RMSE) of the experimental and simulation data. The corresponding coefficient of determination,  $R^2$  was greater than 0.995 for all tracer test experiments indicating good agreement between experimental data and model. The best-fit longitudinal dispersion coefficients and the corresponding dispersivity values are given in Table 6.1. The average dispersivity value of 0.002 m was used in the pore network model for the estimation of the interphase mass transfer coefficient. The setup of the flow cell does not allow for the direct estimation of the lateral dispersivity. Given that the porous media used in this study are quite uniform in size and shape and that the vertical dimension of the flow domain (0.03 cm) is relatively small, it was assumed that the vertical dispersivity was equal to 0.002 m.

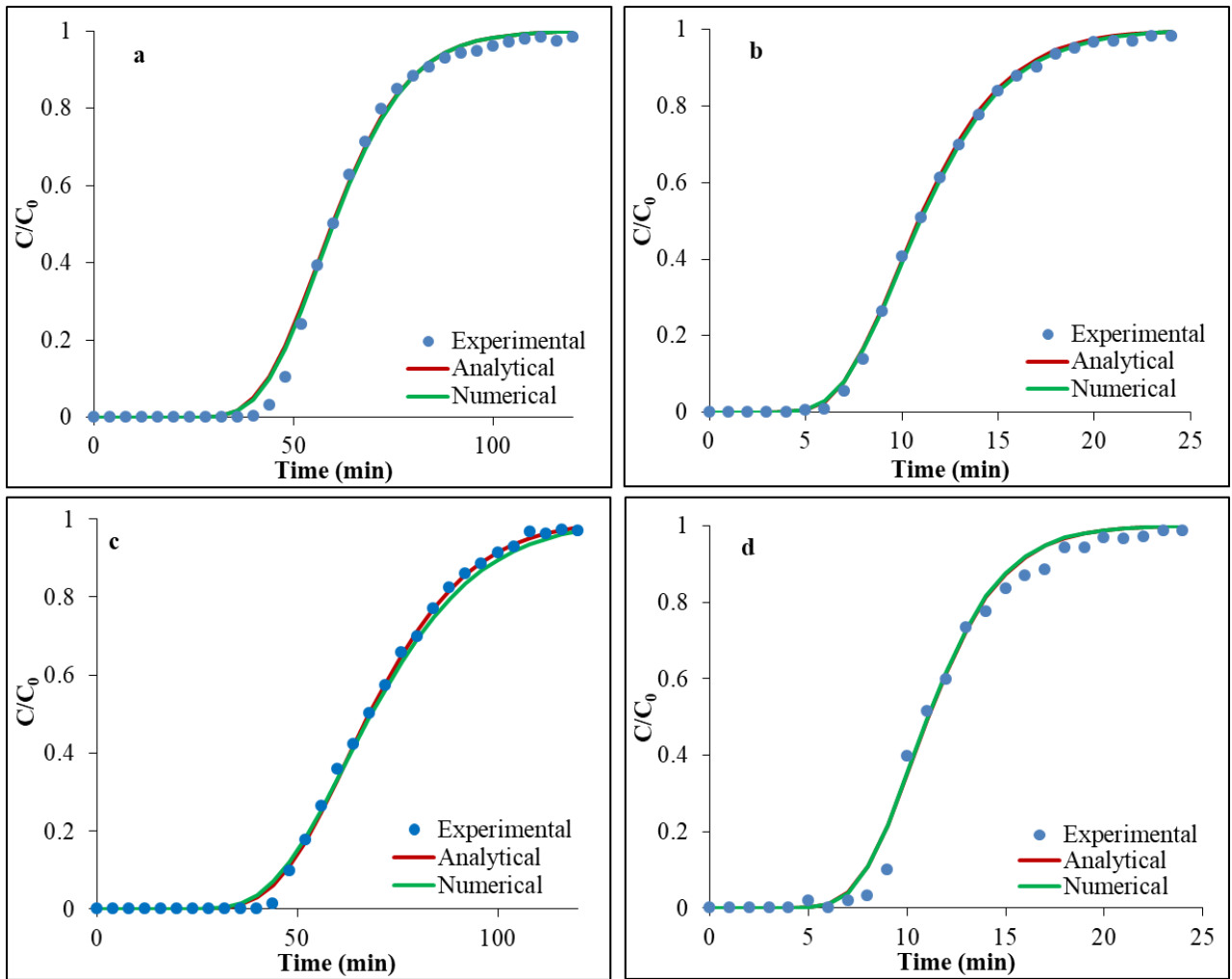


Figure 6.2. Tracer test experimental data and best-fit solutions a) glass beads, low flow ( $v = 2.8 \times 10^{-5}$  m/s), b) glass beads, high flow ( $v = 1.5 \times 10^{-4}$  m/s), c) sand, low flow ( $v = 2.4 \times 10^{-5}$  m/s), and d) sand, high flow ( $v = 1.5 \times 10^{-4}$  m/s).

Table 6.1. Dispersion coefficient and dispersivity values determined from tracer tests.

	Glass beads		Sand	
Flow rate	High	Low	High	Low
Velocity (m/s)	$1.5 \times 10^{-4}$	$2.8 \times 10^{-5}$	$1.5 \times 10^{-4}$	$2.4 \times 10^{-5}$
Dispersion coefficient ( $\text{m}^2/\text{s}$ )	$7.7 \times 10^{-7}$	$0.86 \times 10^{-7}$	$5.3 \times 10^{-7}$	$1.0 \times 10^{-7}$
Longitudinal dispersivity (m)	0.002	0.001	0.002	0.0015
Peclet number ( $\text{Pe} = v d_m / D_m$ )	153	28	30	5

### 6.2.2. Dissolution Experiments

The velocity and the average effluent concentrations with standard errors are presented for the dissolution experiments with glass beads and sand in Table 6.2 and Table 6.3, respectively.

Table 6.2. Velocity and effluent concentration data from glass beads dissolution experiments.

<b>Experiment</b>	<b>Velocity (m/s)</b>	<b>Average effluent concentration (mg/L)</b>	<b>Standard error (%)</b>	<b>Peclet number</b>
1	$8.7 \times 10^{-6}$	100.8	1.2	8.7
2	$1.3 \times 10^{-5}$	96.5	1.3	13.2
3	$3.6 \times 10^{-5}$	84.2	1.7	36.1
4	$7.9 \times 10^{-5}$	71.4	0.9	79.1
5	$1.6 \times 10^{-4}$	65.3	1.4	163.4
6	$3.3 \times 10^{-4}$	54.0	1.2	334.2
7	$5.1 \times 10^{-4}$	47.7	0.3	515.9
8	$1.0 \times 10^{-3}$	43.6	1.0	980.4

Table 6.3. Velocity and effluent concentration data from sand dissolution experiments.

<b>Experiment</b>	<b>Velocity (m/s)</b>	<b>Average effluent concentration (mg/L)</b>	<b>Standard error (%)</b>	<b>Peclet number</b>
1	$6.4 \times 10^{-6}$	81.8	1.1	1.3
2	$8.1 \times 10^{-6}$	76.1	1.2	1.6
3	$1.1 \times 10^{-5}$	75.7	1.2	2.3
4	$1.9 \times 10^{-5}$	86.7	1.1	3.9
5	$4.0 \times 10^{-5}$	63.5	1.2	8.1
6	$7.7 \times 10^{-5}$	70.7	0.6	15.4
7	$1.5 \times 10^{-4}$	60.9	0.6	30.2
8	$2.9 \times 10^{-4}$	52.0	0.9	59.8
9	$4.9 \times 10^{-4}$	49.3	0.6	99.5
10	$9.2 \times 10^{-4}$	39.3	1.2	185.2
11	$1.1 \times 10^{-3}$	38.5	1.1	216.0

The Peclet numbers were calculated using Equation 4.10. The grain size diameter was taken as  $d_m=0.001$  m for glass beads and  $d_m=0.0002$  m for sand. The molecular diffusion coefficient was  $D_m=1 \times 10^{-9}$  m<sup>2</sup>/s. The velocity of each flow cell experiment was also used to calculate Pe number.

The velocity for the glass beads experiments ranged from  $8.7 \times 10^{-6}$  to  $1.0 \times 10^{-3}$  m/s (Table 6.2) which corresponds to Peclet numbers ranging from 8.7 and 980.4. On the other hand, the velocities for the sand experiments ranged from  $6.4 \times 10^{-6}$  to  $1.1 \times 10^{-3}$  m/s (Table 6.3), which corresponds to

Peclet number between 1.3 to 216. The standard errors of the measured effluent concentrations were quite small; the maximum standard errors of the glass beads and sand experiments were 1.7 and 1.2%, respectively.

The effluent concentrations determined from the dissolution experiments as a function of velocity and for the two different porous media are presented in Figure 6.3.

Each point on Figure 6.3 corresponds to a separate dissolution experiment. Figure 6.3 shows that the effluent concentration decreases as the velocity increases due to the shorter contact time between the two phases. Moreover, the effluent concentrations from the glass beads experiments were on average about 20% higher than those observed in the sand experiments. Previous studies have also indicated that the mass transfer coefficient decreases with decrease in mean grain diameter (e.g., Powers et al., 1992; Imhoff et al., 1994; Zhang et al., 2002). With decrease in grain size, flow becomes more tortuous and the NAPL becomes less accessible to the mobile aqueous phase leading to a lower interphase mass transfer (Agaoglu, 2015).

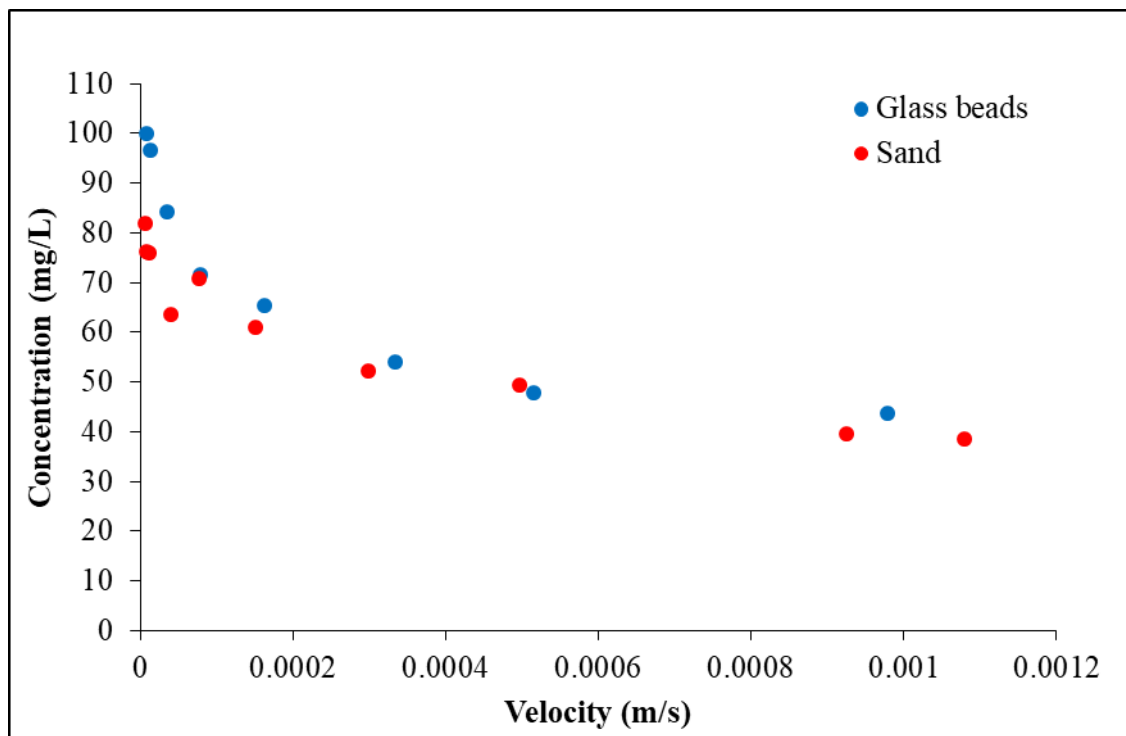


Figure 6.3. Effluent aqueous phase concentrations as a function of velocity for the glass beads and sand experiments.

The results of Figure 6.3 also show that although the cross-sectional area of the flow is small, the effluent concentrations are lower than the solubility even for the lowest velocities. This provides

further evidence for the presence of non-equilibrium conditions and the need for a rate limited kinetic dissolution expression to accurately model the interphase mass transfer.

### 6.3. Estimation of the Mass Transfer Coefficient

The mass transfer coefficients determined with the analytical equation and best-fit mass transfer coefficient determined with 2D pore network model are given in Table 6.4 and Table 6.5 for the glass beads and sand experiments, respectively. The analytical solution allows for the direct calculation of the mass transfer coefficient from the effluent solution. On the other hand, with the numerical solution (pore network model), the mass transfer coefficient is an input parameter. Hence the best-fit mass transfer coefficient is determined by trial and error such that the simulated average effluent concentration matches the observed effluent concentration from the experiments. Table 6.4 and Table 6.5 show that both sets of mass transfer coefficients increase with grain size diameter. The results also show that as the velocity increases, higher interphase mass transfer coefficients were determined due to the high concentration gradient between the two phases.

Table 6.4. Mass transfer coefficients determined with the 1D analytical equation and 2D pore network model for glass beads.

Experiment	Peclet number	Mass transfer coefficient (m/s)	
		Analytical equation	Pore network model
1	8.7	$2.7 \times 10^{-6}$	$8.8 \times 10^{-6}$
2	13.2	$3.8 \times 10^{-6}$	$1.1 \times 10^{-5}$
3	36.1	$8.4 \times 10^{-6}$	$1.9 \times 10^{-5}$
4	79.1	$1.4 \times 10^{-5}$	$2.9 \times 10^{-5}$
5	163.4	$2.7 \times 10^{-5}$	$5.1 \times 10^{-5}$
6	334.2	$4.3 \times 10^{-5}$	$7.4 \times 10^{-5}$
7	515.9	$5.6 \times 10^{-5}$	$9.4 \times 10^{-5}$
8	980.4	$9.6 \times 10^{-5}$	$1.6 \times 10^{-4}$

Table 6.5. Mass transfer coefficients determined with the 1D analytical equation and 2D pore network model for sand.

Experiment	Peclet number	Mass transfer coefficient (m/s)	
		Analytical equation	Pore network model
1	1.3	$1.4 \times 10^{-6}$	$3.7 \times 10^{-6}$
2	1.6	$1.6 \times 10^{-6}$	$3.9 \times 10^{-6}$
3	2.3	$2.3 \times 10^{-6}$	$5.3 \times 10^{-6}$
4	8.1	$6.4 \times 10^{-6}$	$1.3 \times 10^{-5}$
5	15.4	$1.4 \times 10^{-5}$	$3.2 \times 10^{-5}$
6	30.2	$2.2 \times 10^{-5}$	$4.6 \times 10^{-5}$
7	59.8	$3.6 \times 10^{-5}$	$6.7 \times 10^{-5}$
8	99.5	$5.7 \times 10^{-5}$	$1.1 \times 10^{-4}$
9	185.2	$8.1 \times 10^{-5}$	$1.4 \times 10^{-4}$
10	216.0	$9.2 \times 10^{-5}$	$1.5 \times 10^{-4}$

Figure 6.4 – Figure 6.19 show contour plots of the normalized concentration distribution in the flow cell determined from the 2D pore network model and the analytical solutions for the glass beads experiments. Each of these plots corresponds to a pair of Peclet numbers (i.e., velocity) and mass transfer coefficients presented in Table 6.4. The DCB concentrations were normalized by the DCB solubility (156 mg/L). The corresponding plots from the sand experiments are given in Figure 6.20-Figure 6.39. These figures show that the major limitation of the 1D analytical solution is that it assumes that the concentrations over the entire cross section of the flow cell are uniform. On the other hand, the 2D numerical model simulates the concentration distribution of the contaminant over the flow cell cross sectional area due to lateral dispersion. The highest concentrations obtained with the 2D pore network model are observed at the lower downgradient corner of the flow cell near the NAPL surface. Moreover, increase in velocity leads to higher concentration gradients between the interface and bulk fluid resulting in a higher mass transfer coefficient (Table 6.4 and Table 6.5). However, because higher velocities correspond to shorter contact time between the mobile aqueous phase and the NAPL, the effluent concentrations decrease with increase in velocity.

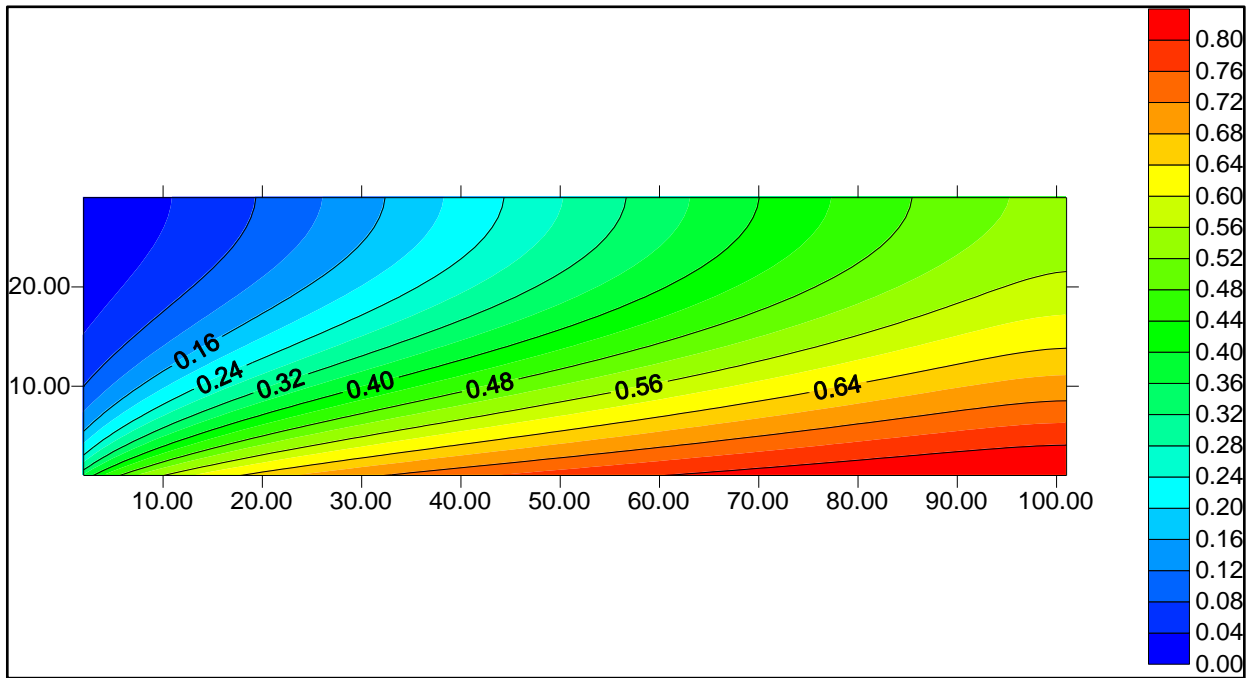


Figure 6.4. Contour plot of the normalized aqueous DCB concentration computed with the pore network model for  $Pe=8.7$  (glass beads).

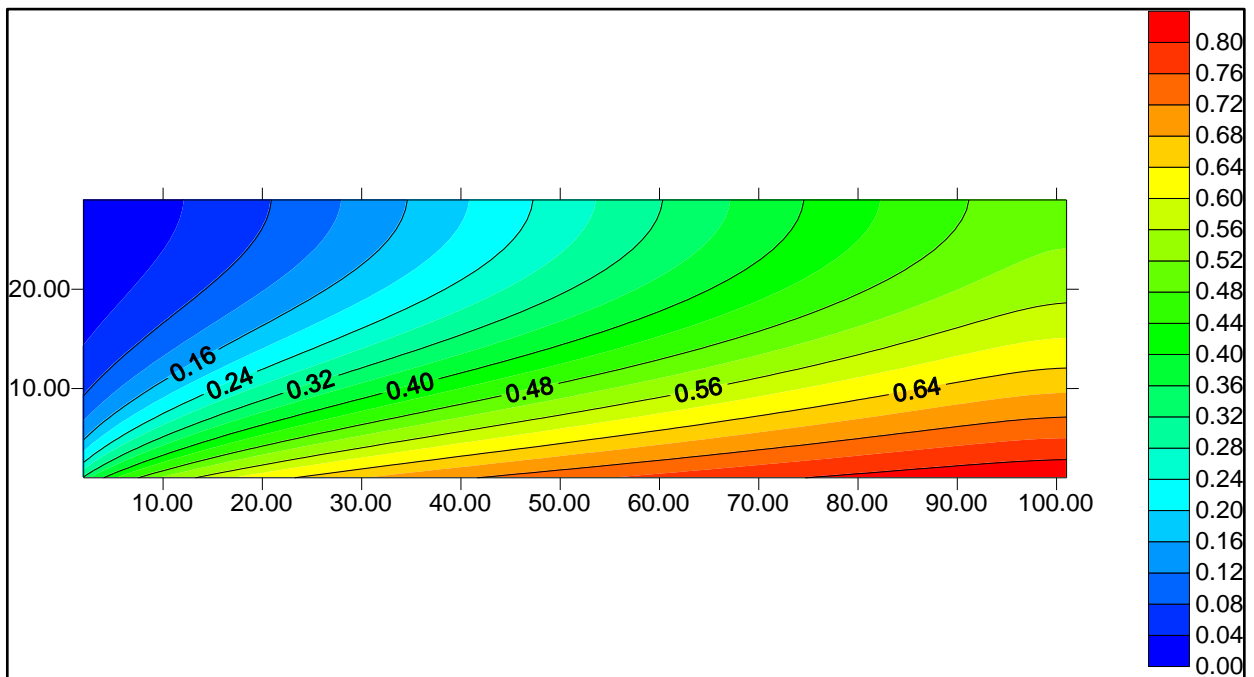


Figure 6.5. Contour plot of the normalized aqueous DCB concentration computed with the pore network model for  $Pe=13.2$  (glass beads).

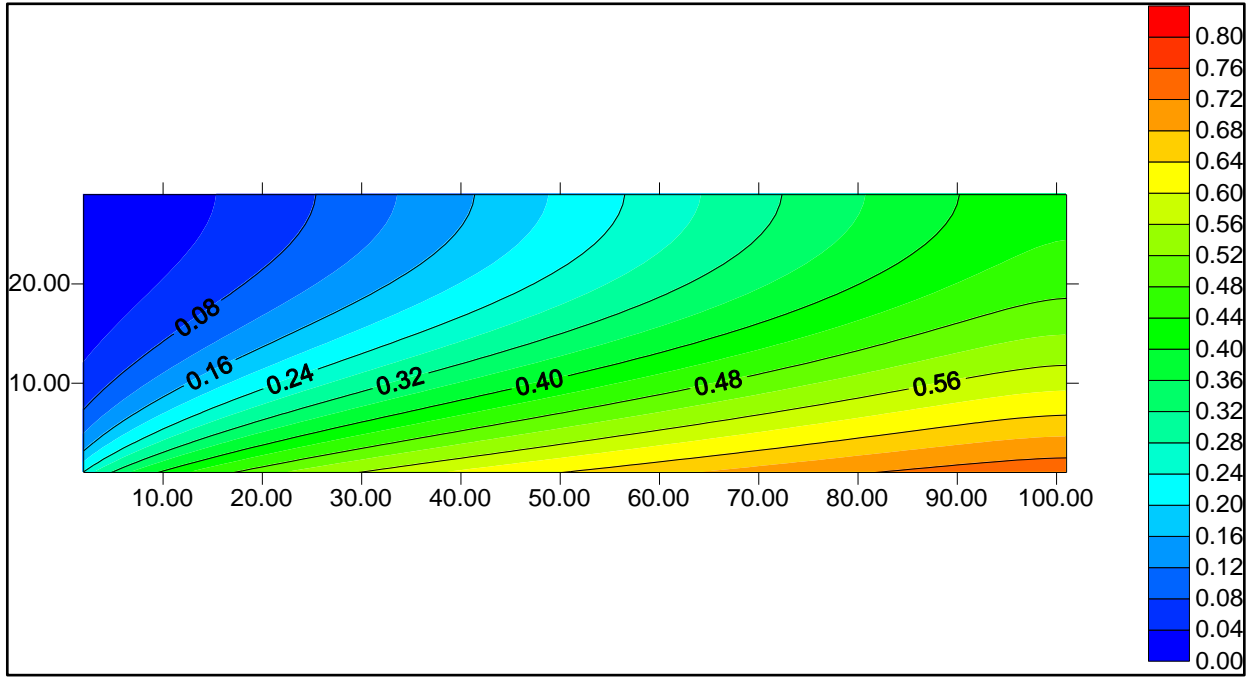


Figure 6.6. Contour plot of the normalized aqueous DCB concentration computed with the pore network model for  $Pe=36.1$  (glass beads).

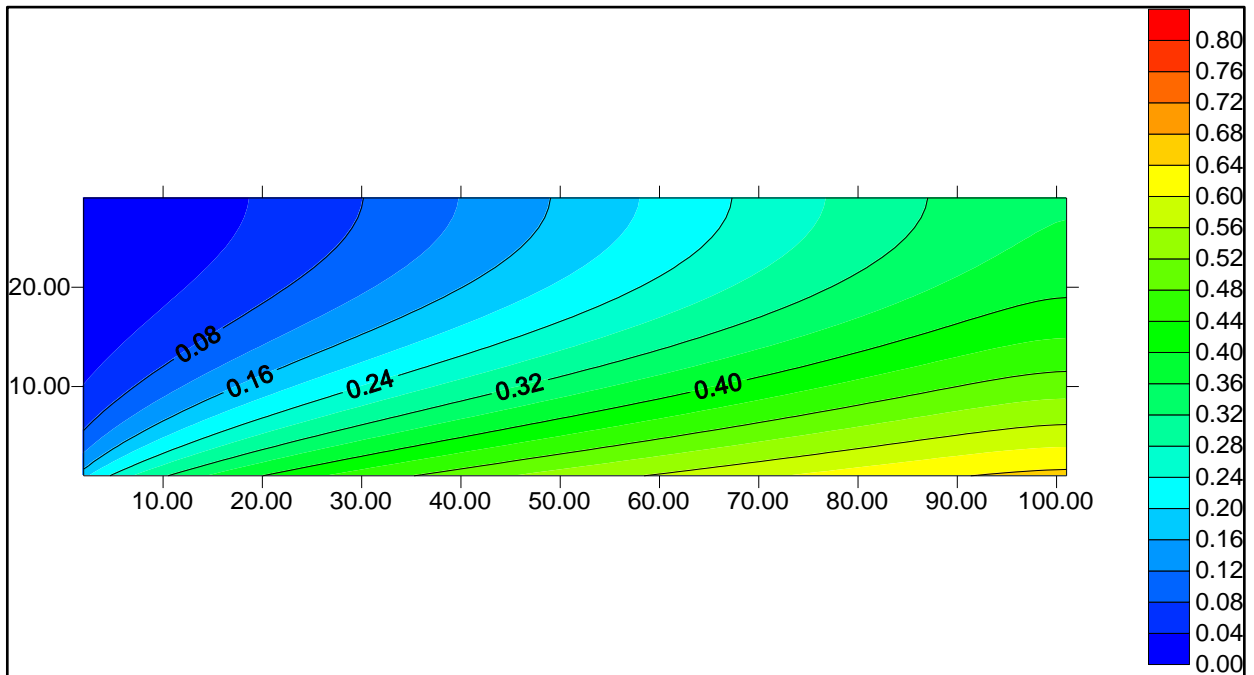


Figure 6.7. Contour plot of the normalized aqueous DCB concentration computed with the pore network model for  $Pe=79.1$  (glass beads).

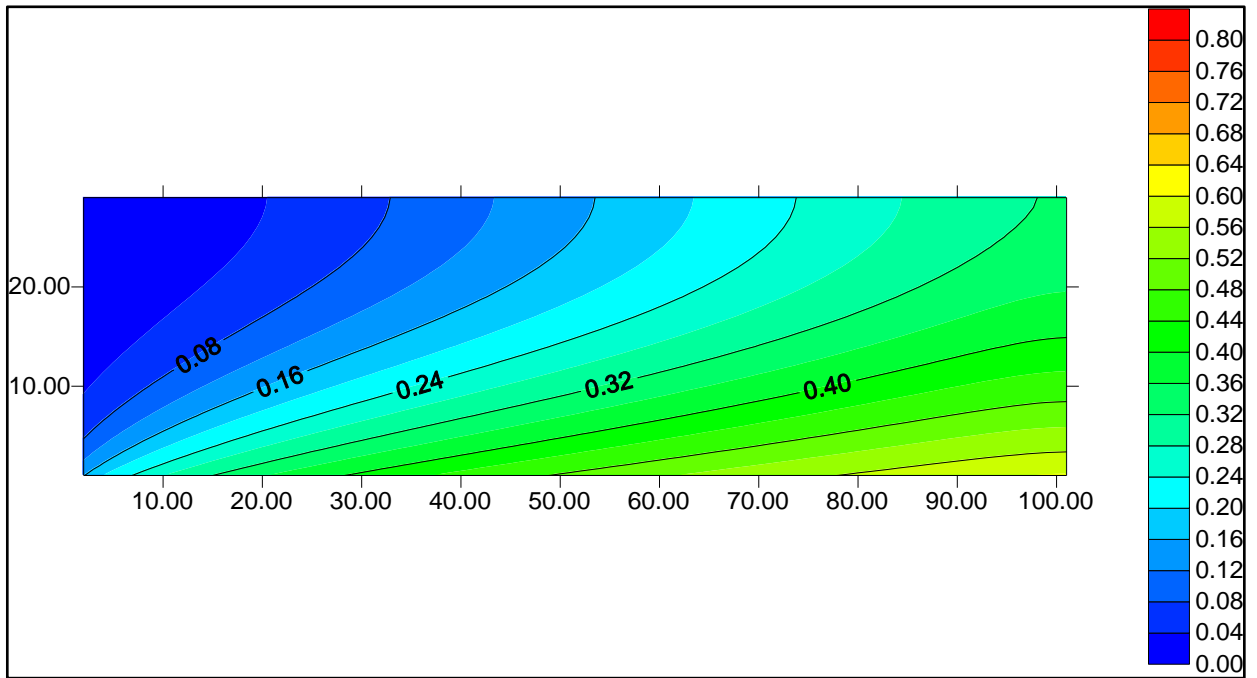


Figure 6.8. Contour plot of the normalized aqueous DCB concentration computed with the pore network model for  $Pe=163.4$  (glass beads).

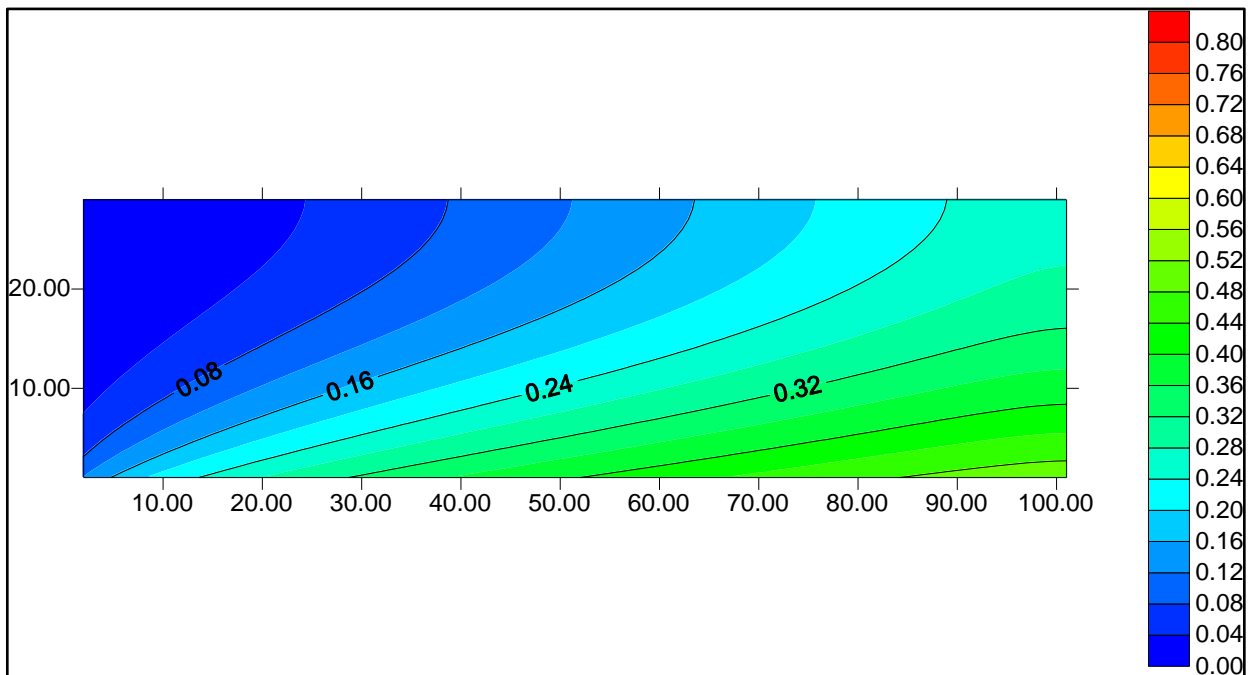


Figure 6.9. Contour plot of the normalized aqueous DCB concentration computed with the pore network model for  $Pe=334.2$  (glass beads).

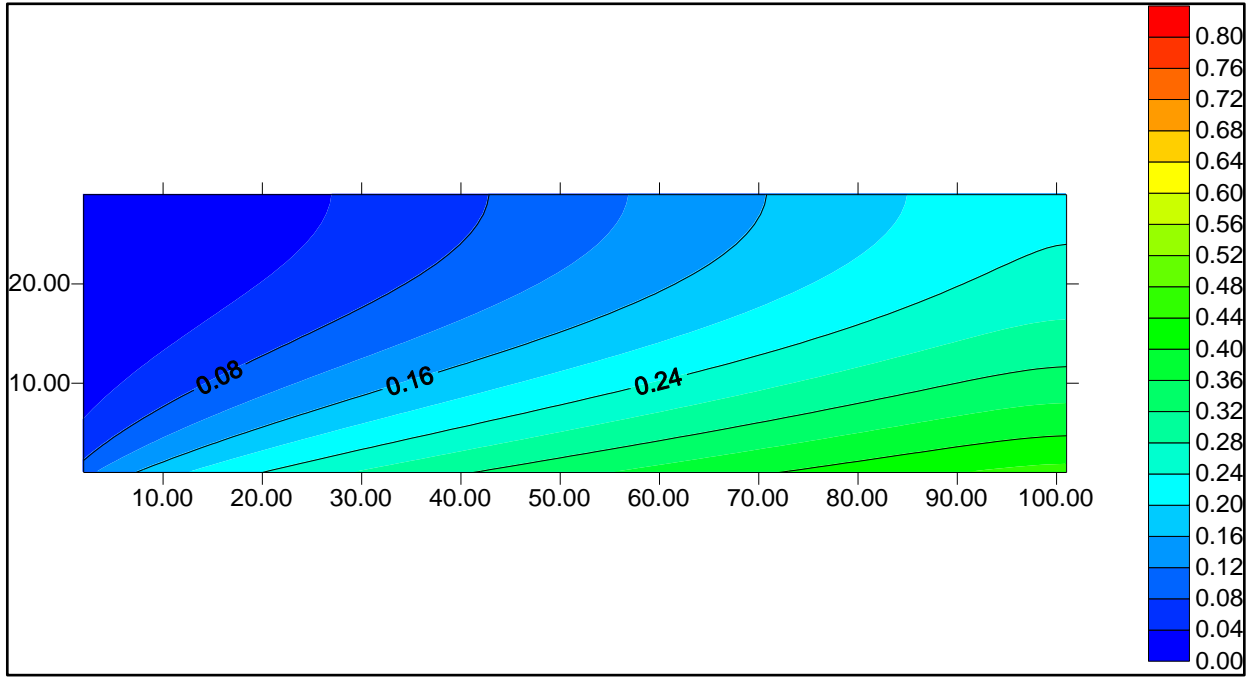


Figure 6.10. Contour plot of the normalized aqueous DCB concentration computed with the pore network model for  $Pe=515.9$  (glass beads).

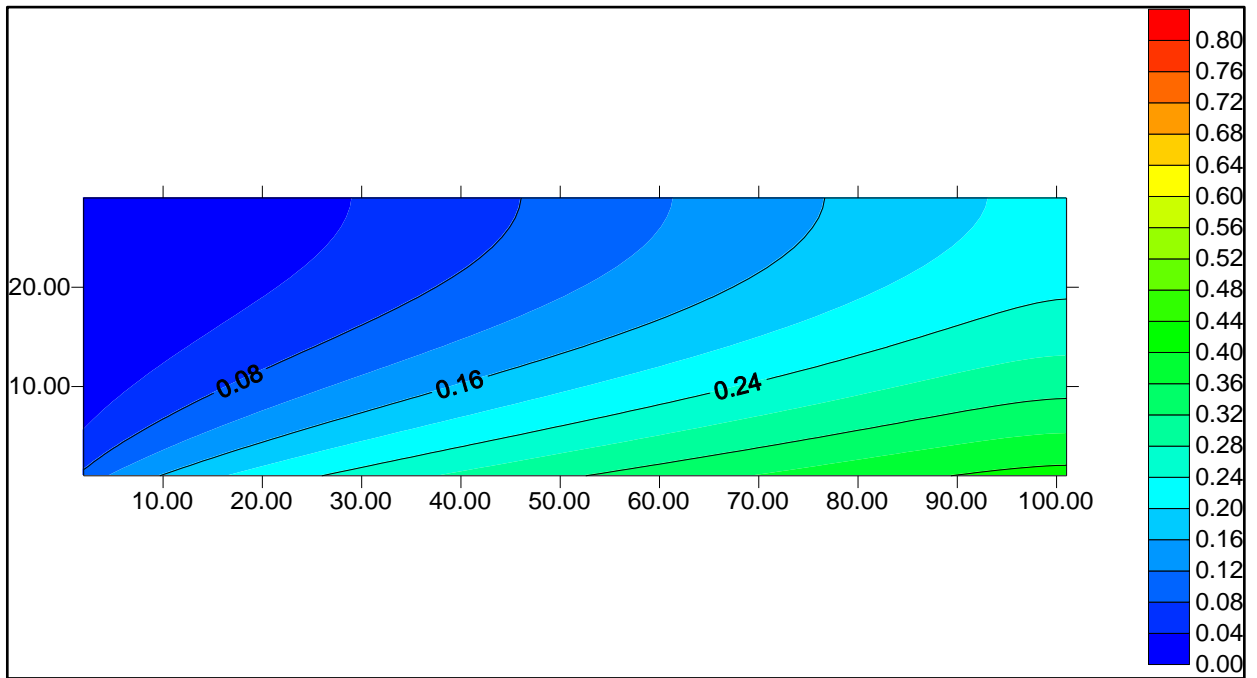


Figure 6.11. Contour plot of the normalized aqueous DCB concentration computed with the pore network model for  $Pe=980.4$  (glass beads).

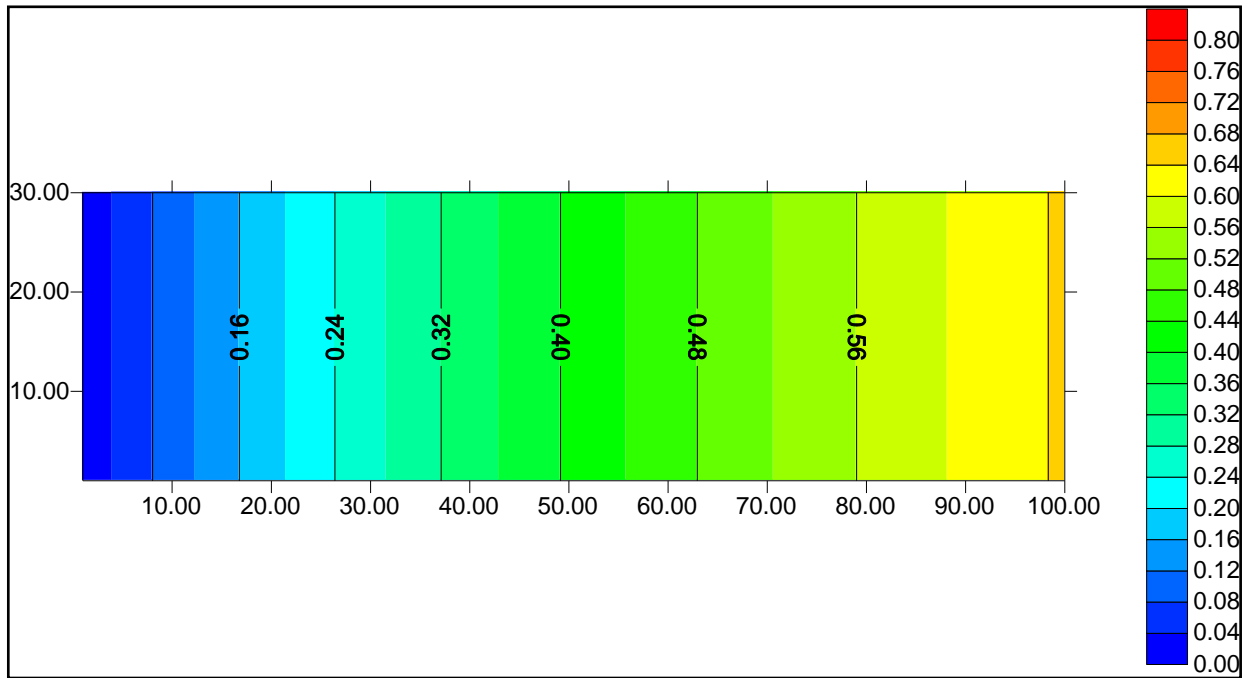


Figure 6.12. Contour plot of the normalized aqueous DCB concentration computed with the 1D analytical solution for  $Pe=8.7$  (glass beads) .

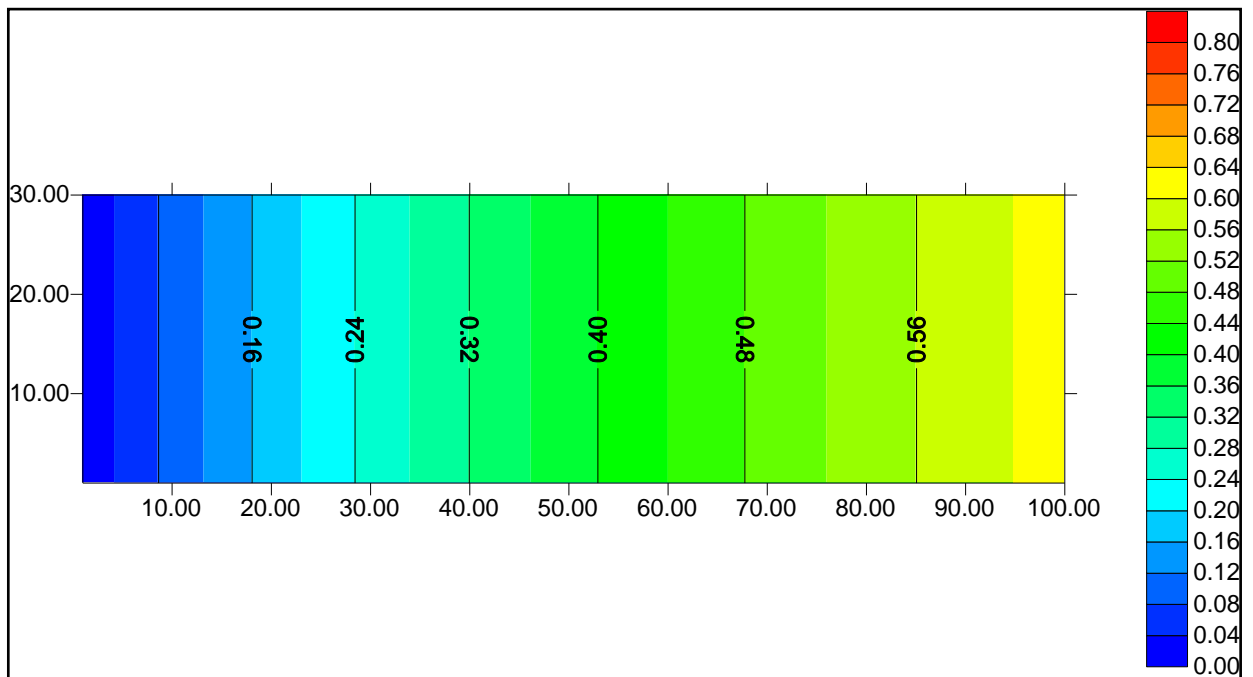


Figure 6.13. Contour plot of the normalized aqueous DCB concentration computed with the 1D analytical solution for  $Pe=13.2$  (glass beads).

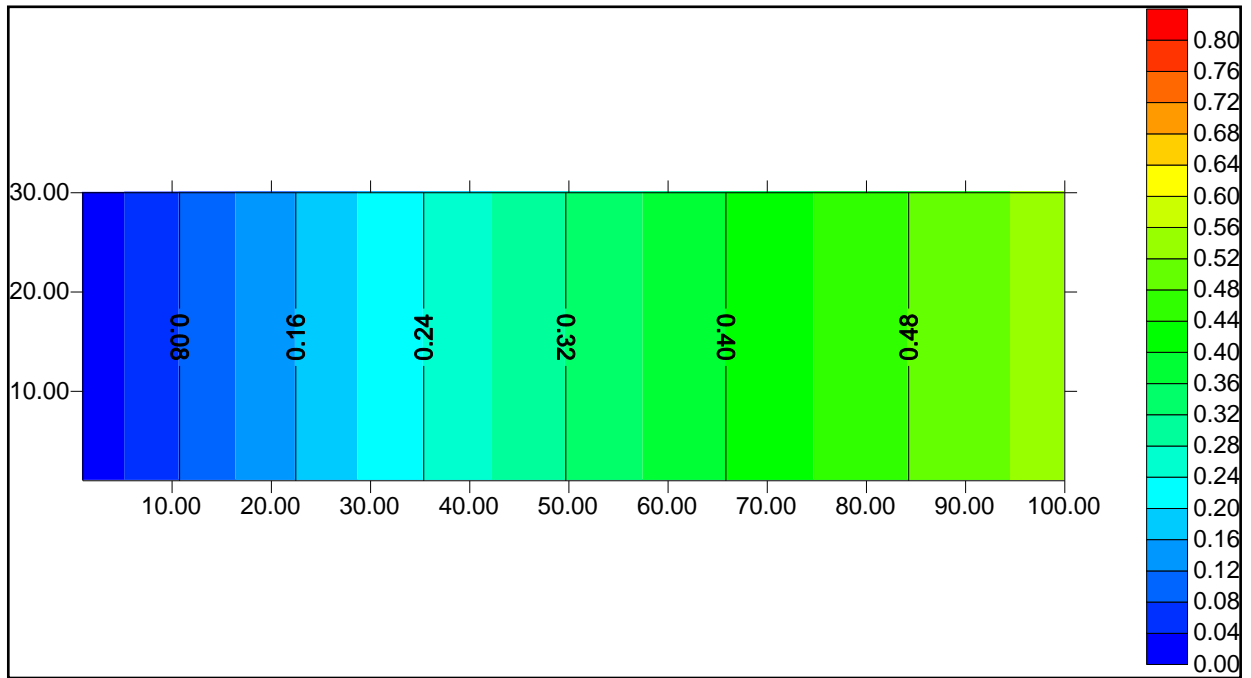


Figure 6.14. Contour plot of the normalized aqueous DCB concentration computed with the 1D analytical solution for  $Pe=36.1$  (glass beads).

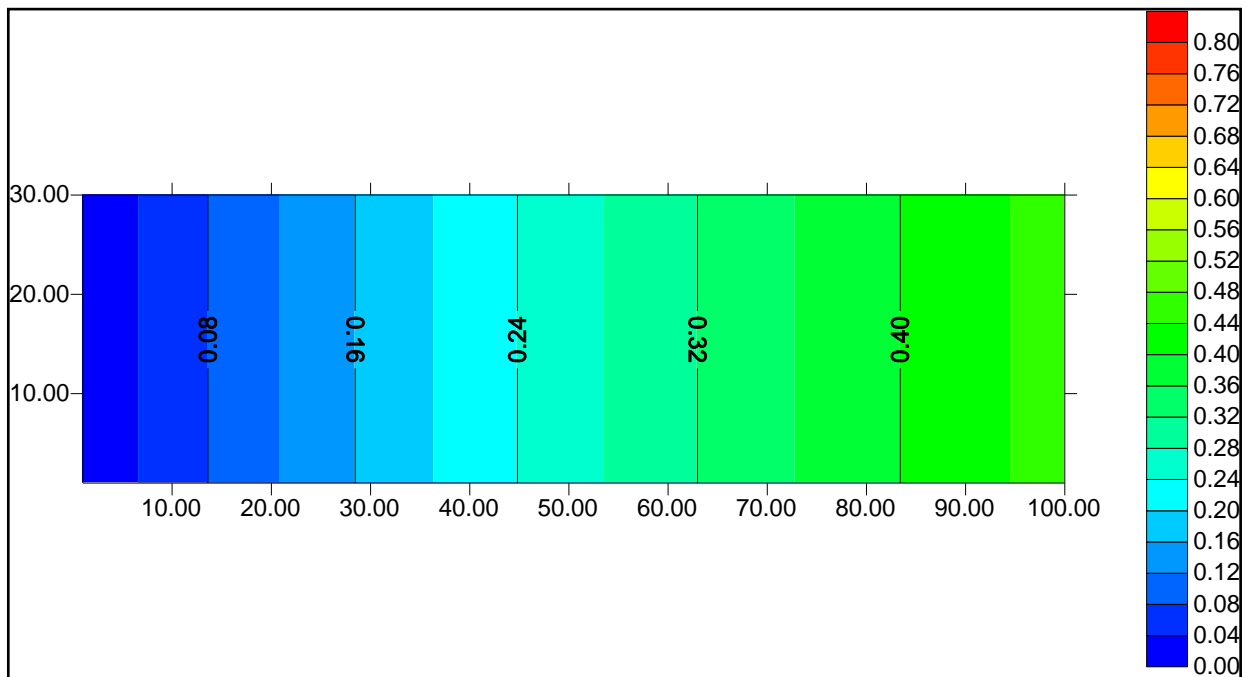


Figure 6.15. Contour plot of the normalized aqueous DCB concentration computed with 1D analytical solution for  $Pe=79.1$  (glass beads).

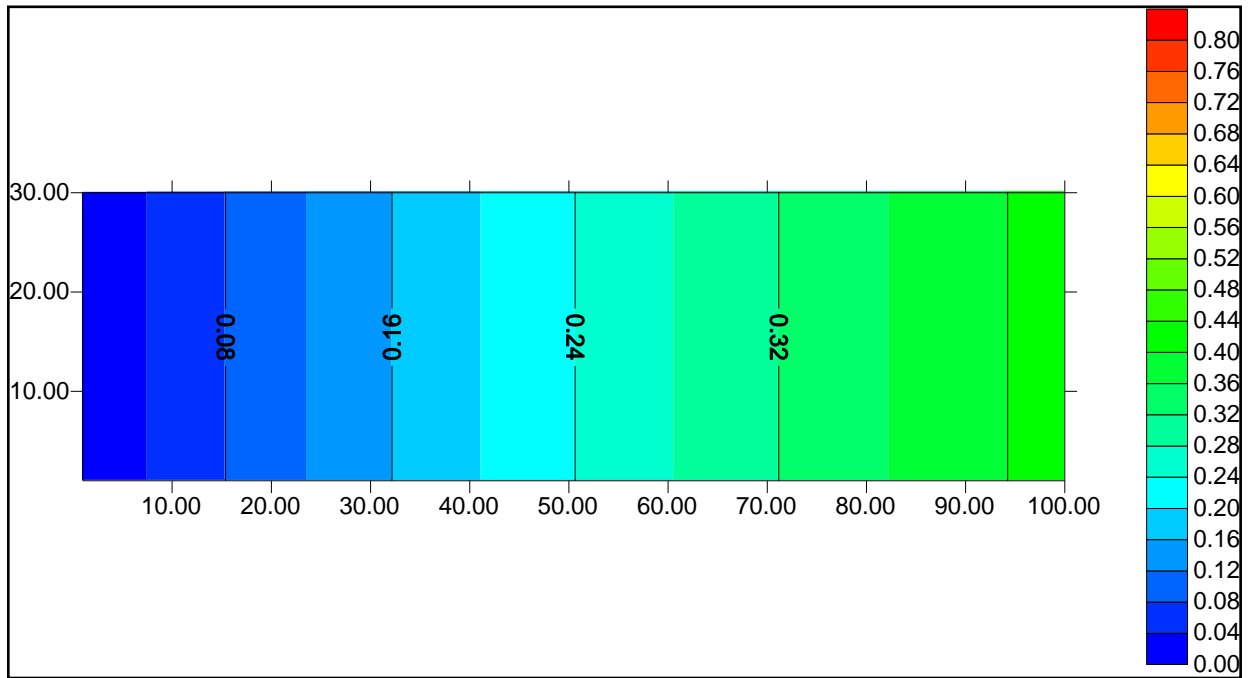


Figure 6.16. Contour plot of the normalized aqueous DCB concentration computed with the 1D analytical solution for  $Pe=163.4$  (glass beads).

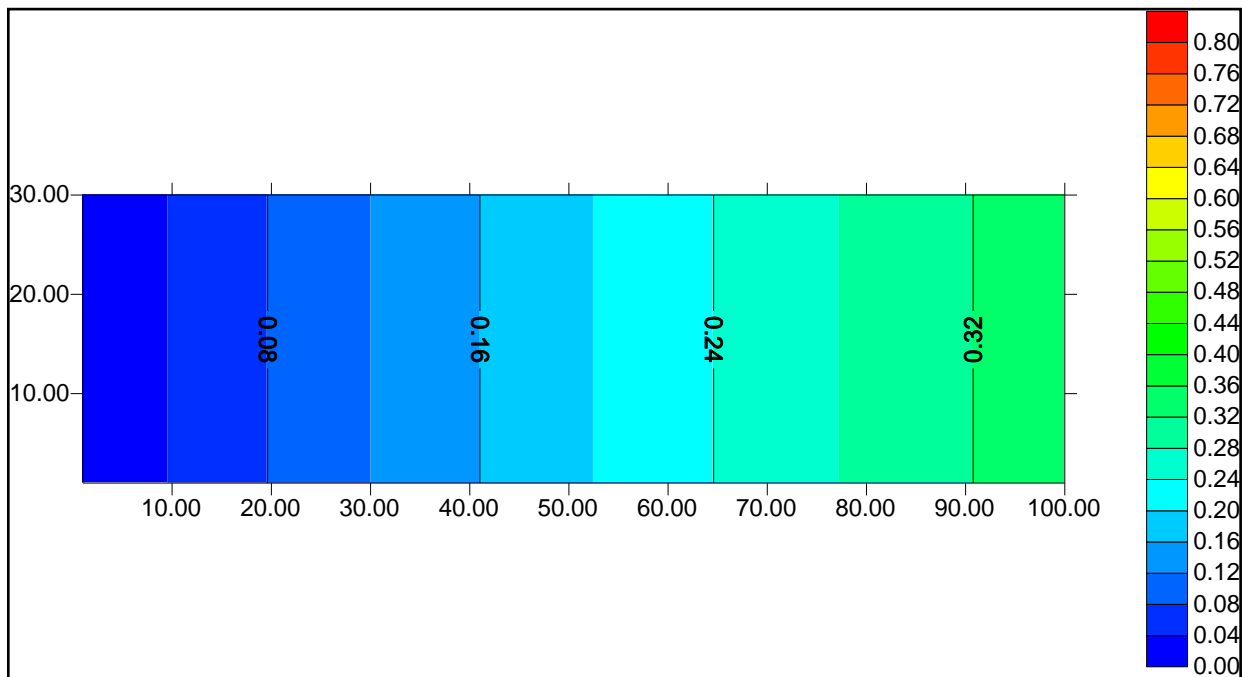


Figure 6.17. Contour plot of the normalized aqueous DCB concentration computed with the 1D analytical solution  $Pe=334.2$  (glass beads).

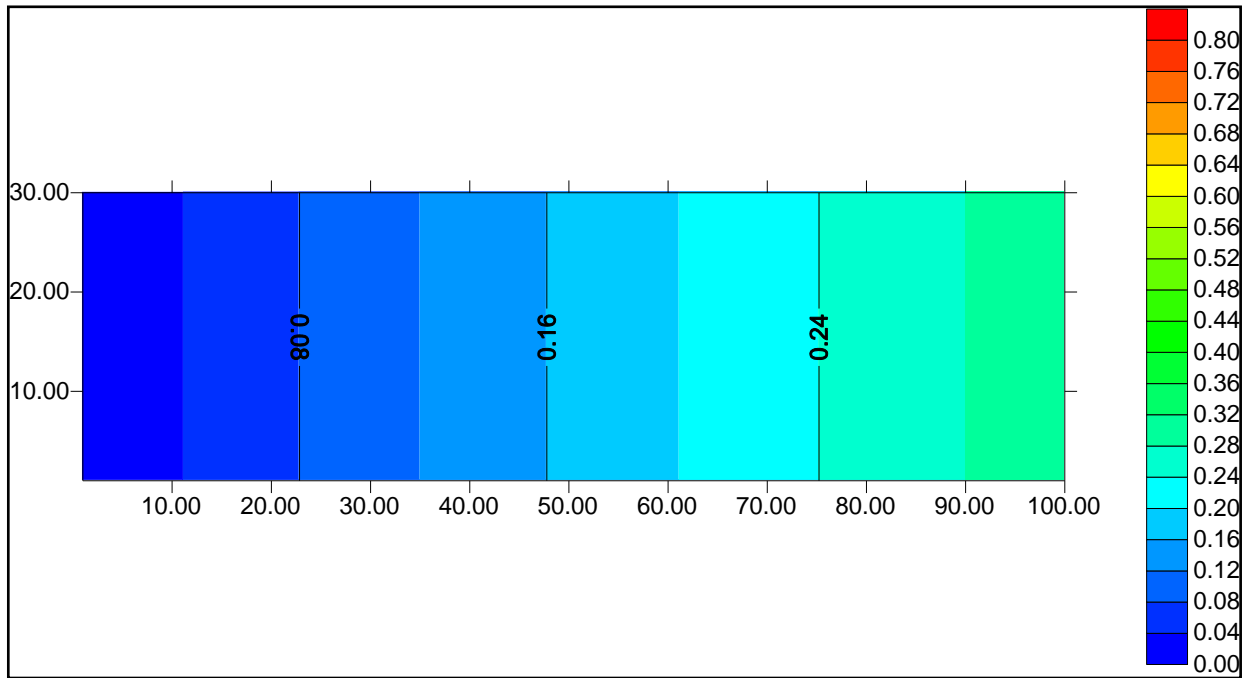


Figure 6.18. Contour plot of the normalized aqueous DCB concentration computed with the 1D analytical solution for  $Pe=515.9$  (glass beads).

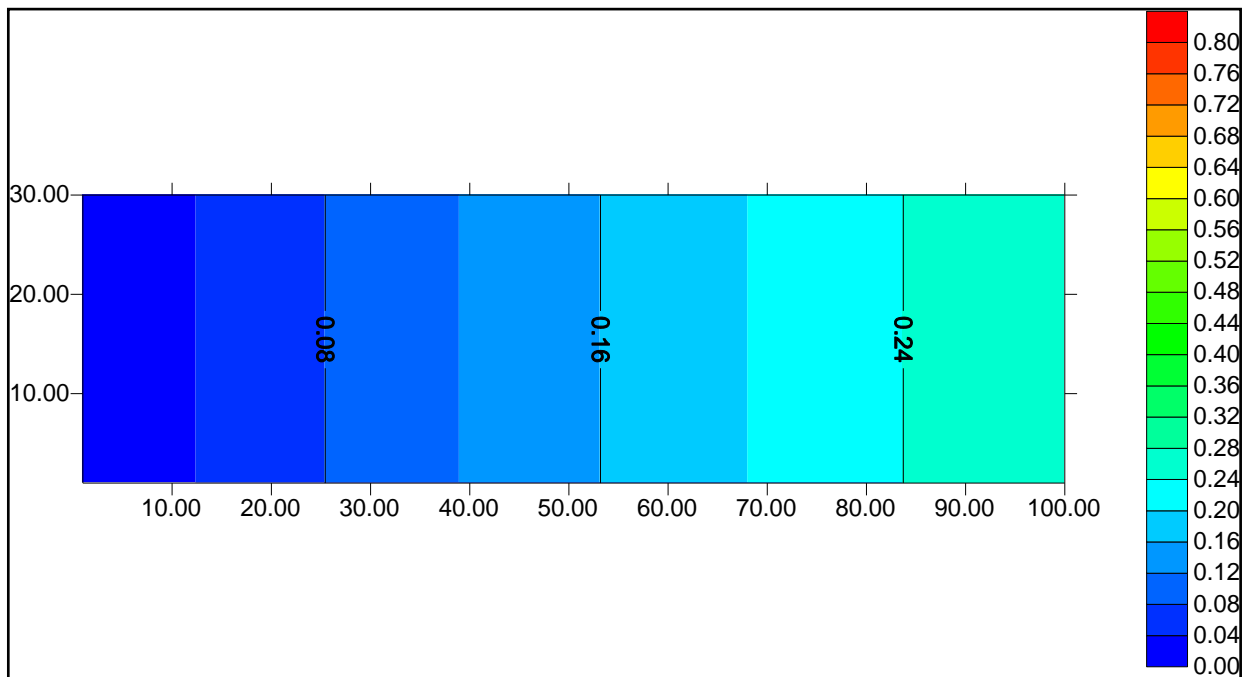


Figure 6.19. Contour plot of the normalized aqueous DCB concentration computed with the 1D analytical solution  $Pe=980.4$  (glass beads).

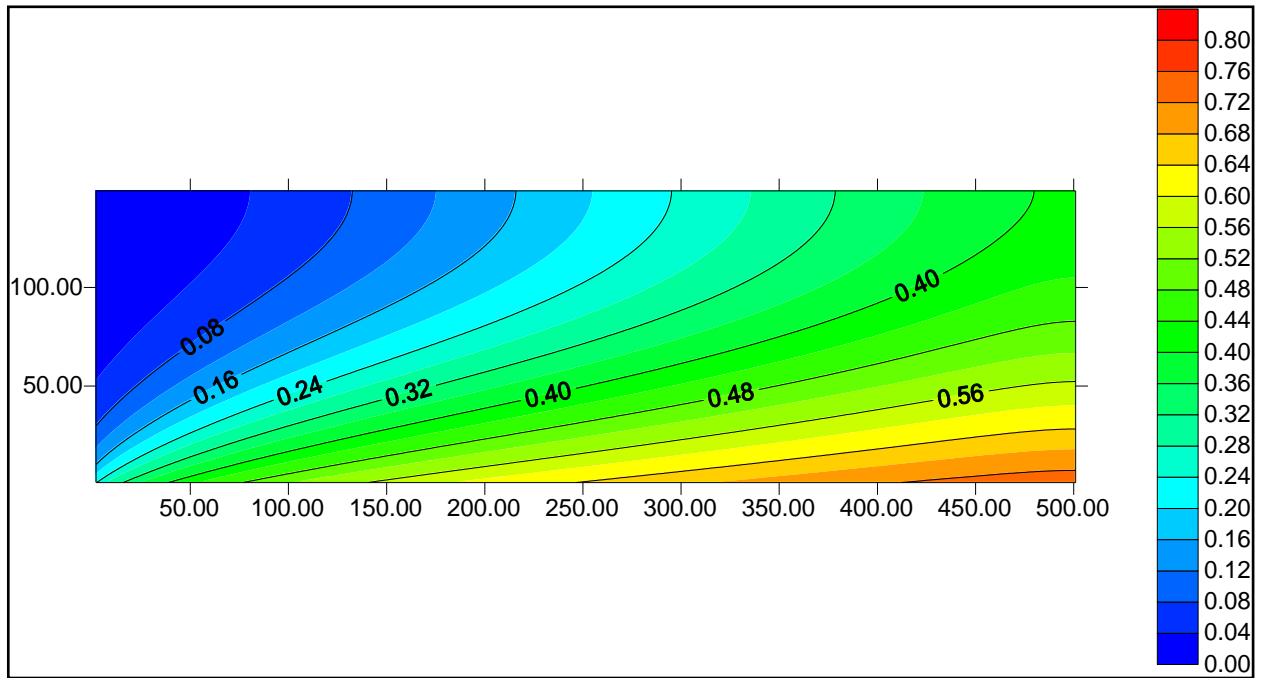


Figure 6.20. Contour plot of the normalized aqueous DCB concentration computed with the pore network model for  $Pe=1.3$  (sand).

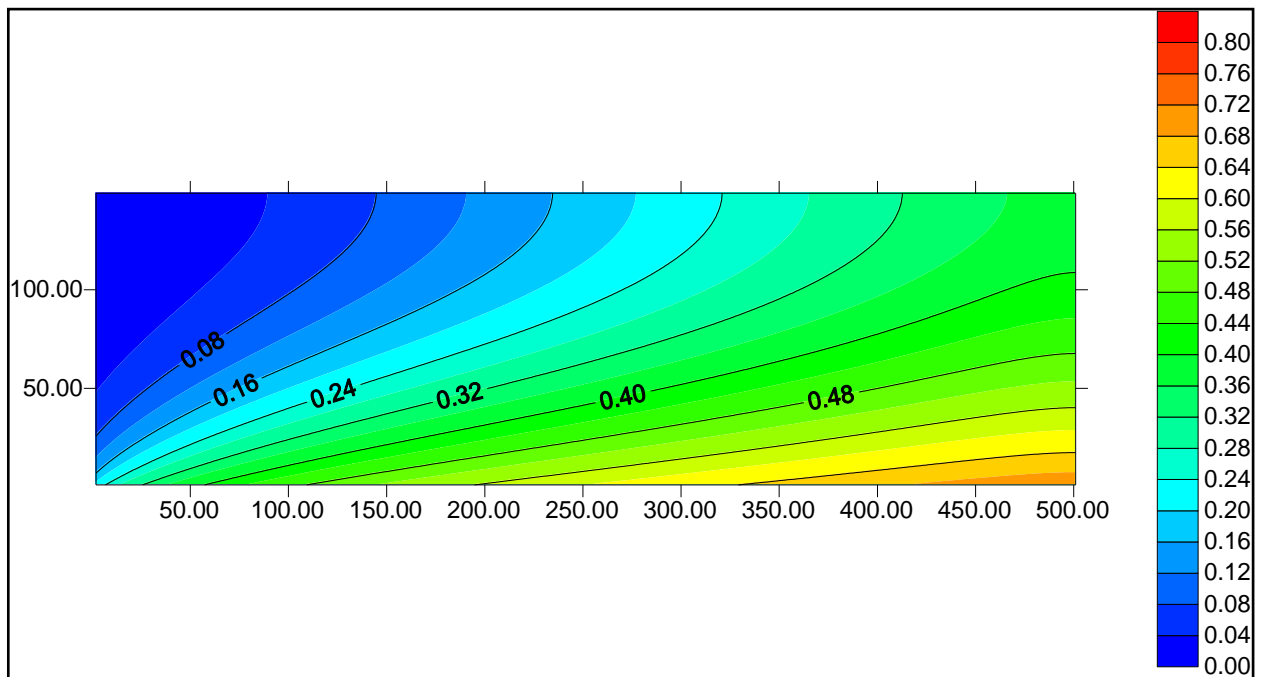


Figure 6.21. Contour plot of the normalized aqueous DCB concentration computed with the pore network model for  $Pe=1.6$  (sand).

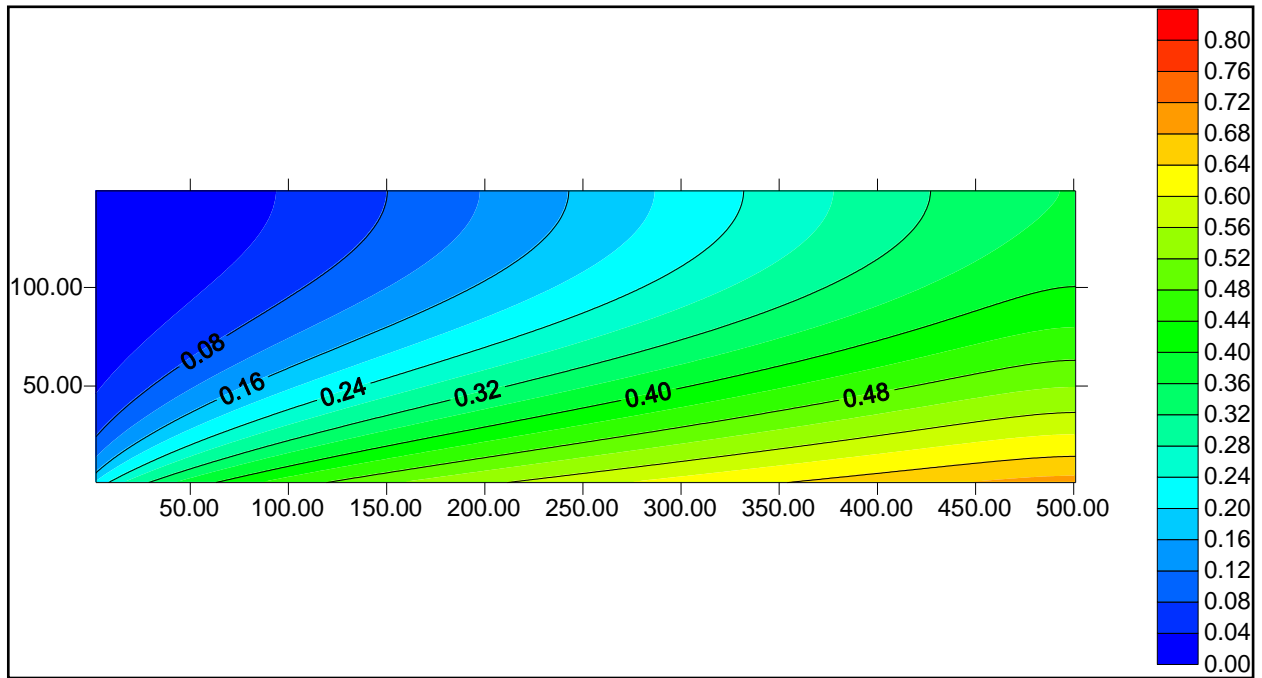


Figure 6.22. Contour plot of the normalized aqueous DCB concentration computed with the pore network model for  $Pe=2.3$  (sand).

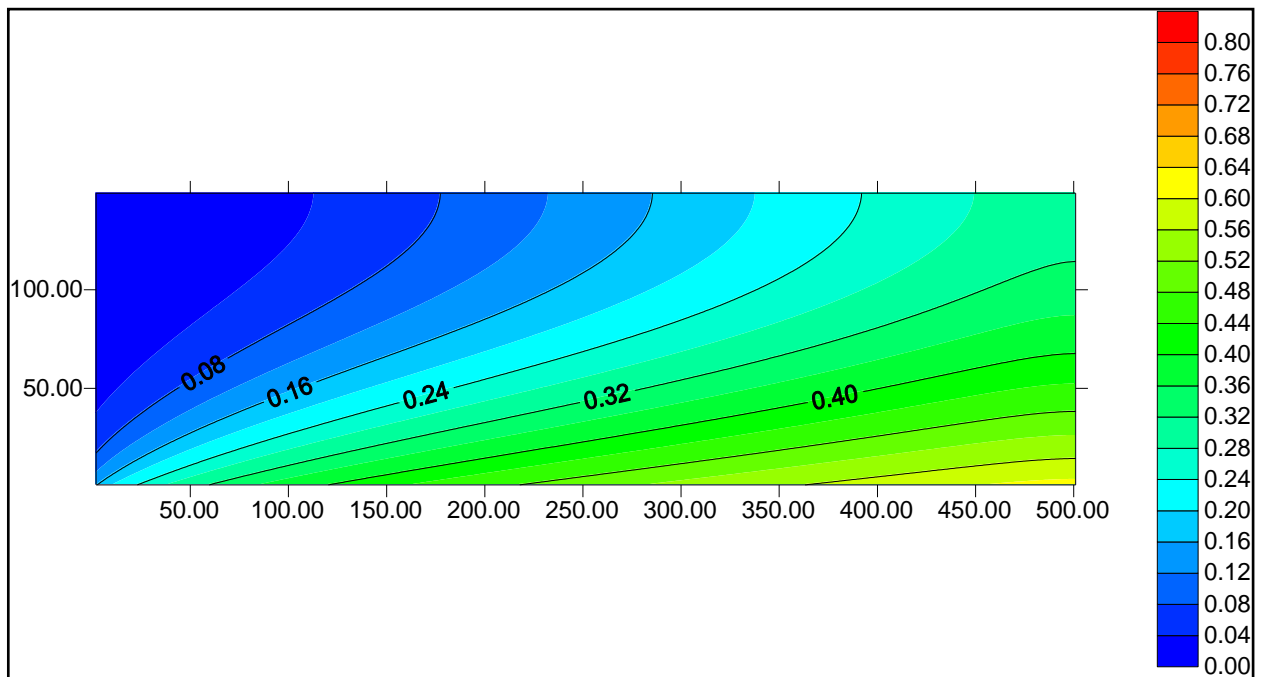


Figure 6.23. Contour plot of the normalized aqueous DCB concentration computed with the pore network model for  $Pe=8.1$  (sand).

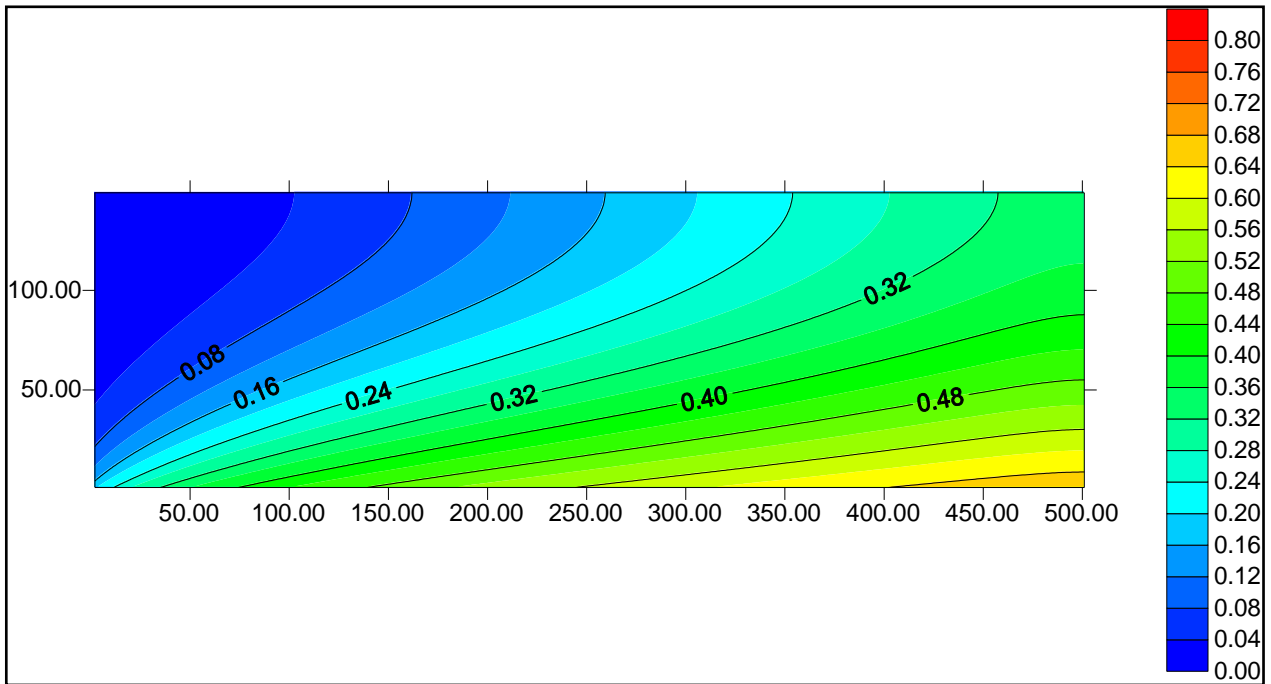


Figure 6.24. Contour plot of the normalized aqueous DCB concentration computed with the pore network model for  $Pe=15.4$  (sand).

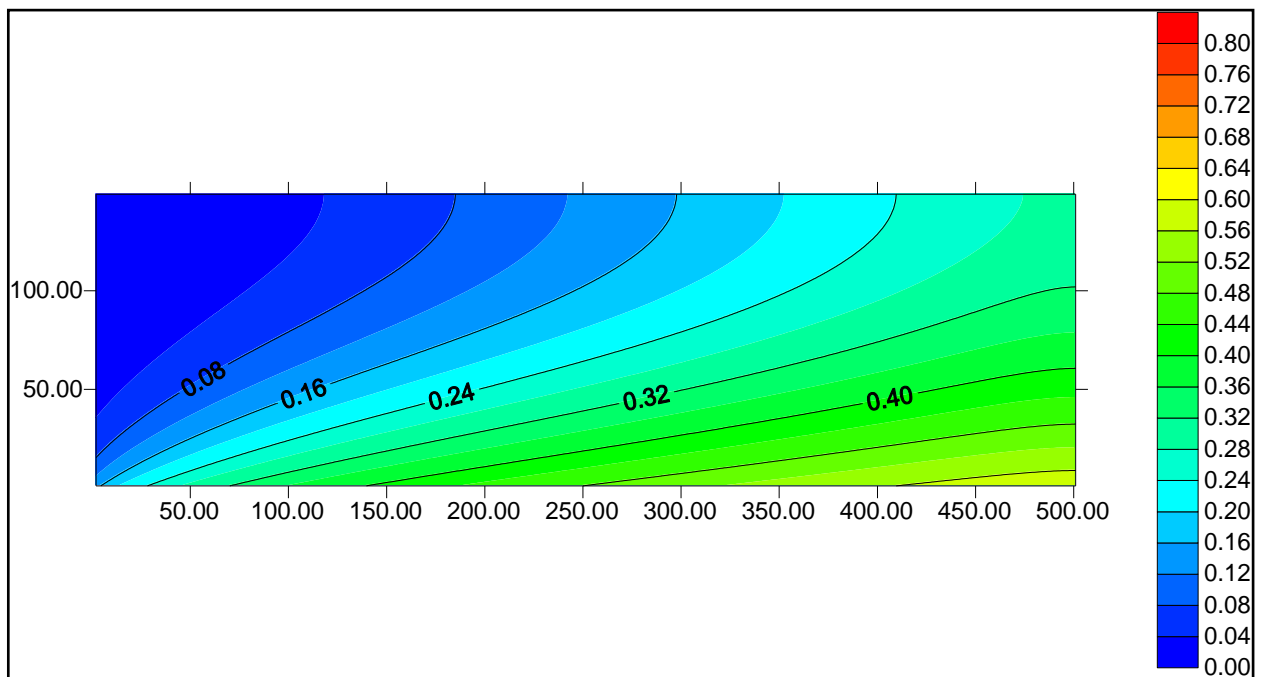


Figure 6.25. Contour plot of the normalized aqueous DCB concentration computed with the pore network model for  $Pe=30.2$  (sand).

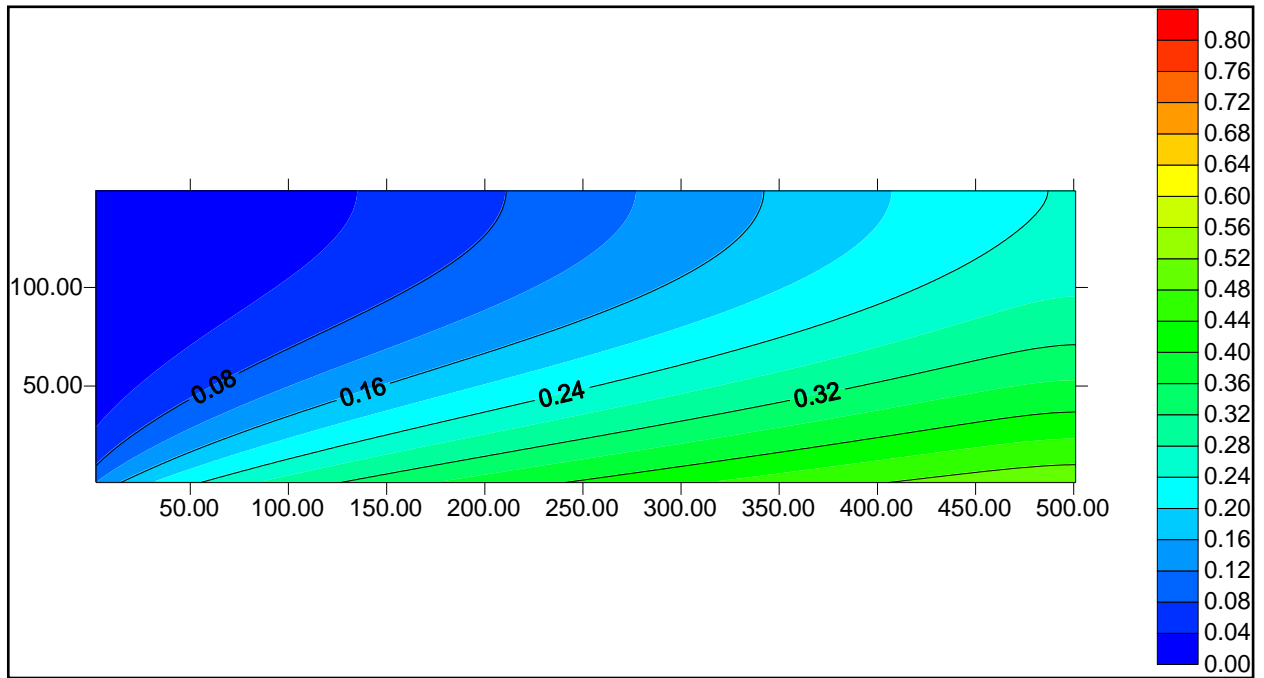


Figure 6.26. Contour plot of the normalized aqueous DCB concentration computed with the pore network model for  $Pe=59.8$  (sand).

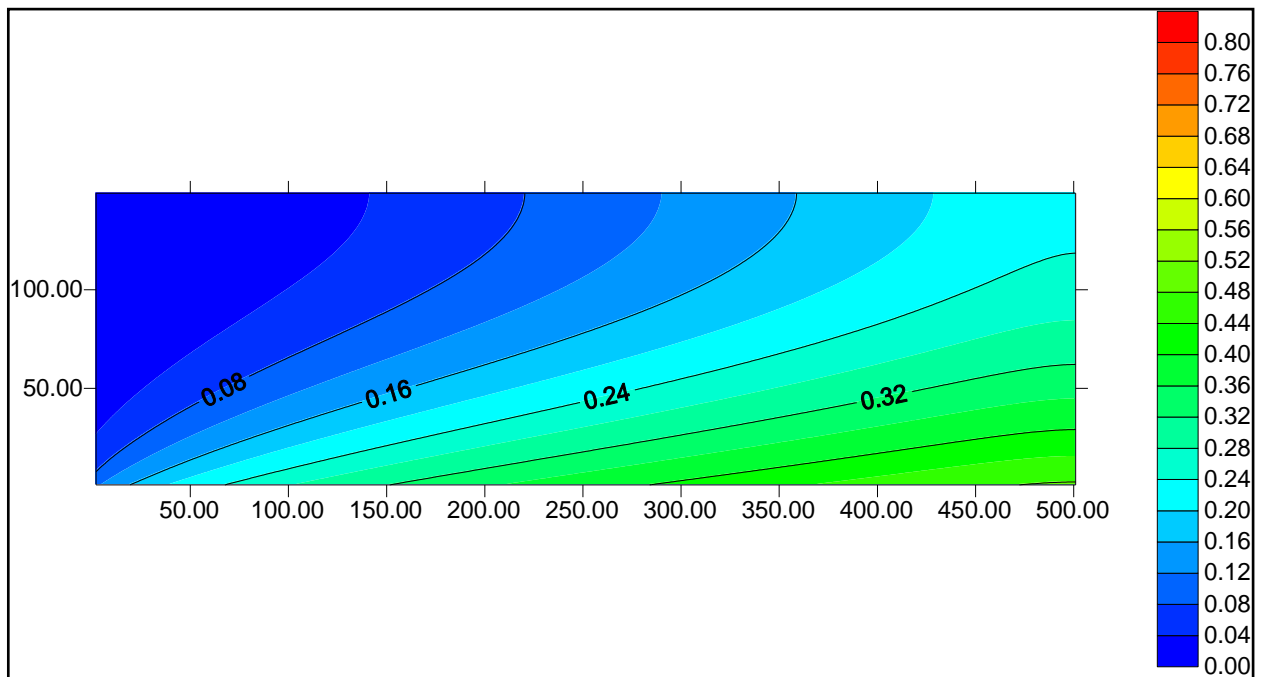


Figure 6.27. Contour plot of the normalized aqueous DCB concentration computed with the pore network model for  $Pe=99.5$  (sand).

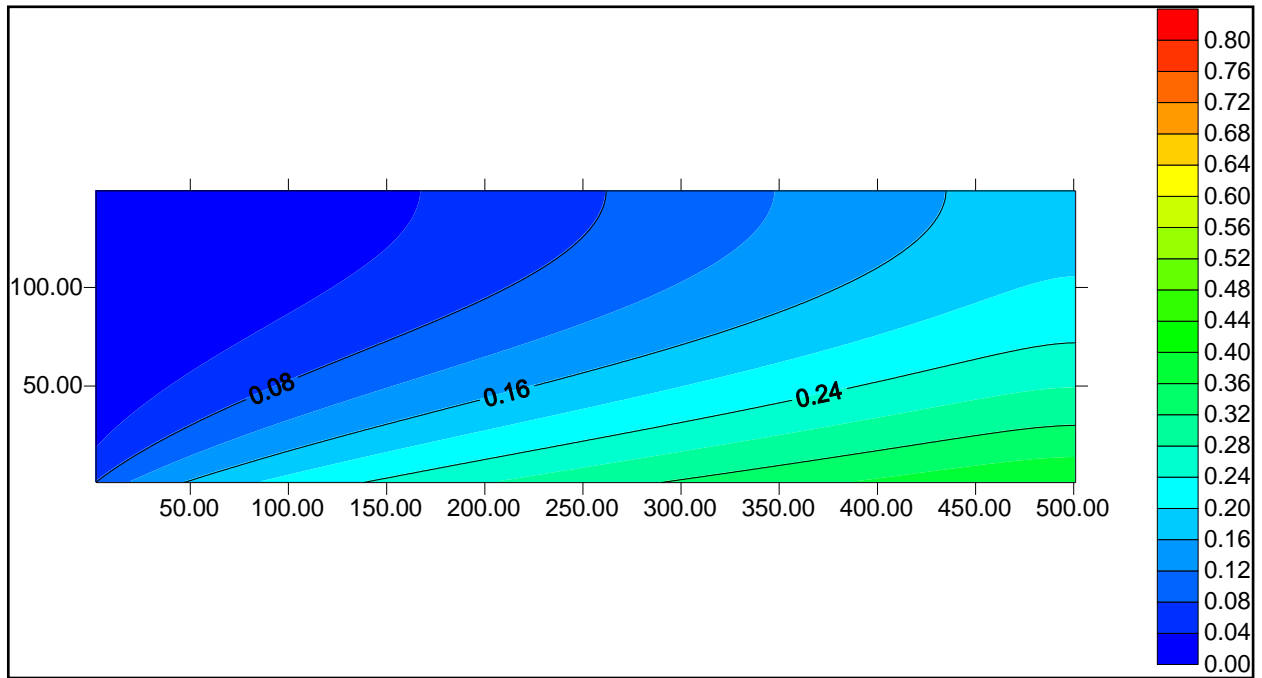


Figure 6.28. Contour plot of the normalized aqueous DCB concentration computed with the pore network model for  $Pe=185.2$  (sand).

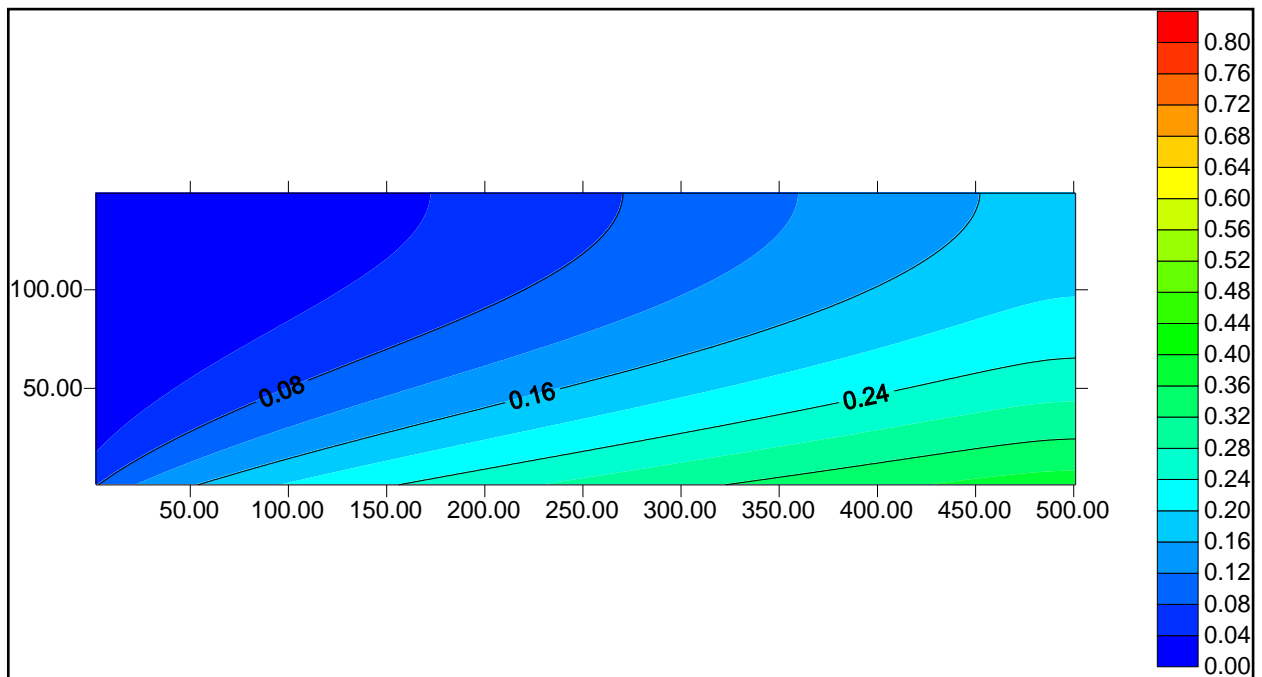


Figure 6.29. Contour plot of the normalized aqueous DCB concentration computed with the pore network model for  $Pe=216.0$  (sand).

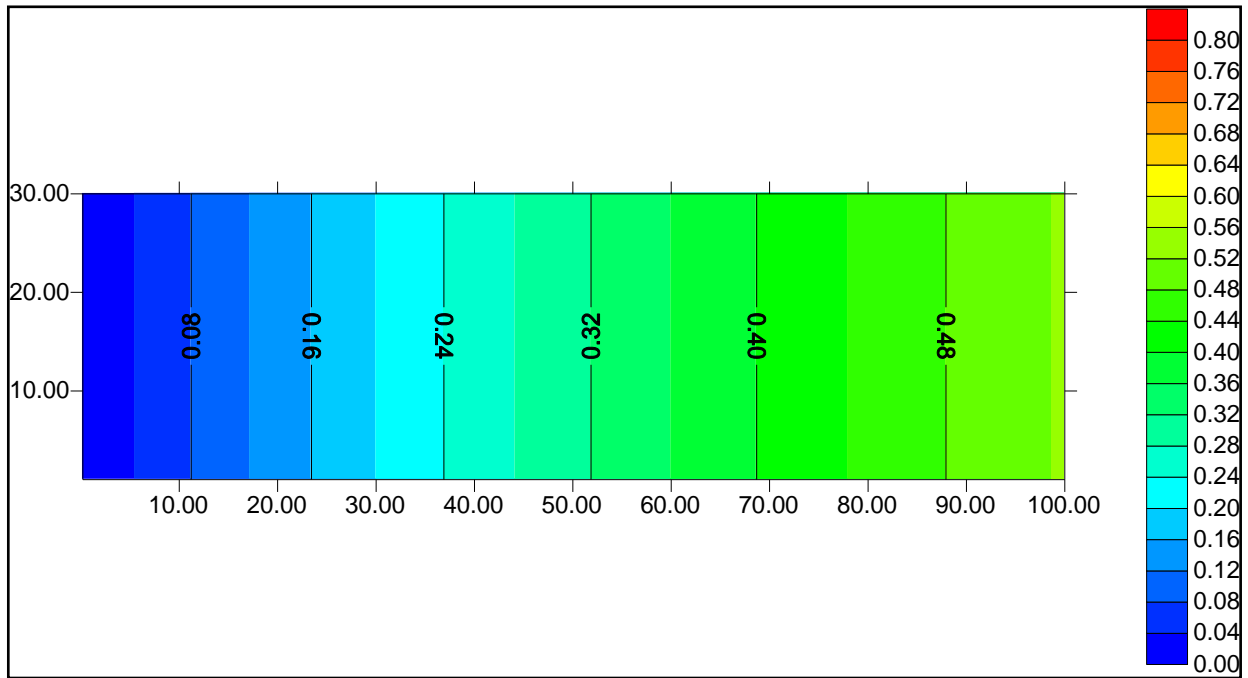


Figure 6.30. Contour plot of the normalized aqueous DCB concentration computed with the 1D analytical solution for  $Pe=1.3$  (sand).

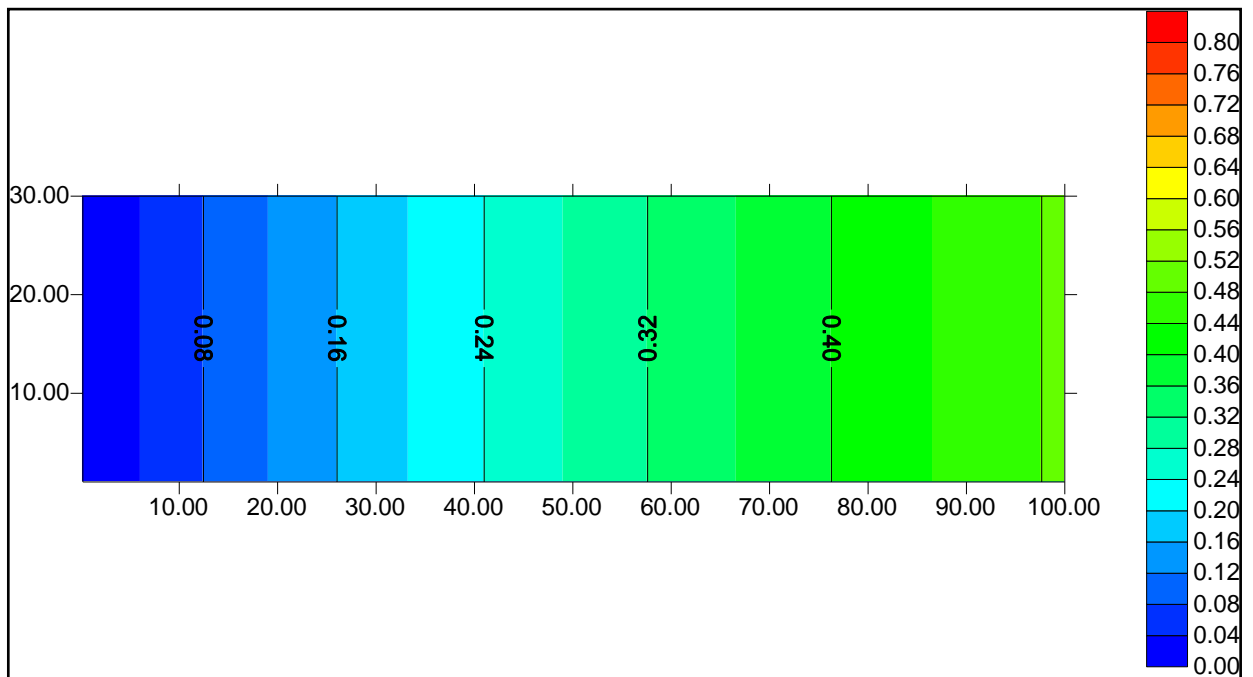


Figure 6.31. Contour plot of the normalized aqueous DCB concentration computed with the 1D analytical solution for  $Pe=1.6$  (sand).

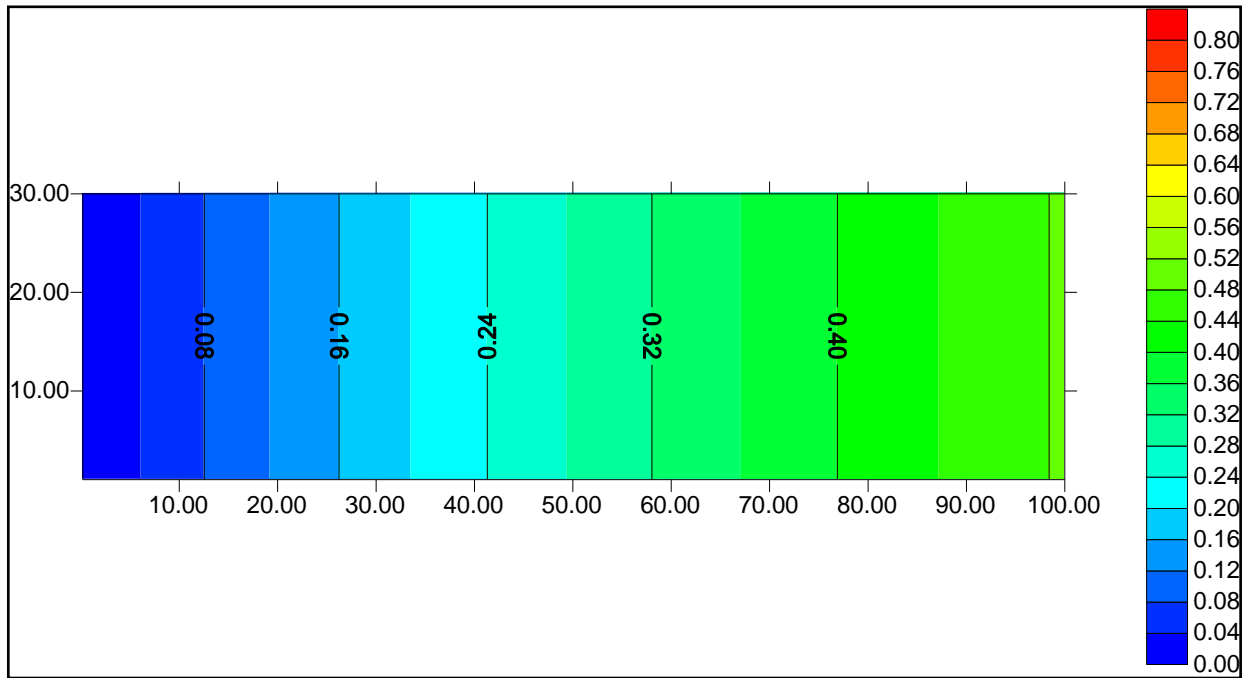


Figure 6.32. Contour plot of the normalized aqueous DCB concentration computed with the 1D analytical solution for  $Pe=2.3$  (sand).

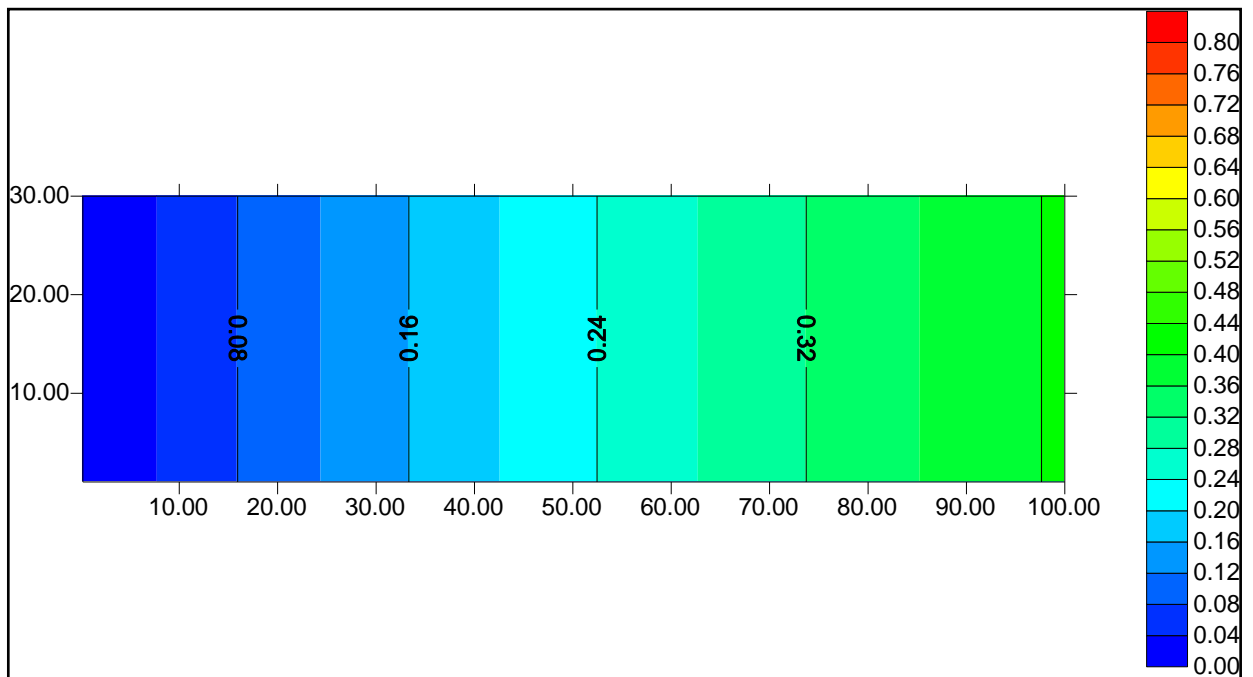


Figure 6.33. Contour plot of the normalized aqueous DCB concentration computed with the 1D analytical solution for  $Pe=8.1$  (sand).

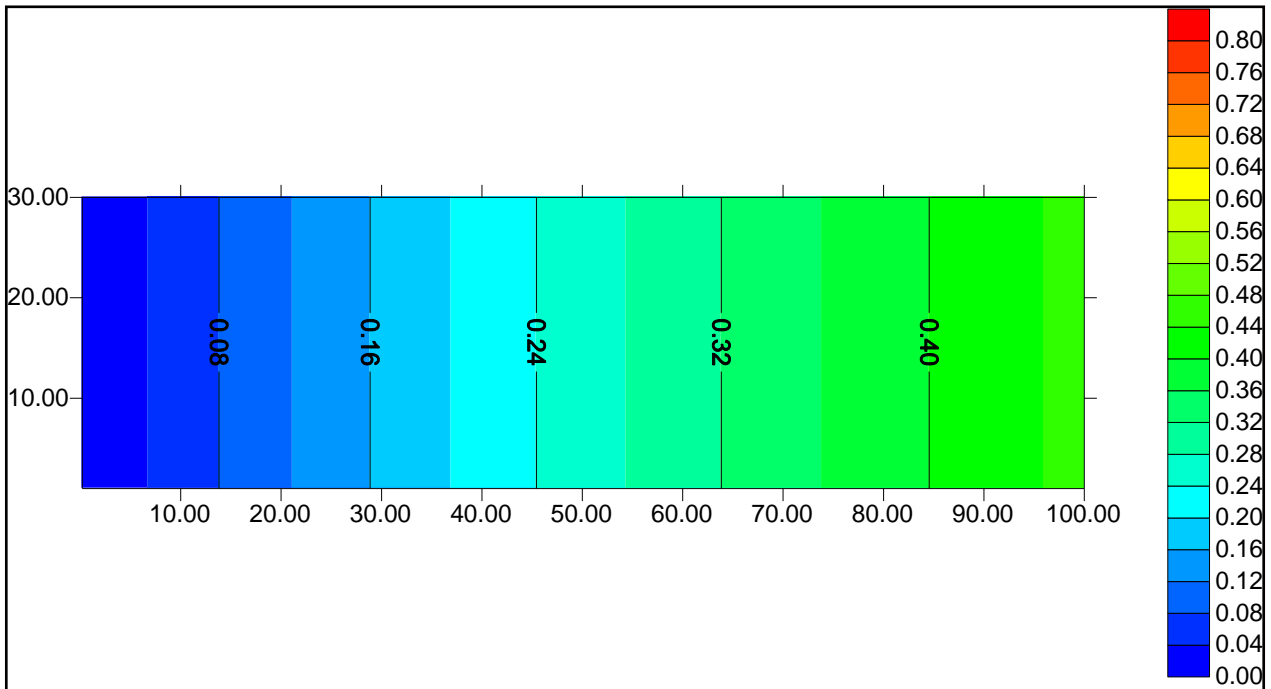


Figure 6.34. Contour plot of the normalized aqueous DCB concentration computed with the 1D analytical solution for  $Pe=15.4$  (sand).

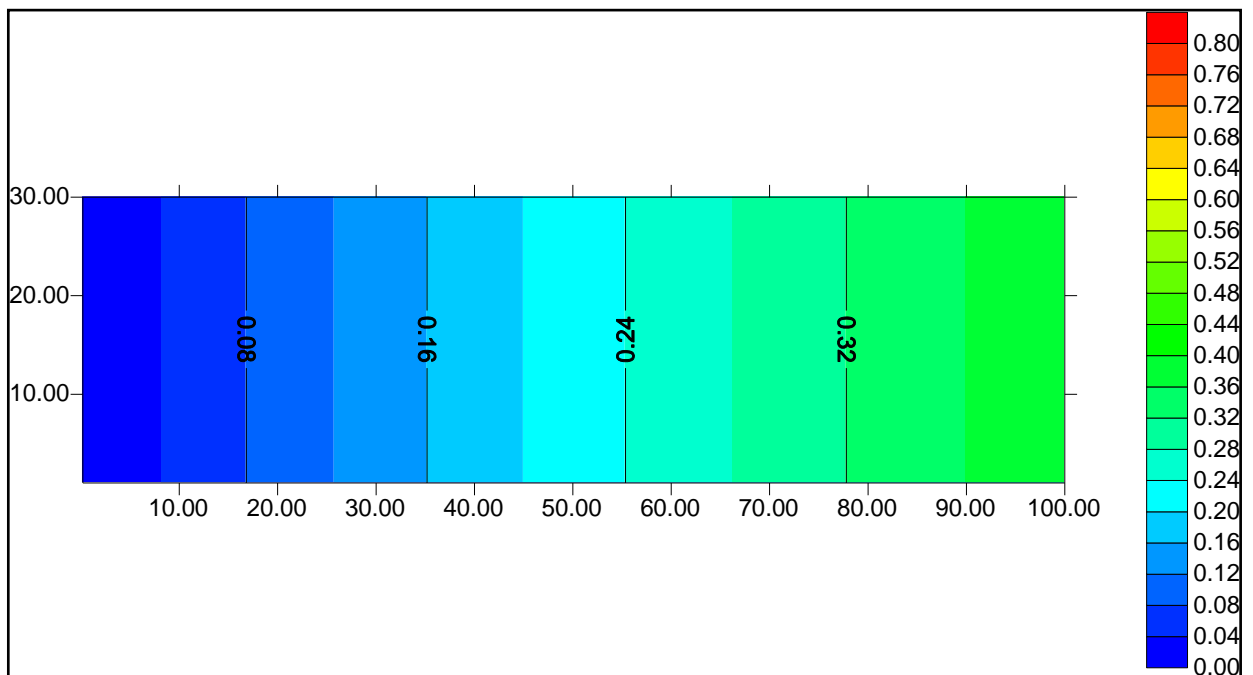


Figure 6.35. Contour plot of the normalized aqueous DCB concentration computed with the 1D analytical solution for  $Pe=30.2$  (sand).

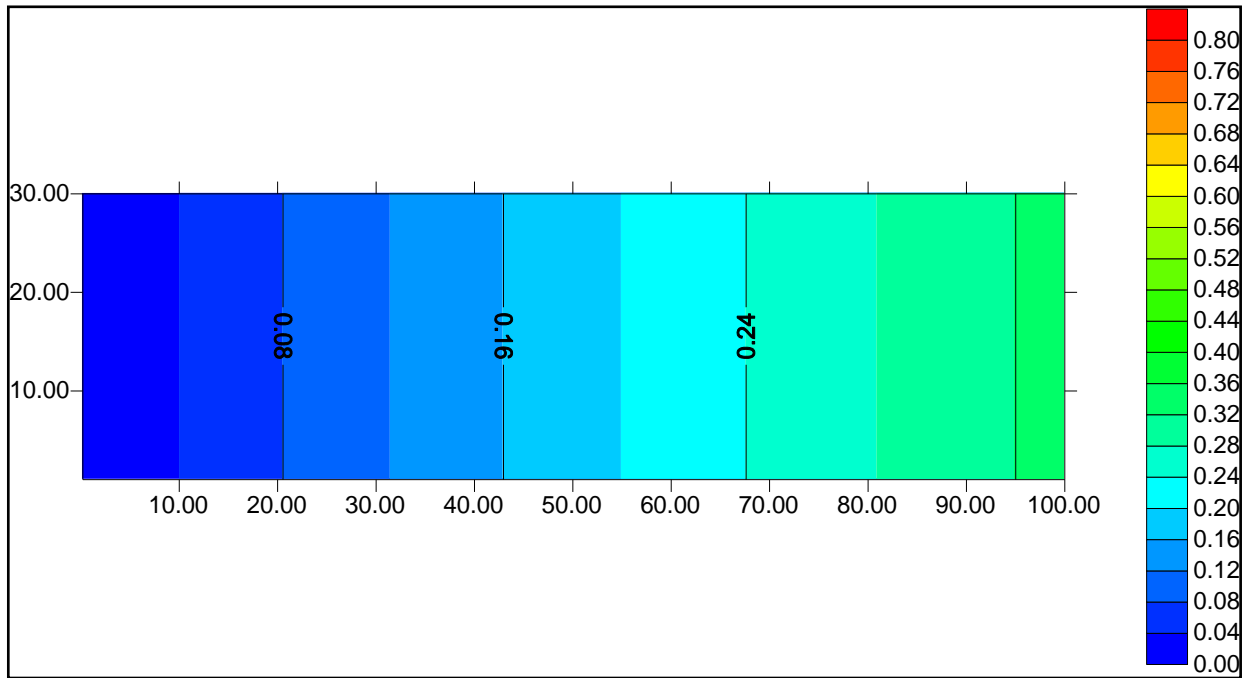


Figure 6.36 Contour plot of the normalized aqueous DCB concentration computed with the 1D analytical solution for  $Pe=59.8$  (sand).

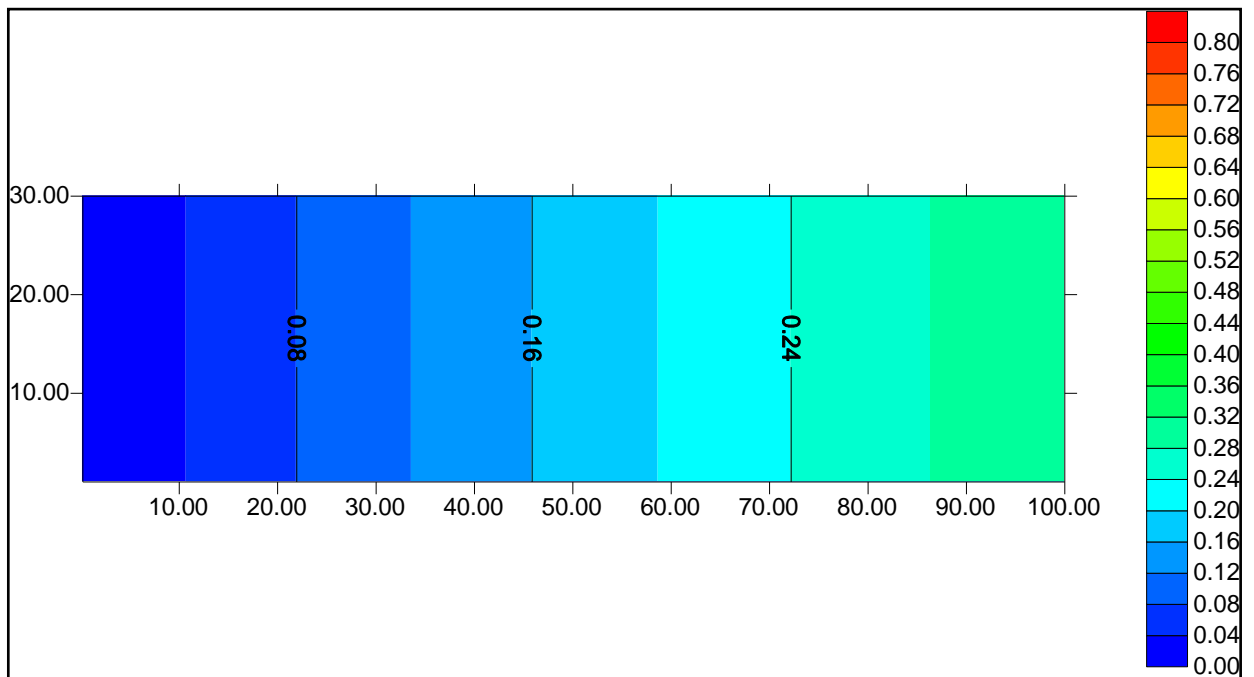


Figure 6.37. Contour plot of the normalized aqueous DCB concentration computed with the 1D analytical solution for  $Pe=99.5$  (sand).

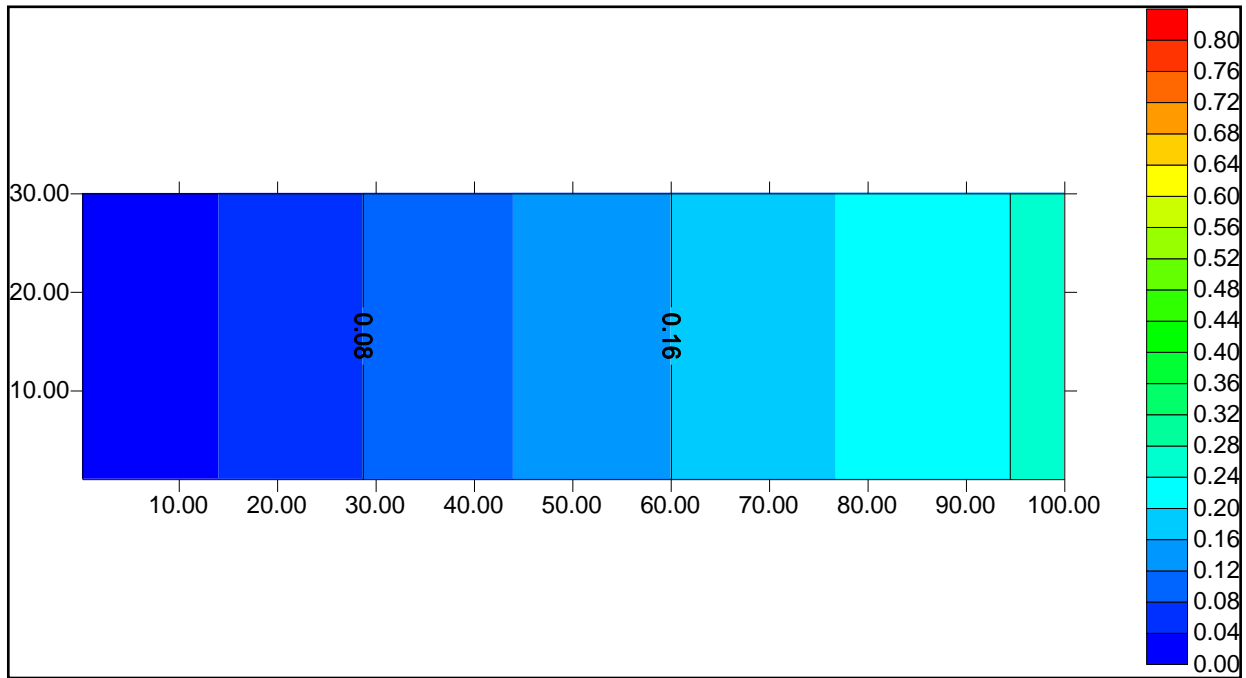


Figure 6.38. Contour plot of the normalized aqueous DCB concentration computed with the 1D analytical solution for  $Pe=185.2$  (sand).

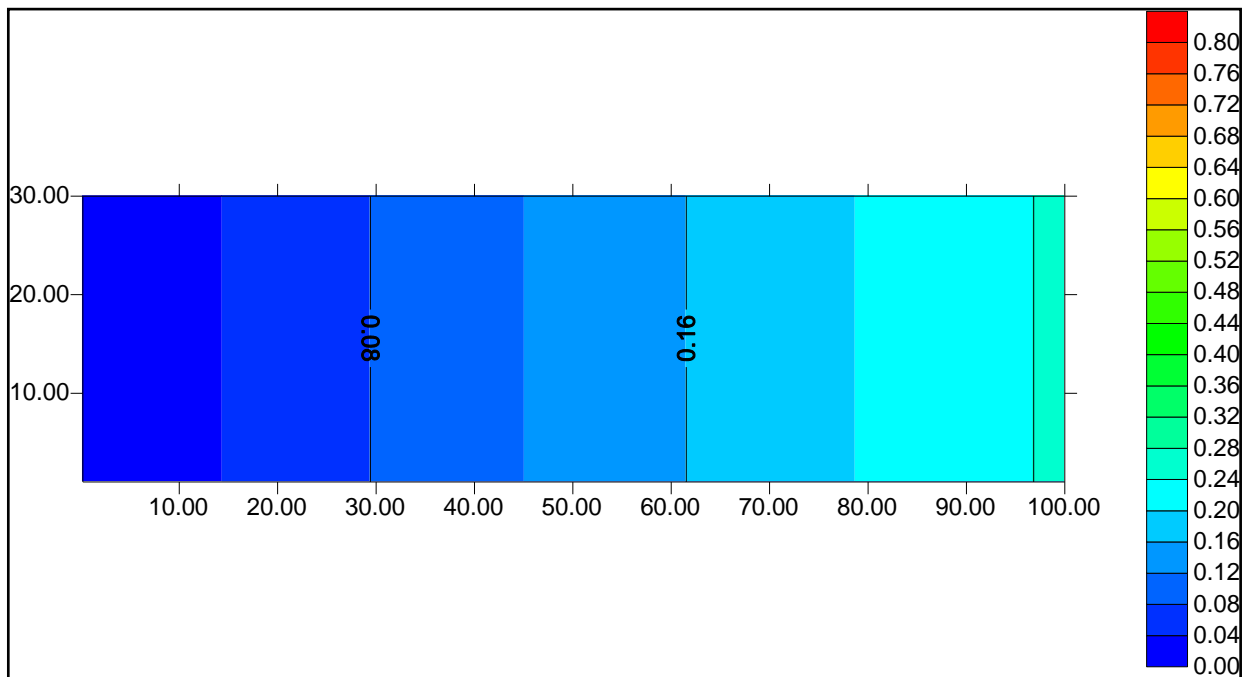


Figure 6.39. Contour plot of the normalized aqueous DCB concentration computed with the 1D analytical solution for  $Pe=216.0$  (sand).

Figure 6.40 a and b compare the determined mass transfer coefficients as a function of the Peclet number. The best-fit mass transfer coefficient determined from the pore network model shows a similar trend with the analytically determined mass transfer coefficient values.

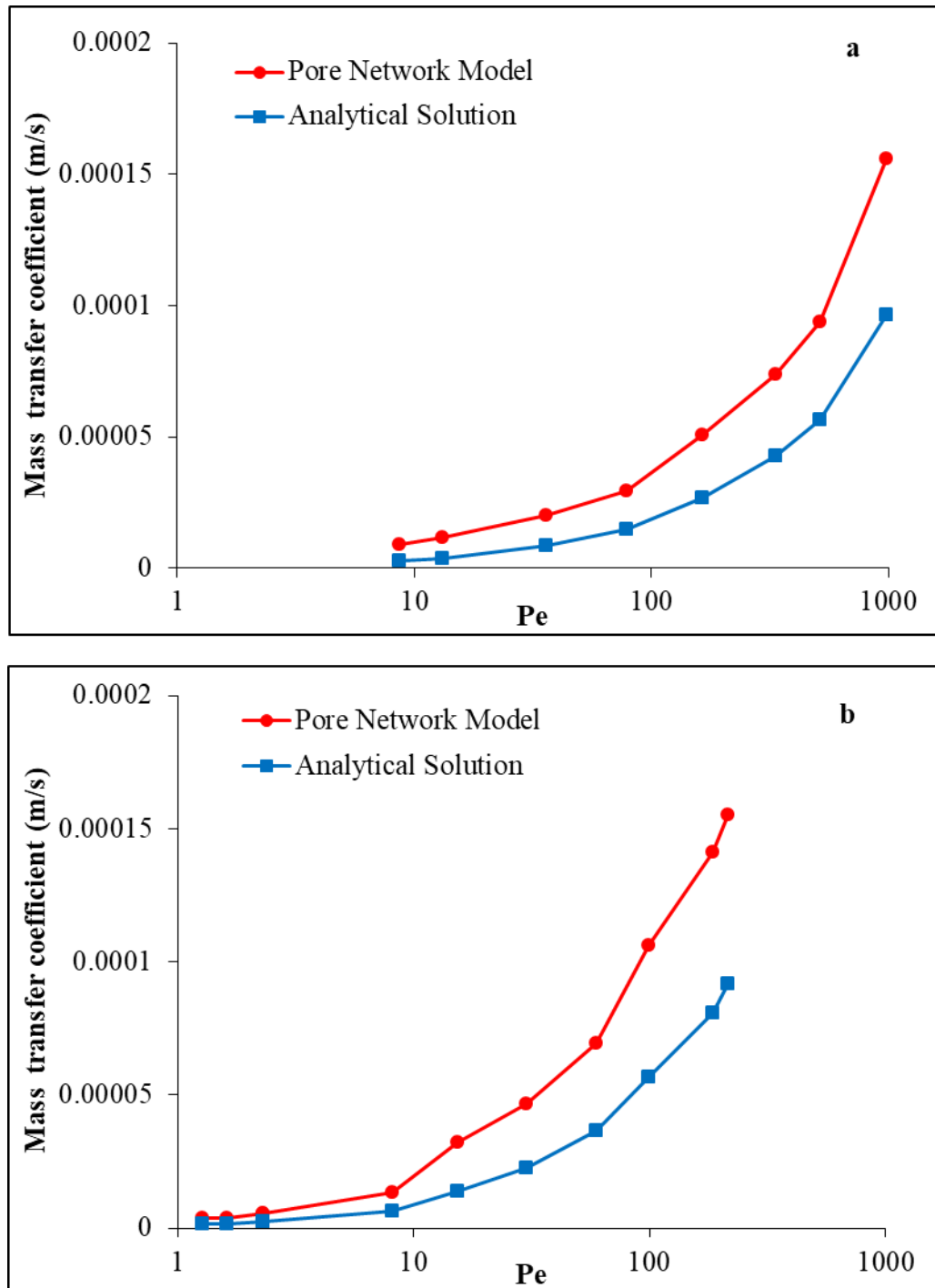


Figure 6.40. Comparison of the mass transfer coefficients determined with the analytical solution and the 2D pore network model for, a) glass beads, and b) sand.

Figure 6.40 also shows that the 1D solution which assumes a uniform concentration along the entire cross-section area of the flow cell can lead to the under estimation of the mass transfer coefficient. Even for the current experimental setup with a relatively small cross-sectional area, the 1D solution underestimates the mass transfer coefficient by a factor of about 1.6-3.2. This factor is highest at low velocities which corresponds to low lateral dispersion coefficients. This shows the significance of lateral transport on the estimation of the interphase mass transfer. Low lateral

dispersion is inconsistent with the underlying assumption of the 1D analysis, namely that the concentration distribution is uniform over the domain cross sectional area.

#### 6.4. Development of Sherwood Correlation

Sherwood correlations were developed for the sand and glass beads experiments using the interphase mass transfer coefficient determined from the pore network model. The developed Sherwood correlations, expressed in terms of the Peclet number, are presented in Figure 6.41. The same plot is also shown in Figure 6.42 with non-logarithmic vertical axis to better visualize the difference between the different models. The Pe numbers were calculated using the Equation 4.10. The corresponding best-fit Sherwood correlations are:

$$Sh = 2.36 Pe^{0.6} \text{ for glass beads (} d_m = 0.001 \text{ m)} \quad (6.1)$$

$$Sh = 0.606 Pe^{0.76} \text{ for sand (} d_m = 0.0002 \text{ m)} \quad (6.2)$$

The coefficient of determination of the above regression equations,  $R^2$ , for the sand and glass beads was 0.991 and 0.998, respectively, indicating a good fit between the developed correlations and the experimental data. For comparison Figure 6.41 and 6.42 also shows the data from Zilliox et al. (1973) and Hoffmann (1969) data for glass beads with  $d_m = 0.002$  m and  $d_m = 0.0005$  m respectively, and the Pfannkuch (1984) correlation. It is observed that the Pfannkuch (1984) correlation falls below both correlations given in Equations 6.1 and 6.2 although the grain diameters used in these experiments falls between those used in the current study. This suggests that the Pfannkuch correlation underestimates the mass transfer correlation by a factor of 2-3. As mentioned before, Pfannkuch correlation is associated with a high degree of uncertainty due to the lack of precise data to define some key parameters and because the estimation of the mass transfer coefficient using a 1D analytic solution that ignores the dissolved oil concentration along the flow cell. Using a higher solubility value as well as ignoring the dissolved concentration in the aqueous phase both can lead to the overestimation of the concentration difference term and underestimation of the mass transfer coefficient (Equation 2.1).

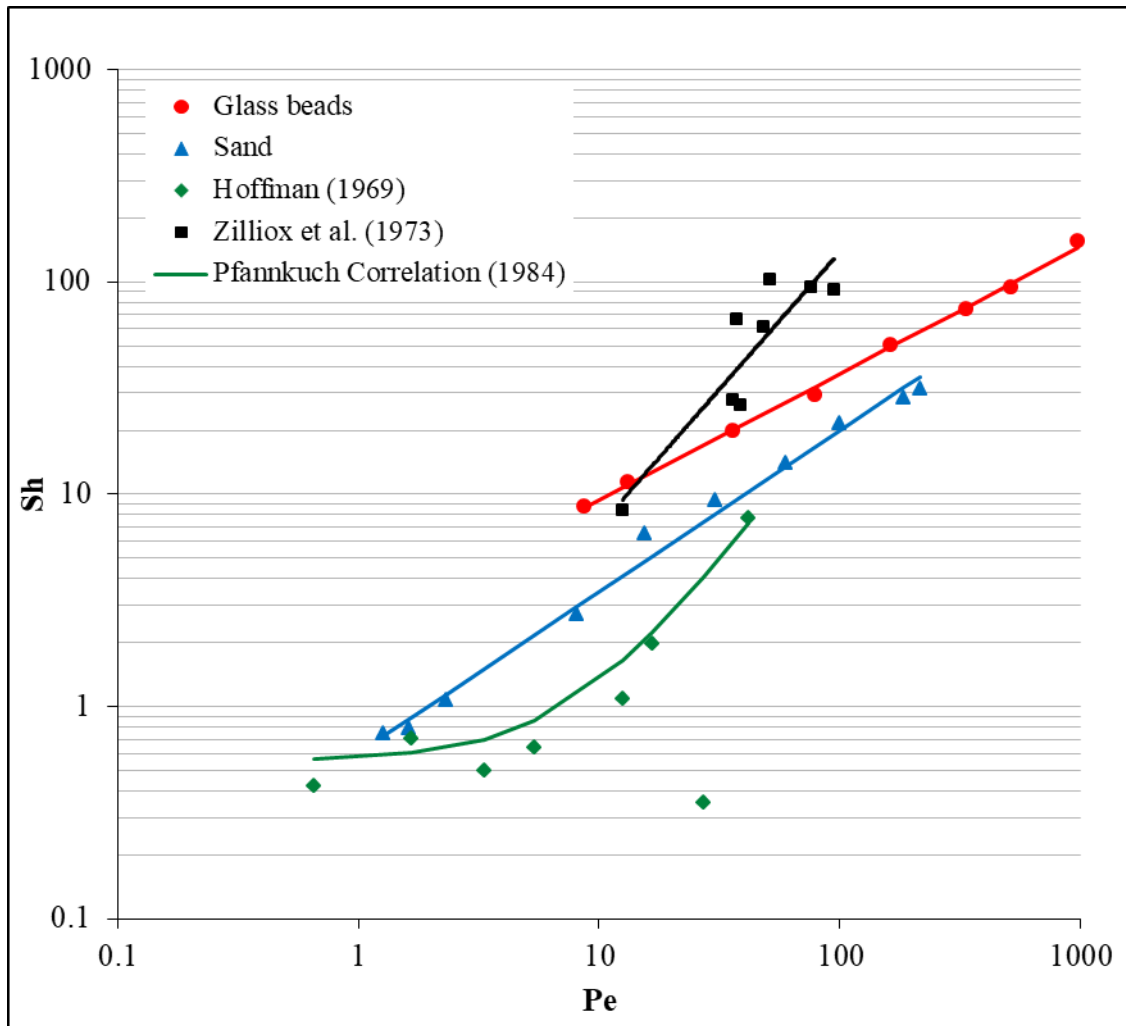


Figure 6.41. Sherwood calculations for glass beads ( $d_m = 0.001$  m) and sand ( $d_m = 0.0002$  m) and their best-fit correlations. For comparison the data from Zilliox et al. (1973) [glass beads with  $d_m = 0.002$  m], Hoffmann (1969) [glass beads with  $d_m = 0.0005$  m], and the Pfannkuch (1984) Sherwood correlation are also shown. A logarithmic scale is used for the vertical axis.

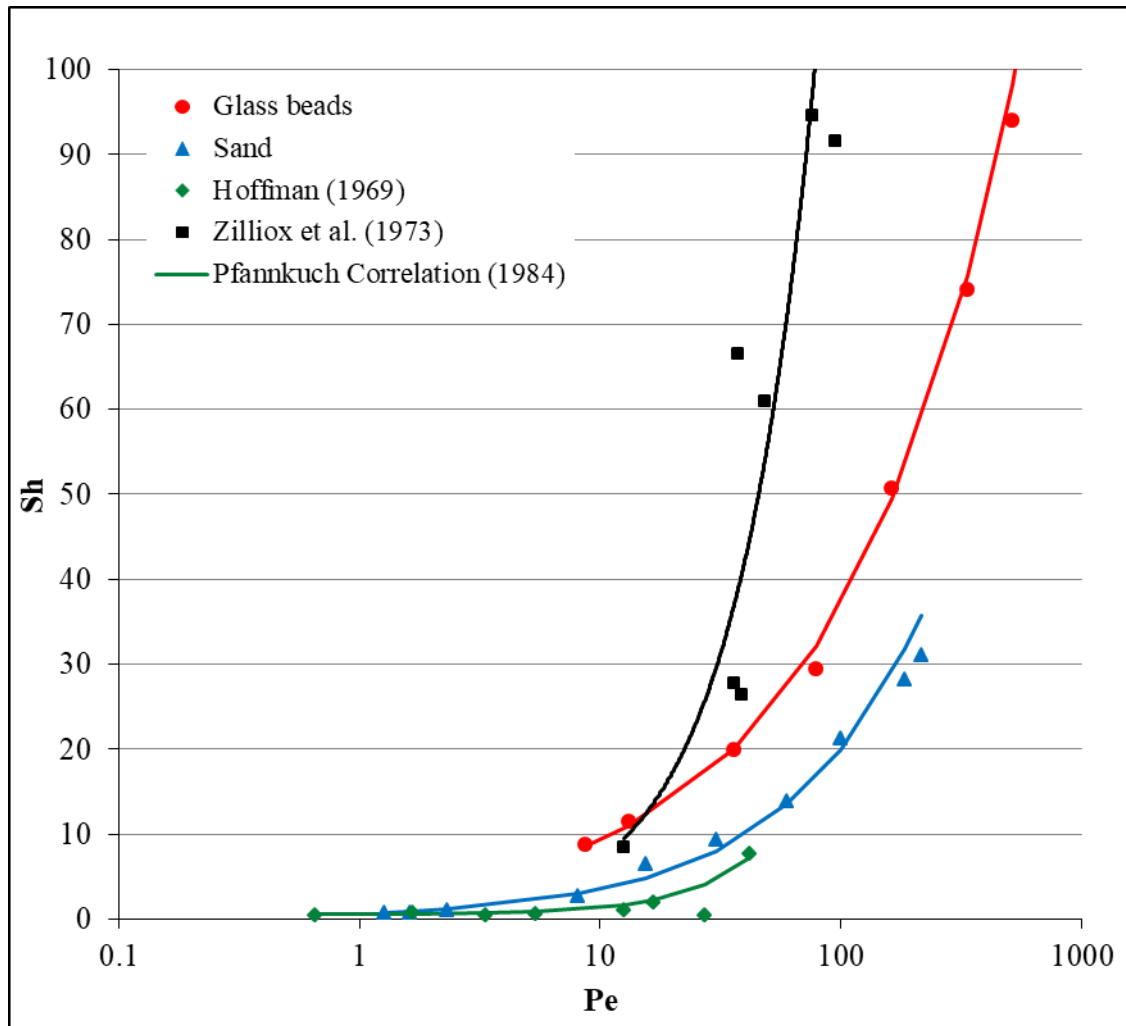


Figure 6.42. Sherwood calculations for glass beads ( $d_m = 0.001$  m) and sand ( $d_m = 0.0002$  m) and their best-fit correlations. For comparison the data from Zilliox et al. (1973) [glass beads with  $d_m = 0.002$  m], Hoffmann (1969) [glass beads with  $d_m = 0.0005$  m], and the Pfannkuch (1984) Sherwood correlation are also shown. A non-logarithmic scale is used for the vertical axis.

Another important difference between the two correlations is the exponent of the Pe term. The exponents of the Pe term determined in this study falls within the range of values reported in the literature (see for example Table 1 of Jia et al., 1999), albeit previous studies developed expressions for the lumped Sherwood number, not the explicit value. It is important to note that these values are significantly lower than the exponent of  $3/2$  determined by Pfannkuch (1984). As noted by Cussler (2009) the exponent is related to the NAPL configuration. A power greater than 1 is not consistent with the NAPL pool and flow configuration considered here. As the aqueous phase velocity increases, the volume of water contacting the NAPL per unit time increases proportionally. However, the contact time between the NAPL and flowing aqueous phase decreases with increase in the velocity. Overall, this means that the dissolution rate (or equally the mass transfer coefficient) is proportional to the velocity raised to a power that is less than unity.

## 7. CONCLUSION AND RECOMMENDATIONS

The accidental release of organic contaminants in the form of non-aqueous phase liquids (NAPLs) into the subsurface is a widespread and challenging environmental problem. Successful remediation of sites contaminated with NAPLs is essential for the protection of human health and the environment. Cosolvent flushing is one of the promising technologies often considered for the remediation of NAPL zones in the subsurface. The focus of this dissertation is to experimentally investigate the factors influencing the interphase mass transfer and to numerically model the enhanced dissolution of NAPLs due to cosolvent flushing. For this purpose, two sets of experiments were conducted and subsequently modelled numerically to gain further insight into the governing processes.

In the first set of experiments, batch tests and a series of cosolvent flushing experiments were conducted to evaluate the enhanced remediation of a DNAPL using an intermediate-scale tank with varying cosolvent contents, velocities and pumping patterns. The DNAPL selected for this purpose was TCE which is a widely observed chemical at groundwater contamination sites, while the cosolvent selected for this study was ethanol.

The batch tests were conducted to understand the characteristics of the multiphase (TCE-water-ethanol) system. The measured parameters were IFT, solubility and miscibility by TPDs as a function of ethanol content. The main findings of the batch tests are as follows:

- The IFT gradually decreased with increase in ethanol content of the flushing solution.
- The solubility of TCE increased rapidly with ethanol content up to 19,000 mg/L for ethanol contents of about 30% in the flushing solution.
- TPDs showed that the multiphase system is fully miscible at ethanol contents higher than 50%.

The results of the intermediate-scale tank experiments highlighted the importance of the flushing solution content, its velocity, and the flow patterns on the rate of DNAPL mass recovery from the subsurface. The following findings were observed from these experiments:

- For the low ethanol contents, the collected TCE mass was higher from the upper ports while the highest TCE mass recovery was achieved from lower ports for high ethanol contents.

- TCE mass recovery was found to be strongly dependent to the ethanol content of the flushing solution and its velocity.
- The cumulative TCE mass recovered was significantly higher for 50% ethanol content when compared to 0 and 20%.
- Since the TCE was partially bypassed by the flushing solution at the higher velocities, TCE recovery was lower.
- Intermittent flushing, which consist of repetitive cycles of injection of the flushing solution followed by periods of no flow, significantly enhanced the TCE mass recovery due to the increased contact time between the flushing solution and the entrapped DNAPL mass.
- The calculated trapping number suggests that TCE mobility did not occur in the tank system and that the resultant increase in TCE recovery is due to enhanced solubility.

The results of the intermediate-scale tank experiments were also simulated using a modified version of the UTCHEM multiphase flow simulator. The interphase mass transfer coefficient has proved to be a key parameter for the DNAPL mass recovery. This parameter generally cannot be directly measured and hence must be estimated by matching experimental data to model results. The main findings of this numerical investigation are listed below:

- Under conditions similar to those encountered in the field, the non-equilibrium assumption is usually more valid than the equilibrium condition, which tends to overestimate the NAPL recovery.
- A single mass transfer coefficient for the entire flushing period can overestimate the recovered NAPL mass. This could be attributed to the NAPL source bypassing phenomenon of the flushing solution that often results in a significant decrease in NAPL recovery compared to what is predicted by multiphase models, especially under high velocities.
- It was observed that the effluent concentrations and best-fit mass transfer coefficients are almost identical for two different TCE zones with the same spill volume but different NAPL zone size (3x3 vs. 5x5). This finding suggests that in some instances defining the correct DNAPL spill volume may be sufficient for accurately simulating the contamination transport problem.
- The estimated interphase mass transfer rate, expressed as a modified Sherwood number, obtained from the current study is about 10–200 times lower than the Sherwood values predicted in the literature for similar flow conditions. Whereas Sherwood correlations are generally developed for uniform NAPL distributions, the initial NAPL distributions of the current experiments closer to conditions that may be encountered in real NAPL

contamination settings. Reducing the size of the NAPL zone did not significantly alter the estimated mass transfer coefficients.

- The conducted experiments suggest that the interphase mass transfer coefficient is also a function of the cosolvent content.

Based on the experimental and the numerical work conducted in this study, future recommendations on cosolvent enhanced NAPL removal may focus on the issues below:

- The present flushing experiments were conducted considering a single NAPL. However, in real cases, mixed contaminants can be present in the field that would complicate the multiphase system and consequently affect the removal efficiency of the remediation process.
- The impact of multiple cosolvents on the performance of the flushing operation could be tested with further experiments. By using cosolvent mixtures, the synergetic benefits of using different cosolvents each with its own properties (density, viscosity, solubility enhancement) can be evaluated.
- The intermediate-scale cosolvent flushing were conducted with a fairly uniform sand. In reality, the soil in the subsurface is heterogeneous and the soil heterogeneity is a significant parameter that influences the NAPL removal.
- Future studies could consider the combination of cosolvent flushing with zero valent iron nanoparticles to reduce NAPLs in subsurface. The rapid degradation of dissolved NAPL with highly reactive nZVI may enhance the dissolution of NAPL and reduce the clean-up time.
- Cosolvent flushing could also be combined with in-situ chemical oxidation using permanganate or persulfate. It is hypothesized that the synergy obtained through the combination of these two technologies – enhanced dissolution and in-situ chemical oxidation – can lead to the more rapid and efficient remediation of groundwater systems contaminated with NAPLs.

The numerical interpretation conducted in this study demonstrates the complexity of modeling cosolvent enhanced NAPL remediation and underlines the significance of the interphase mass transfer for the accurate simulation and NAPL fate and transport. Therefore, the second part of this study focused on elucidating the factors influencing the interphase mass transport and to develop a fundamental generic expression for the interphase mass transfer that can be used in future modelling studies. For this purpose, a series of controlled dissolution experiments were conducted and a

NAPL dissolution computer program written in Fortran was developed for the interpretation of the experimental data.

The persistence of NAPLs entrapped in the subsurface is strongly controlled by their rate of dissolution into the groundwater. The interphase mass transfer coefficient needed to model the rate of dissolution is generally defined in terms of Sherwood correlations that are related to system properties. Such expressions are lacking because of the difficulty in estimating the interfacial area between phases. In fact, only two such correlations have been reported in the literature: the Powers et al. (1994b) correlation for the dissolution of sphere embedded in porous media and the Pfannkuch (1984) correlation for the dissolution from pooled-NAPL. The latter has been used in a number of subsequent studies although it is associated with a high level of uncertainty.

In the second part of the study, dissolution from pooled NAPL emplaced in porous media was investigated. This problem is commonly encountered in the field and similar to that considered by Hoffmann (1969) and Pfannkuch (1984). The idealized NAPL distribution (in the form of a pool) allows for the estimation of the contact area between the NAPL and aqueous phases. Controlled dissolution experiments were conducted for Pe numbers ranging from about 1 to 1000 and for two uniform porous media: glass beads with  $d_m = 0.001$  m and sand with  $d_m = 0.0002$  m. The interpretation of the dissolution experiments was performed using a 2D pore network model in addition to a simplified 1D analytical solution. The results of the dissolution experiments and the numerical interpretation are listed below:

- Since the contact time is shorter between NAPL and aqueous phase, effluent concentrations decreases as the velocity increases.
- As previous studies have also suggested, the mass transfer coefficient decreases with decrease in mean grain diameter.
- Although the cross sectional area of the flow cell used in this study is small, the effluent concentrations are lower than the solubility even for the lowest velocities. This provides further evidence for the presence of non-equilibrium conditions and the need for a rate-limited kinetic dissolution expression to accurately model the interphase mass transfer.
- The lateral transport influences the rate of dissolution and that the analytical solution which ignores the transport in the lateral direction under-estimates the interphase mass transfer coefficient. This shows the significance of lateral transport on the estimation of the interphase mass transfer.

The main contribution of this part is a revised Sherwood expression as a function of Peclet number for pooled NAPL. As noted previously, the Pfannkuch, (1984) correlation and the Hoffmann, (1969) data used in the development of the correlation were not intended to be used as predictive tool for the estimation of rate-limited interphase mass transfer due to a number of uncertainties. Many of these uncertainties have been addressed and therefore the Sherwood expressions developed in this study are more suitable for use in future studies such as the thermodynamics-based approach that has been recently proposed (Grant and Gerhard, 2007a; Kokkinaki et al., 2013a, 2013b) as well as other modeling studies requiring an expression of the non-lumped Sherwood correlation.

Both set of experiments and modelling results showed that more effort is needed to further enhance our knowledge of the interphase mass transfer. Future research in this area may be directed to the following issues:

- Since accurate determination of the interfacial area is a major limitation, innovative imaging techniques could be used to estimate more accurately pore space geometry and contact area between the phases. With such advanced imaging technologies, it is possible to extend the current work to other NAPL configurations besides the pooled NAPL considered in this study.
- Interphase mass transfer is influenced by a number of parameters in a complex manner. In the scope of this dissertation, the effect of the flow velocity and grain size diameter of the porous media on mass transfer was investigated. Beside these parameters, the impact of wettability, ionic strength and temperature could be considered in future studies.
- The intermediate-scale experiments suggest that the interphase mass transfer coefficient is also a function of the cosolvent content. This parameter has been generally overlooked in the development of Sherwood correlations. Further systematic experiments are needed to confirm this observation.

The experimental investigations and modeling work conducted in this study demonstrate the complexity of the NAPL groundwater contamination problem and the need to continue efforts for the development of effective and cost-efficient remediation technologies. The ultimate test is to demonstrate the effectiveness of such remediation technologies to real-life problems and the associated complexities encountered at the field scale.

## REFERENCES

- Abriola, L. M., Drummond, C. D., Hahn, E. J., Hayes, K. F., Kibbey, T.C.G., Lemke, L. D., 2005. Pilot-scale demonstration of surfactant-enhanced PCE solubilization at the Bachman Road site. 1. Site characterization and test design. *Environmental Science and Technology*, 39, 1778-1790.
- Agaoglu, B., Scheytt, T., Coptý, N. K., 2012. Laboratory Scale Experiments and Numerical Modeling of Cosolvent flushing of Multi-component NAPLs in Saturated Porous Media. *Journal of Contaminant Hydrology*. *Journal of Contaminant Hydrology*, 140, 80-94.
- Agaoglu, B., Coptý, N. K., Scheytt, T., Hinkelmann, R., 2015. Interphase mass transfer between fluids in subsurface formations: a review. *Advances in Water Resources*, 79, 162-194.
- Agaoglu, B., Scheytt, T., Coptý, N. K., 2016. Impact of NAPL architecture on interphase mass transfer: A pore network study. *Advances in Water Resources*, 95, 138-151.
- Akyol, N.H. and Turkkan, S., 2018. Effect of Cyclodextrin-Enhanced Dissolution on Mass Removal and Mass-Flux Reduction Relationships for Non-uniformly Organic Liquid Distribution in Heterogeneous Porous Media. *Water, Air, and Soil Pollution*, 229, 30.
- Akyol, N. H., Yolcubal, I., Yüksel, D. I., 2011. Sorption and transport of trichloroethylene in caliche soil. *Chemosphere*, 82, 809-816.
- Akyol, N.H., Yolcubal, I., 2013. Oxidation of nonaqueous phase trichloroethylene with permanganate in epikarst. *Water, Air, and Soil Pollution*, 224, 1573.
- Anwar, A. F., Tien, T. H., Inoue, Y., Takagi, F., 2003. Mass transfer correlation for nonaqueous phase liquid volatilization in porous media. *Environmental Science and Technology*, 37, 1277-1283.
- Aydin-Sarikurt, D., Dokou, Z., Coptý, N. K., Karatzas, G. P., 2016. Experimental Investigation and Numerical Modeling of Enhanced DNAPL Solubilization in Saturated Porous Media. *Water, Air, and Soil Pollution*, 227, 441.

Banerjee, S., Yalkowsky, S. H., Valvani, S. C., 1980. Water solubility and octanol/water partition coefficients of organics. Limitations of the solubility-partition coefficient correlation. *Environmental Science and Technology*, 14, 1227-1229.

Berge, N. D., Ramsburg, C. A., 2010. Iron-mediated trichloroethene reduction within nonaqueous phase liquid. *Journal of Contaminant Hydrology*, 118, 105-116.

Brooks, R. H., Corey, A. T., 1966. Properties of porous media affecting fluid flow. *Journal of the Irrigation and Drainage Division*, 92, 61-90.

Brooks, M. C., Annable, M. D., Rao, P. S. C., Hatfield, K., Jawitz, J. W., Wise, W. R., Wood, A. L., Enfield, C.G., 2004. Controlled release, blind test of DNAPL remediation by ethanol flushing. *Journal of Contaminant Hydrology*, 69, 281-297.

Brusseau, M. L., Zhang, Z., Nelson, N. T., Cain, R. B., Tick, G. R., Oostrom, M., 2002. Dissolution of nonuniformly distributed immiscible liquid: intermediate-scale experiments and mathematical modeling. *Environmental Science and Technology*, 36, 1033-1041.

Brusseau, M.L., Carroll, K.C., Allen, T., Baker, J., DiGuseppi, W., Hatton, J., Morrison, C., Russo, A., Berkompas, J., 2011. Impact of in situ chemical oxidation on contaminant mass discharge: linking source-zone and plume-scale characterizations of remediation performance. *Environmental Science and Technology*, 45, 5352-5358.

Childs, J., Acosta, E., Annable, M. D., Brooks, M. C., Enfield, C. G., Harwell, J. H., Shiau, B. 2006. Field demonstration of surfactant-enhanced solubilization of DNAPL at Dover Air Force Base, Delaware. *Journal of Contaminant Hydrology*, 82, 1-22.

Christ, J. A., Lemke, L. D., Abriola, L. M., 2005. Comparison of two-dimensional and three-dimensional simulations of dense nonaqueous phase liquids (DNAPLs): Migration and entrapment in a nonuniform permeability field. *Water Resources Research*, 41.

Cohen, R. M., Mercer, J. W., 1993. DNAPL Site Evaluation, C. K. Smoley. CRC Press, Boca Raton, Florida.

Cussler, E. L., 2009. Diffusion: Mass Transfer in Fluid Systems, Third Ed., Cambridge University Press, Cambridge U.K.

Davis, E. L., 1997. Ground Water Issue: How Heat Can Enhance In-Situ Soil and Aquifer Remediation: Important Chemical Properties and Guidance on Choosing the Appropriate Technique. US Environmental Protection Agency, Center for Environmental Research Information. USA.

Delshad, M., Pope, G. A., Sepehrnoori, K., 1996. A compositional simulator for modeling surfactant enhanced aquifer remediation, 1 formulation. Journal of Contaminant Hydrology, 23, 303-327.

Dillard, L. A., Blunt, M. J., 2000. Development of a pore network simulation model to study nonaqueous phase liquid dissolution. Water Resources Research, 36, 439-454.

Eberhardt, C., Grathwohl, P., 2002. Time scales of organic contaminant dissolution from complex source zones: Coal tar pools vs. blobs. Journal of Contaminant Hydrology, 59, 45-66.

Eichel, H., Helmig, R., Neuweiler, I., Cirpka, O. A., 2005. Upscaling of two-phase flow processes in porous media. In Das, D. B., Hassanizadeh, S. M. (Eds.), Upscaling multiphase flow in porous media, 237-257, Springer, Netherlands.

Fagerlund, F., Illangasekare, T. H., Phenrat, T., Kim, H. J., Lowry, G. V., 2012. PCE dissolution and simultaneous dechlorination by nanoscale zero-valent iron particles in a DNAPL source zone. Journal of Contaminant Hydrology, 131, 9-28.

Fetter, C. W., 1999. Contaminant Hydrogeology, Prentice Hall, New Jersey, USA.

Fortin, J., Jury, W. A., Anderson, M. A., 1997. Enhanced removal of trapped non-aqueous phase liquids from saturated soil using surfactant solutions. Journal of Contaminant Hydrology, 24, 247-267.

Gabler, T., Paschke, A., Schüürmann, G., 1996. Diffusion coefficients of substituted benzenes at high dilution in water. Journal of Chemical and Engineering Data, 41, 33-36.

Giese, S. W., Powers, S. E., 2002. Using polymer solutions to enhance recovery of mobile coal tar and creosote DNAPLs. *Journal of Contaminant Hydrology*, 58, 147-167.

Gillham, R. W., O'Hannesin, S. F., 1994. Enhanced degradation of halogenated aliphatics by zero-valent iron. *Ground Water*, 32, 958-967.

Grant, G. P., Gerhard, J.I., 2007a. Simulating the dissolution of a complex dense nonaqueous phase liquid source zone: 1. Model to predict interfacial area. *Water Resources Research*, 43.

Grant, G. P., Gerhard, J. I., 2007b. Simulating the dissolution of a complex dense nonaqueous phase liquid source zone: 2. Experimental validation of an interfacial areabased mass transfer model. *Water Resources Research*, 43.

Grubb, D. G., Sitar, N., 1994. Evaluation of technologies for in-situ cleanup of DNAPL contaminated sites. Robert S. Kerr Environmental Research Laboratory, Office of Research and Development, US Environmental Protection Agency. USA.

Guilbeault, M. A., Parker, B. L., Cherry, J. A., 2005. Mass and flux distributions from DNAPL zones in sandy aquifers. *Ground Water*, 43, 70-86.

Hand, D. B., 1939. Dimeric distribution: I. The distribution of a consolute liquid between two immiscible liquids. *Journal of Physics and Chemistry*, 34, 1961-2000.

Held, R. J., Celia, M.A., 2001. Pore-scale modeling and upscaling of nonaqueous phase liquid mass transfer. *Water Resources Research*, 37, 539-549.

Hirasaki, G. J., Jackson, R. E., Jin, M., Lawson, J. B., Londergan, J., Meinardus, H., Miller, C. A., Pope, G. A., Szafranski, R., Tanzil, D., Annable, M.D., 2000. Field demonstration of the surfactant/foam process for remediation of a heterogeneous aquifer contaminated with DNAPL. *NAPL Removal: Surfactants, Foams, and Microemulsions*, 3-163.

Hoffmann, B., 1969. Über die ausbreitung gelöster kohlenwasserstoffe im grundwasserleiter. Inst F Wasserwirtschaft U Landwirtschaftl Wasserbau D Techn Univ.

Hoffman, F., 1993. Ground-water remediation using "Smart Pump and Treat". *Groundwater*, 31, 98-106.

Hofstee, C., Gutiérrez Ziegler, C., Trötschler, O., Braun, J., 2003. Removal of DNAPL contamination from the saturated zone by the combined effect of vertical upward flushing and density reduction. *Journal of Contaminant Hydrology*, 67, 61-78.

Hu, L. M., Meegoda, J. N., Lo, I. M., Liu, Y., Gao, S. Y., Wu, Z. Q., 2010. Gasoline Contaminated Sites: Pollutant Transport and Remediation, *Advances in Environmental Geotechnics*, Springer, Berlin Heidelberg, 221-235.

Hyman, M., Dupont, R. R., 2001. *Groundwater and soil remediation*. ASCE Press.

Huling, S. G. Weaver, J.W., 1991. Dense nonaqueous phase liquids. Superfund Technology Support Center for Ground Water, Robert S. Kerr Environmental Research Laboratory. USA.

Imhoff, P. T., Jaffé, P. R., Pinder, G. F., 1994. An experimental study of complete dissolution of a nonaqueous phase liquid in saturated porous media. *Water Resources Research*, 30, 307-320.

Imhoff, P.T., Gleyzer, S.N., McBride, J.F., Vancho, L.A., Okuda, I., Miller, C.T., 1995. Cosolvent enhanced remediation of residual dense nonaqueous phase liquids: experimental investigation. *Environmental Science and Technology*, 29, 1966-1976.

Imhoff, P. T., Miller, C. T., 1996. Dissolution fingering during the solubilization of nonaqueous phase liquids in saturated porous media: 1. Model predictions. *Water Resources Research*, 32, 1919-1928.

Illangasekare, T. H., Armbruster III, E. J., Yates, D. N., 1995. Non-aqueous-phase fluids in heterogeneous aquifers-Experimental study. *Journal of Environmental Engineering*, 121, 571-579.

Jawitz, J. W., Sillan, R. K., Annable, M. D., Rao, P. S. C., Warner, K., 2000. In-situ alcohol flushing of a DNAPL source zone at a dry cleaner site. *Environmental Science and Technology*, 34, 3722-3729.

Jia, C., Shing, K., Yortsos, Y.C., 1999. Visualization and simulation of non-aqueous phase liquids solubilization in pore networks. *Journal of Contaminant Hydrology*, 35, 363-387.

Joekar-Niasar, V., Hassanizadeh, S.M., 2012. Analysis of fundamentals of two-phase flow in porous media using dynamic pore-network models: a review. *Critical Reviews in Environmental Science and Technology*, 42, 1895-1976.

Johnson, R. L., and Pankow, J. F., 1992. Dissolution of dense chlorinated solvents into groundwater. 2. Source functions for pools of solvent. *Environmental Science and Technology*, 26, 896-901.

Johnson, W. P., John, W. W., 1999. PCE Solubilization and Mobilization by Commercial Humic Acid. *Journal of Contaminant Hydrology*, 35, 343-362.

Kavanaugh MC, Suresh P, Rao C., 2003. The DNAPL remediation challenge: Is there a case for source depletion?, Environmental Protection Agency, Washington DC, USA.

Keely, J. F., Boulding, J. R., 1989. Performance evaluations of pump-and-treat remediations, EPA Environmental Engineering Sourcebook, CRC Press, Washington DC, USA.

Kennedy, C. A., Lennox, W. C., 1997. A pore-scale investigation of mass transport from dissolving DNAPL droplets. *Journal of Contaminant Hydrology*, 24, 221-246.

Kokkinaki, A., O'Carroll, D. M., Werth, C. J., Sleep, B. E., 2013a. An evaluation of Sherwood–Gilland models for NAPL dissolution and their relationship to soil properties. *Journal of Contaminant Hydrology*, 155, 87-98.

Kokkinaki, A., O'Carroll, D. M., Werth, C. J., Sleep, B. E., 2013b. Coupled simulation of DNAPL infiltration and dissolution in three-dimensional heterogeneous domains: process model validation. *Water Resources Research*, 49, 7023-7036.

Krembs, F. J., 2008. Critical analysis of the field scale application of in situ chemical oxidation for the remediation of contaminated groundwater, Ph.D. Thesis, Colorado School of Mines.

- Kumar, M. A., Bae, S., Han, S., Chang, Y., Lee, W., 2017. Reductive dechlorination of trichloroethylene by polyvinylpyrrolidone stabilized nanoscale zerovalent iron particles with Ni. *Journal of Hazardous Materials*, 340, 399-406.
- Lenormand, R., Touboul, E., Zarcone, C., 1988. Numerical models and experiments on immiscible displacements in porous media. *Journal of Fluid Mechanics*, 189, 165.
- Li, B., Fu, J., 1992. Interfacial tensions of two-liquid-phase ternary systems. *Journal of Chemical and Engineering Data*, 37, 172-174.
- Liang, H., Falta, R. W., 2008. Modeling field-scale cosolvent flooding for DNAPL source zone remediation. *Journal of Contaminant Hydrology*, 96, 1-16.
- Lien, H. L., Wilkin, R. T., 2005. High-level arsenite removal from groundwater by zero-valent iron. *Chemosphere*, 59, 377-386.
- Liu, Y., Majetich, S. A., Tilton, R. D., Sholl, D. S., Lowry, G. V., 2005. TCE dechlorination rates, pathways, and efficiency of nanoscale iron particles with different properties. *Environmental Science and Technology*, 39, 1338-1345.
- Lowe, D. F., Oubre, C. L., Ward, C. H., Simpkin, T. J., 1999. *Surfactants and cosolvents for NAPL remediation: A technology practices manual (Vol. 1)*, CRC Press, USA.
- Luciano, A., Viotti, P., Papini, M. P., 2010. Laboratory investigation of DNAPL migration in porous media. *Journal of Hazardous Materials*, 176, 1006-1017.
- Lunn, S. R., Kueper, B. H., 1997. Removal of pooled dense, nonaqueous phase liquid from saturated porous media using upward gradient alcohol floods. *Water Resources Research*, 33, 2207-2219.
- Lunn, S. R., Kueper, B. H., 1999. Manipulation of density and viscosity for the optimization of DNAPL recovery by alcohol flooding. *Journal of Contaminant Hydrology*, 38, 427-445.

- Marble, J. C., DiFilippo, E. L., Zhang, Z., Tick, G. R., Brusseau, M. L., 2008. Application of a lumped-process mathematical model to dissolution of non-uniformly distributed immiscible liquid in heterogeneous porous media. *Journal of Contaminant Hydrology*, 100, 1-10.
- Martel, R., Gelinat, P. J., Desnoyers, J. E., 1998. Aquifer washing by micellar solutions: 1. Optimization of alcohol-surfactant-solvent solutions. *Journal of Contaminant Hydrology*, 29, 319-346.
- Mackay, D. M., Cherry, J. A., 1989. Groundwater contamination: Pump-and-treat remediation. *Environmental Science and Technology*, 23, 630-636.
- Maji, R., Sudicky, E. A., 2008. Influence of mass transfer characteristics for DNAPL source depletion and contaminant flux in a highly characterized glaciofluvial aquifer. *Journal of Contaminant Hydrology*, 102, 105-119.
- McKnight, U. S., Funder, S. G., Rasmussen, J. J., Finkel, M., Binning, P. J., Bjerg, P. L., 2010. An integrated model for assessing the risk of TCE groundwater contamination to human receptors and surface water ecosystems. *Ecological Engineering*, 36, 1126-1137.
- Mercer, J. W., Cohen, R. M., 1990. A review of immiscible fluids in the subsurface: Properties, models, characterization and remediation. *Journal of Contaminant Hydrology*, 6, 107-163.
- Miller, C. T., Poirier-McNeill, M. M., Mayer, A. S., 1990. Dissolution of trapped nonaqueous phase liquids: mass transfer characteristics. *Water Resources Research*, 26, 2783-2796.
- Mulligan, C. N., Yong, R. N., Gibbs, B. F., 2001. Surfactant-enhanced remediation of contaminated soil: a review. *Engineering Geology*, 60, 371-380.
- Nambi, I. M., Powers, S. E., 2000. NAPL dissolution in heterogeneous systems: an experimental investigation in a simple heterogeneous system. *Journal of Contaminant Hydrology*, 44, 161-184
- Nambi, I. M., Powers, S. E., 2003. Mass transfer correlations for nonaqueous phase liquid dissolution from regions with high initial saturations. *Water Resources Research*, 39.

Okuda, I., McBride, J. F., Gleyzer, S. N., Miller, C. T., 1996. Physicochemical transport processes affecting the removal of residual DNAPL by nonionic surfactant solutions. *Environmental Science and Technology*, 30, 1852-1860.

Oostrom, M., Dane, J. H., Wietsma, T. W., 2006. A review of multidimensional, multifluid intermediate-scale experiments. *Vadose Zone Journal*, 5, 570-598.

Pacwa-Płociniczak, M., Płaza, G.A., Piotrowska-Seget, Z., Cameotra, S.S., 2011. Environmental applications of biosurfactants: recent advances. *International Journal of Molecular Sciences*, 12, 633-654.

Pankow, J. F., Cherry, J. A., 1996. Dense chlorinated solvents and other DNAPLs in groundwater, Waterloo Press, Portland, OR, USA.

Park, E., Parker, J. C., 2005. Evaluation of an upscaled model for DNAPL dissolution kinetics in heterogeneous aquifers. *Advances in Water Resources*, 28, 1280-1291.

Parker, J. C., Park, E., 2004. Modeling field-scale dense nonaqueous phase liquid dissolution kinetics in heterogeneous aquifers. *Water Resources Research*, 40.

Pennell, K. D., Pope, G. A., Abriola, L. M., 1996. Influence of viscous and buoyancy forces on the mobilization of residual tetrachloroethylene during surfactant flushing. *Environmental Science and Technology*, 30, 1328-1335.

Pfannkuch, H. O., 1984. Determination of the contaminant source strength from mass exchange processes at the petroleum-ground-water interface in shallow aquifer systems. *Proceedings of the NWWA/API Conference Petroleum Hydrocarbons and Organic Chemicals in Ground Water: Prevention, Detection, and Restoration*, Houston, Texas, 13-15 November 1984, 5-7.

Phenrat, T., Fagerlund, F., Illangasekare, T., Lowry, G. V., Tilton, R. D., 2011. Polymer-modified Fe<sup>0</sup> nanoparticles target entrapped NAPL in two dimensional porous media: effect of particle concentration, NAPL saturation, and injection strategy. *Environmental Science and Technology*, 45, 6102-6109.

- Phenrat, T., Thongboot, T., Lowry, G. V., 2015. Electromagnetic induction of zerovalent iron (ZVI) powder and nanoscale zerovalent iron (NZVI) particles enhances dechlorination of trichloroethylene in contaminated groundwater and soil: proof of concept. *Environmental Science and Technology*, 50, 872-880.
- Pope, G. A., Nelson, R. C., 1978. A chemical flooding compositional simulator. *Society of Petroleum Engineers Journal*, 18, 339-354.
- Powers, S. E., Abriola, L. M., Weber, W. J., 1992. An experimental investigation of nonaqueous phase liquid dissolution in saturated subsurface systems: Steady state mass transfer rates. *Water Resources Research*, 28, 2691-2705.
- Powers, S. E., Abriola, L. M., Dunkin, J. S., Weber, W. J., 1994a. Phenomenological models for transient NAPL-water mass-transfer processes. *Journal of Contaminant Hydrology*, 16, 1-33.
- Powers, S. E., Abriola, L. M., Weber, W. J., 1994b. An experimental investigation of nonaqueous phase liquid dissolution in saturated subsurface systems: Transient mass transfer rates. *Water Resources Research*, 30, 321-332.
- Puls, R.W., Paul, C. J., Powell, R.M., 1999. The application of in situ permeable reactive (zero valent iron) barrier technology for the remediation of chromate-contaminated groundwater: a field test. *Applied Geochemistry*, 14, 989-1000.
- Ramsburg, C. A., Pennell, K. D., 2002. Density-modified displacement for DNAPL source zone remediation: density conversion and recovery in heterogeneous aquifer cells. *Environmental Science and Technology*, 36, 3176-3187.
- Roeder, E., Falta, R.W., 2001. Modeling unstable alcohol flooding of DNAPL-contaminated columns. *Advances in Water Resources*, 24, 803-819.
- Saba, T., Illangasekare, T. H., 2000. Effect of groundwater flow dimensionality on mass transfer from entrapped nonaqueous phase liquid contaminants. *Water Resources Research*, 36, 971-979.

Saba, T., Illangasekare, T. H., Ewing, J., 2001. Investigation of surfactant-enhanced dissolution of entrapped nonaqueous phase liquid chemicals in a two-dimensional groundwater flow field. *Journal of Contaminant Hydrology*, 51, 63-82.

Sabatini, D. A., Knox, R. C., Harwell, J. H., Wu, B., 2000. Integrated design of surfactant enhanced DNAPL remediation: efficient supersolubilization and gradient systems. *Journal of Contaminant Hydrology*, 45, 99-121.

Salanitro, J. P., Johnson, P. C., Spinnler, G. E., Maner, P. M., Wisniewski, H. L., Bruce, C., 2000. Field-scale demonstration of enhanced MTBE bioremediation through aquifer bioaugmentation and oxygenation. *Environmental Science and Technology*, 34, 4152-4162.

Saleh, N., Sirk, K., Liu, Y., Phenrat, T., Dufour, B., Matyjaszewski, K., Lowry, G. V., 2007. Surface modifications enhance nanoiron transport and NAPL targeting in saturated porous media. *Environmental Engineering Science*, 24, 45-57.

Sarikurt, D. A., Gokdemir, C., Coptu, N. K., 2017. Sherwood correlation for dissolution of pooled NAPL in porous media. *Journal of Contaminant Hydrology*, 206, 67-74.

Schnaar, G., Brusseau, M.L., 2006. Characterizing pore-scale dissolution of organic immiscible liquid in natural porous media using synchrotron X-ray microtomography. *Environmental Science and Technology*. 40, 6622-6629.

Shiau, B. J., Sabatini, D. A., Harwell, J. H., 1995. Properties of food grade (edible) surfactants affecting subsurface remediation of chlorinated solvents. *Environmental Science and Technology*, 29, 2929-2935.

Siegrist, R. L., Crimi, M., Simpkin, T. J. (Eds.), 2011. *In situ chemical oxidation for groundwater remediation (Vol. 3)*. Springer Science and Business Media, U.S.A.

Silva, R.D.C.F., Almeida, D.G., Rufino, R.D., Luna, J.M., Santos, V.A., Sarubbo, L.A., 2014. Applications of biosurfactants in the petroleum industry and the remediation of oil spills. *International Journal of Molecular Sciences*, 15, 12523-12542.

Soga, K., Page, J. W. E., Illangasekare, T. H., 2004. A review of NAPL source zone remediation efficiency and the mass flux approach. *Journal of Hazardous Materials*, 110, 13- 27.

St-Pierre, C., Martel, R. Gabriel, U., Lefebvre, R., Robert, T, Hawari, J., 2004. TCE recovery mechanisms using micellar and alcohol solutions: phase diagrams and sand column experiments, *Journal of Contaminant Hydrology*, 71, 155-192.

Stroo, H. F., Unger, M., Ward, C. H., Kavanaugh, M. C., Vogel, C., Leeson, A., 2003. Remediating chlorinated solvent source zones. *Environmental Science and Technology*, 37, 224A-230A.

Stroo, H. F., Ward, C. H. (Eds.), 2010. *In situ remediation of chlorinated solvent plumes*. Springer Science and Business Media, U.S.A.

Tick, G. R., Lourenso, F., Wood, A. L., Brusseau, M. L., 2003. Pilot-scale demonstration of cyclodextrin as a solubility-enhancement agent for remediation of a tetrachloroethene-contaminated aquifer. *Environmental science and Technology*, 37, 5829-5834.

U.S.EPA., 1995. *Subsurface Volatilization and Ventilation System (SVVS) TM*, Innovative Technology Evaluation Report, EPA/540/R-94/529. August.

U.S.EPA., 2004. *Cleaning up the nation's waste sites: markets and technology trends*. Washington, DC. EPA/542/R-04/015. April.

Van Valkenburg, M. E., Annable, M. D., 2002. Mobilization and entry of DNAPL pools into finer sand media by cosolvents: two-dimensional chamber studies. *Journal of Contaminant Hydrology*, 59, 211-230.

Waduge, W. A. P., Soga, K., Kawabata, J., 2004. Effect of NAPL entrapment conditions on air sparging remediation efficiency. *Journal of hazardous materials*, 110, 173-183.

Wang, X., Brusseau, M. L., 1993. Solubilization of some low-polarity organic compounds by hydroxypropyl- $\beta$ -cyclodextrin. *Environmental Science and Technology*, 27, 2821-2825.

Wang, C. B., Zhang, W. X., 1997. Synthesizing nanoscale iron particles for rapid and complete dechlorination of TCE and PCBs. *Environmental Science and Technology*, 31, 2154-2156.

Wang, Q., Jeong, S. W., Choi, H., 2012. Removal of trichloroethylene DNAPL trapped in porous media using nanoscale zerovalent iron and bimetallic nanoparticles: Direct observation and quantification. *Journal of Hazardous Materials*, 213, 299-310.

West, C. C., Harwell, J. H., 1992. Surfactants and subsurface remediation. *Environmental Science and Technology*, 26, 2324-2330.

Wu, L., Ritchie, S. M., 2006. Removal of trichloroethylene from water by cellulose acetate supported bimetallic Ni/Fe nanoparticles. *Chemosphere*, 63, 285-292.

Vogan, J. L., Focht, R. M., Clark, D. K., Graham, S. L., 1999. Performance evaluation of a permeable reactive barrier for remediation of dissolved chlorinated solvents in groundwater. *Journal of Hazardous Materials*, 68, 97-108.

Yak, H. K., Lang, Q., Wai, C. M., 2000. Relative resistance of positional isomers of polychlorinated biphenyls toward reductive dechlorination by zerovalent iron in subcritical water. *Environmental Science and Technology*, 34, 2792-2798.

Yin, Y., Allen, H. E., 1999. In situ chemical treatment. Technology evaluation report, Ground-Water Remediation Technologies Analysis Center, Pittsburgh, PA, USA.

Zhang, C., Werth, C. J., Webb, A. G., 2002. A magnetic resonance imaging study of dense nonaqueous phase liquid dissolution from angular porous media. *Environmental Science and Technology*, 36, 3310-3317.

Zilliox, L., Muntzer, P., Menanteau, J. J., 1973. Probleme de l'echange entre un produit petrolier immobile et l'eau en mouvement dans un milieu poreux. *Revue de l'Institut Frabcais du Petrole*, 28, 185-200.

## APPENDIX A: PORE NETWORK FORTRAN CODE FOR FLOW CELL FILLED WITH GLASS BEADS

```

c 2D mass transport model to determine the mass transfer coefficient
c May 2017
c length of tank is 100 mm, height is 40 -10 =30 mm
c C matrix is the concentration at the current time step
cunits are in: g, m, s
implicit double precision (a-h,o-z)
parameter (nx0=102, ny0=30,nexp0=1,niter0=600000,tol=1.e-08)
dimension vel(nexp0),q(nexp0),Dx(nexp0),Dy(nexp0),xk(nexp0)
dimension caver(nexp0,niter0)
dimension c(nx0,ny0),cold(nx0,ny0)
    open(3,file='conc.out',status='unknown')
    open(4,file='tempH.out',status='unknown')
    open(5,file='tempV.out',status='unknown')
    open(6,file='glassbeadsQ8.dat',status='unknown')
c define input data
    deltaT=0.03
    grain=0.001
    vol=(grain*0.7)**3
    atube=(grain*0.5)**2
    xl=grain*0.3
    area= 0.04*0.03
    por= 0.34
    dm=1.e-9
    cset alpha to 0.002 m from tracer tests
    alphaL=0.002
    alphaT=0.002
    Csol=156.
c define flow rate as ml/min
c q(1)=0.213
c q(2)=0.324
c q(3)=0.885
c q(4)=1.935

```

```

c  q(5)=4.
c  q(6)=8.182
c  q(7)=12.632
    q(1)=24.
do 10 nexp=1,nexp0
c  convert flow rate to units of m^3/s
q(nexp)=q(nexp)*1.e-06/60.
qtube=q(nexp)/float(40*30)
    vel(nexp)=q(nexp)/area/por
    Dx(nexp)=alphaL*vel(nexp)+dm
    Dy(nexp)=alphaT*vel(nexp)+dm
c  xk(1)=8.77e-06
c  xk(2)=1.14e-05
c  xk(3)=1.99e-05
c  xk(4)=2.94e-05
c  xk(5)=5.06e-05
c  xk(6)=7.40e-05
c  xk(7)=9.40e-05
    xk(1)=1.56e-04
10  continue

c  define initial concentrations
    do 20 i=1,nx0
do 30 j=1,ny0
c(i,j)=0.
cold(i,j)=0.
30continue
20continue

c  calculate time-dependent state concentration
    do 100 nexp=1,nexp0
do 110 k=1,niter0
if(k/1000*1000.eq.k)write (*,*)nexp,k
do 120 i=2,nx0-1
do 130 j=1,ny0-1

```

```

if (j.eq.1)then
  if (i.eq.2)then
c(i,j)=cold(i,j)
  & +deltaT*qtube/Vol*(cold(i-1,j)-cold(i,j))
& +deltaT*atube/Vol*(dx(nexp)/xl*(-cold(i,j)+cold(i+1,j))
& +dy(nexp)/xl*(-cold(i,j)+cold(i,j+1))
  & +xk(nexp)*(Csol-cold(i,j)))
else
c(i,j)=cold(i,j)
  & +deltaT*qtube/Vol*(cold(i-1,j)-cold(i,j))
& +deltaT*atube/Vol*
  & (dx(nexp)/xl*(cold(i-1,j)-2.*cold(i,j)+cold(i+1,j))
& +dy(nexp)/xl*(-cold(i,j)+cold(i,j+1))
  & +xk(nexp)*(Csol-cold(i,j)))
  endif
endif

if (j.ne.1)then
  if(i.eq.2)then
c(i,j)=cold(i,j)
  & +deltaT*qtube/Vol*(cold(i-1,j)-cold(i,j))
& +deltaT*atube/Vol*(dx(nexp)/xl*(-cold(i,j)+cold(i+1,j))
& +dy(nexp)/xl*(cold(i,j-1)-2.*cold(i,j)+cold(i,j+1)))
else
c(i,j)=cold(i,j)
  & +deltaT*qtube/Vol*(cold(i-1,j)-cold(i,j))
& +deltaT*atube/Vol*
  & (dx(nexp)/xl*(cold(i-1,j)-2.*cold(i,j)+cold(i+1,j))
& +dy(nexp)/xl*(cold(i,j-1)-2.*cold(i,j)+cold(i,j+1)))
  endif
endif

if(j.eq.1.and.k/10000*10000.eq.k)write(4,2)k,i,j,c(i,j),cold(i,j)
if(i.eq.101.and.k/10000*10000.eq.k)
  & write(5,2)k,i,j,c(i,j),cold(i,j)

```

```

2  format(3i7,2f12.6)

130 continue
120 continue

c  find the maximum absolute difference between the previous iteration and the current iteration
(cold and c)
cdiffmax=0.
cdo 140 i=2,nx0
cdo 150 j=1,ny0
c  diff(i,j)=abs(c(i,j)-cold(i,j))
cif(diffmax.lt.diff(i,j))diffmax=diff(i,j)
c150 continue
c140 continue
cwrite(*,*)nexp,diffmax
c  compare the maximum difference to the tolerance
c  if (diffmax.le.tol)then
ckmax(nexp)=k
cgoto 199
cendif

c  update cold matrix
do 160 i=1,nx0
do 170 j=1,ny0
  cold(i,j)=c(i,j)
c  define boundary conditions
if(i.eq.nx0)cold(i,j)=c(i-1,j)
if(j.eq.ny0)cold(i,j)=c(i,j-1)
170 continue
160 continue

c  calculate average concentration at outlet
199 caver(nexp,k)=0
do 200 j=1,ny0
  caver(nexp,k)=caver(nexp,k)+cold(101,j)/float(ny0)

```

```
200 continue
```

```
110 continue
```

```
100 continue
```

```
c write output results
```

```
do 250 nexp=1,nexp0
```

```
do 260 k=1,niter0,100
```

```
write(3,1)nexp,k,caver(nexp,k)
```

```
1 format(2i7,f12.6)
```

```
260continue
```

```
250continue
```

```
do 300 j=1,ny0-1
```

```
do 301 i=2,nx0-1
```

```
write(6,3)float(i),float(j),c(i,j)/Csol
```

```
301 continue
```

```
300 continue
```

```
c do 310 j=1,ny0
```

```
cwrite(6,3)(cold(i,j),i=1,nx0)
```

```
3format (100f12.6)
```

```
c310 continue
```

```
stop
```

```
end
```

## APPENDIX B: PORE NETWORK FORTRAN CODE FOR FLOW CELL FILLED WITH SAND

```

c 2D mass transport model to determine the mass transfer coefficient
c May 2017
c length of tank is 100 mm, height is 40 -10 =30 mm
c C matrix is the concentration at the current time step
cunits are in: g, m, s
implicit double precision (a-h,o-z)
parameter (nx0=502, ny0=150,nexp0=1,niter0=300000,tol=1.e-08)
dimension vel(nexp0),q(nexp0),Dx(nexp0),Dy(nexp0),xk(nexp0)
dimension caver(nexp0,niter0)
dimension c(nx0,ny0),cold(nx0,ny0)
    open(3,file='conc.out',status='unknown')
    open(4,file='tempH.out',status='unknown')
    open(5,file='tempV.out',status='unknown')
    open(6,file='sandQ1.dat',status='unknown')
c define input data
    deltaT=0.1
    grain=0.0002
    vol=(grain*0.7)**3
    atube=(grain*0.5)**2
    xl=grain*0.3
    area= 0.04*0.03
    por= 0.36
    dm=1.e-9
    cset alpha to 0.002 m from tracer tests
    alphaL=0.002
    alphaT=0.002
    Csol=156.
c define flow rate as ml/min
    q(1)=0.165
c q(2)=0.210
c q(3)=0.299
c q(4)=0.510

```

```

cq(5)=1.050
c q(6)=2.0
c q(7)=3.910
c q(8)=7.745
c q(9)=12.9
cq(10)=24.0
c q(11)= 28.0
do 10 nexp=1,nexp0
c convert flow rate to units of m^3/s
q(nexp)=q(nexp)*1.e-06/60.
qtube=q(nexp)/float(200*150)
    vel(nexp)=q(nexp)/area/por
    Dx(nexp)=alphaL*vel(nexp)+dm
    Dy(nexp)=alphaT*vel(nexp)+dm
xk(1)=3.68e-06
c xk(2)=3.92e-06
c xk(3)=5.30e-06
cxk(4)=1.41e-05
c xk(5)=1.35e-05
c xk(6)=3.23e-05
cxk(7)=4.65e-05
c xk(8)=6.96e-05
c xk(9)=1.06e-04
c xk(10)=1.41e-04
c xk(11)=1.55e-04
10 continue

c calculate time-dependent state concentration
do 100 nexp=1,nexp0

c define initial concentrations
do 20 i=1,nx0
do 30 j=1,ny0
c(i,j)=0.

```

```

cold(i,j)=0.
30continue
20continue

do 110 k=1,niter0
if(k/1000*1000.eq.k)write (*,*)nexp,k,caver(nexp,k-1)
do 120 i=2,nx0-1
do 130 j=1,ny0-1
  if (j.eq.1)then
    if (i.eq.2)then
c(i,j)=cold(i,j)
      & +deltaT*qtube/Vol*(cold(i-1,j)-cold(i,j))
& +deltaT*atube/Vol*(dx(nexp)/xl*(-cold(i,j)+cold(i+1,j))
& +dy(nexp)/xl*(-cold(i,j)+cold(i,j+1))
      & +xk(nexp)*(Csol-cold(i,j)))
    else
c(i,j)=cold(i,j)
      & +deltaT*qtube/Vol*(cold(i-1,j)-cold(i,j))
& +deltaT*atube/Vol*
      & (dx(nexp)/xl*(cold(i-1,j)-2.*cold(i,j)+cold(i+1,j))
& +dy(nexp)/xl*(-cold(i,j)+cold(i,j+1))
      & +xk(nexp)*(Csol-cold(i,j)))
    endif
  endif
endif

if (j.ne.1)then
  if(i.eq.2)then
c(i,j)=cold(i,j)
      & +deltaT*qtube/Vol*(cold(i-1,j)-cold(i,j))
& +deltaT*atube/Vol*(dx(nexp)/xl*(-cold(i,j)+cold(i+1,j))
& +dy(nexp)/xl*(cold(i,j-1)-2.*cold(i,j)+cold(i,j+1)))
  else
c(i,j)=cold(i,j)
      & +deltaT*qtube/Vol*(cold(i-1,j)-cold(i,j))
& +deltaT*atube/Vol*

```

```

    & (dx(nexp)/xl*(cold(i-1,j)-2.*cold(i,j)+cold(i+1,j))
& +dy(nexp)/xl*(cold(i,j-1)-2.*cold(i,j)+cold(i,j+1)))
endif
endif

if(j.eq.1.and.k/10000*10000.eq.k)write(4,2)k,i,j,c(i,j),cold(i,j)
if(i.eq.101.and.k/10000*10000.eq.k)
    & write(5,2)k,i,j,c(i,j),cold(i,j)
2 format(3i7,2f12.6)

130 continue
120 continue

c find the maximum absolute difference between the previous iteration and the current iteration
(cold and c)
cdiffmax=0.
cdo 140 i=2,nx0
cdo 150 j=1,ny0
c diff(i,j)=abs(c(i,j)-cold(i,j))
cif(diffmax.lt.diff(i,j))diffmax=diff(i,j)
c150 continue
c140 continue
cwrite(*,*)nexp,diffmax
c compare the maximum difference to the tolerance
c if (diffmax.le.tol)then
ckmax(nexp)=k
cgoto 199
cendif
c update cold matrix
do 160 i=1,nx0
do 170 j=1,ny0
cold(i,j)=c(i,j)
c define boundary conditions
if(i.eq.nx0)cold(i,j)=c(i-1,j)
if(j.eq.ny0)cold(i,j)=c(i,j-1)

```

```
170 continue
160 continue

c calculate average concentration at outlet
199 caver(nexp,k)=0
do 200 j=1,ny0
    caver(nexp,k)=caver(nexp,k)+cold(501,j)/float(ny0)
200 continue
110 continue
100 continue

c write output results
do 250 nexp=1,nexp0
do 260 k=1,niter0,100
write(3,1)nexp,k,caver(nexp,k)
1 format(2i7,f12.6)
260continue
250continue

do 300 j=1,ny0-1
do 301 i=2,nx0-1
write(6,3)float(i),float(j),c(i,j)/Csol
301 continue
300 continue

c do 310 j=1,ny0
cwrite(6,3)(cold(i,j),i=1,nx0)
3format (100f12.6)
c310 continue

stop
end
```